SEARCH FOR NOVEL REGULATORS OF BRAIN CIRCULATION AND THEIR FUNCTIONAL ANALYSIS

SHEN HONGYUAN

NATIONAL UNIVERSITY OF SINGAPORE

2013

SEARCH FOR NOVEL REGULATORS OF BRAIN CIRCULATION AND THEIR FUNCTIONAL ANALYSIS

SHEN HONGYUAN

B.Sc. (Honours), NUS

A THESIS SUBMITTED

FOR THE DEGREE OF DOCTOR OF PHILOSOPHY

DEPARTMENT OF BIOLOGICAL SCIENCES

NATIONAL UNIVERSITY OF SINGAPORE

2013

DECLARATION

I hereby declare that the thesis is my original work and it has been written by me in its entirety. I have duly acknowledged all the sources of information which have been used in the thesis.

This thesis has also not been submitted for any degree in any university previously.

Shen Hongyuan

15 Nov 2013

Acknowledgement

I would like to thank my supervisor, Associate Professor Vladimir Korzh, for his guidance, discussions and encouragement throughout my Ph.D. studies. He goes to extra miles in nurturing young scientists in all aspects of science research, which greatly motivates me. I would also like to thank all members of Vladimir Korzh lab for their kind suggestions, helpful discussions and encouragement when sometimes experiments become miserable. Lastly, I would like to acknowledge Institute of Molecular and Cell Biology (IMCB), Agency for Science, Technology and Research (A*STAR) for awarding me the Ph.D. scholarship, without which this work will not be possible.

TABLE OF CONTENTS

Summary

Brain circulation has attracted renewed interest as an active signalling milieu that regulates brain development, homeostasis, and disease. The vertebrate brain ventricular system is a series of connected cavities which are filled with cerebrospinal fluid (CSF) and surrounded by neuroepithelium. CSF serves as a fluid envelop that protects the central nervous system. Due to its immediate contact with neural stem cells in the developing and adult brain, it also plays an essential role in regulating neuronal functioning. While the gross anatomy of ventricular system and CSF hydrodynamics are well documented, the molecular mechanisms underlying their development are poorly understood. Identification of novel molecular regulators of brain circulation will help to uncover more details of this important process. In this study, a zebrafish forward genetic screen was carried out using *Tol2* transposon-mediated gene-breaking insertional mutagenesis strategy. Among all the mutants generated, a *kcng4b* mutant, which lacks voltage-gated potassium channel Kv6.4b silent subunit function, displayed developmental defects in embryonic brain ventricles, including neuroepithelial cells delamination, ventricle dilation and thus hydrocephalus. Functional analyses of the mutant provide the first *in vivo* evidence that the silent Kv6.4b subunits, play an essential role in regulating embryonic brain lumen inflation by modulating neuroepithelial cell proliferation and maintaining neuroepithelium integrity, presumably through the formation of Kv2.1/Kv6.4b heterotetramers at the embryonic brain ventricular zone. These results provide a functional basis for the modulation of

Kv2.1 by silent Kv6.4b subunits during vertebrate embryonic brain ventricle morphogenesis.

List of Tables

Appendix

List of Figures

List of Symbols

aa	amino acid
AP	alkaline phosphatase
AV	arachnoid villi
BBB	blood–brain barrier
CMZ	cilliary marginal zone
CP	choroid plexuses
CSF	cerebrospinal fluid
DA	dorsal aorta
dpf	days post fertilization
DLAV	dorsal longitudinal anastomotic vessels
DPPX	dipeptidyl-peptidase-like protein
eCSF	embryonic cerebrospinal fluid
ECM	extracellular matrix
eNPC	embryonic neural progenitor cells
ENU	N-ethyl-N-nitrosourea
ER	endoplsmic reticulum
FGFs	fibro-blast growth factors
FP	floor plate
GBT	'gene-breaking' transposon
GFP	green fluorescent protein
hpf	hours post fertilization
IGFs	insulin-like growth factors
I2E3	intron 2 exon 3
$\mathbf{I_{DR}}$	delayed-rectifier current
INM	interkinetic nuclear migration
ISF	interstitial fluid
ISV	intersegmental vessels
Kv	voltage-gated potassium channel
Kv2.1	protein encoded by *kcnb1*
Kv6.4	protein encoded by *kcng4*
Kv6.4a	protein encoded by *kcng4a*
Kv6.4b	protein encoded by *kcng4b*
KvS	'silent' voltage-gated potassium channel
MCS	mesenchymal stem cells
MHBC	midbrain-hindbrain boundary constrictions
MO	morpholino
Nav	voltage-gated sodium channel
NSC	neural stem cells
PCV	peripheral cardinal vein
PFA	paraformaldehyde
PH3	phosphohistone H3
RB	Rohon-Beard
RBC	red blood cells
RFP	red fluorescent protein
RNAi	RNA interference
SA	splice acceptor
SCO	subcommissural organ

SD	splice donor
Shh	sonic hedgehog
SVZ	subventricular zone
TG	trigeminal ganglion
VSD	voltage-sensing domain
VZ	ventricular zone
ZFN	zinc finger nuclease

Chapter 1. Introduction

1.1 The brain ventricular system

The vertebrate brain has a complex three-dimensional structure. One highly conserved aspect of brain structure is the ventricular system, a series of connected cavities lying deep within the brain, filled with cerebrospinal fluid (CSF). The brain ventricles and the CSF they contain, together with the surrounding neuroepithelium and associated structures, form the brain ventricular system (Lowery and Sive, 2009). In the adult human brain, there are four connected ventricles: two lateral ventricles within the cerebrum, a third ventricle within the diencephalon, and a fourth ventricle lying between the cerebellum and pons (Figure 1.1). The lateral ventricles are connected to the third ventricle, which is linked to the fourth ventricle via the cerebral aqueduct. In turn, the fourth ventricle joins to the spinal cord canal and the subarachnoid space that envelops the brain. The adult human brain contains about 140 ml of CSF, of which approximately 20 ml is within the ventricles and the remainder is surrounding the brain (Brown et al., 2004).

1.2 The choroid plexues and CSF production

It is generally believed that adult CSF is produced mainly by the choroid plexuses, highly vascular structures located within the ventricles (Figure 1.1), although some CSF may be produced by ependyma, cells lining the ventricles. CSF secretion in adults varies between 400 ml to 600 ml per day. The choroid plexuses consist of granular meningeal protrusions into the ventricular lumen, the epithelial surface of which is continuous with the ependyma. They comprise a tuft of capillaries. Choroidal cells present microvilli at their apical pole and are interconnected by tight junctions with a variable distribution

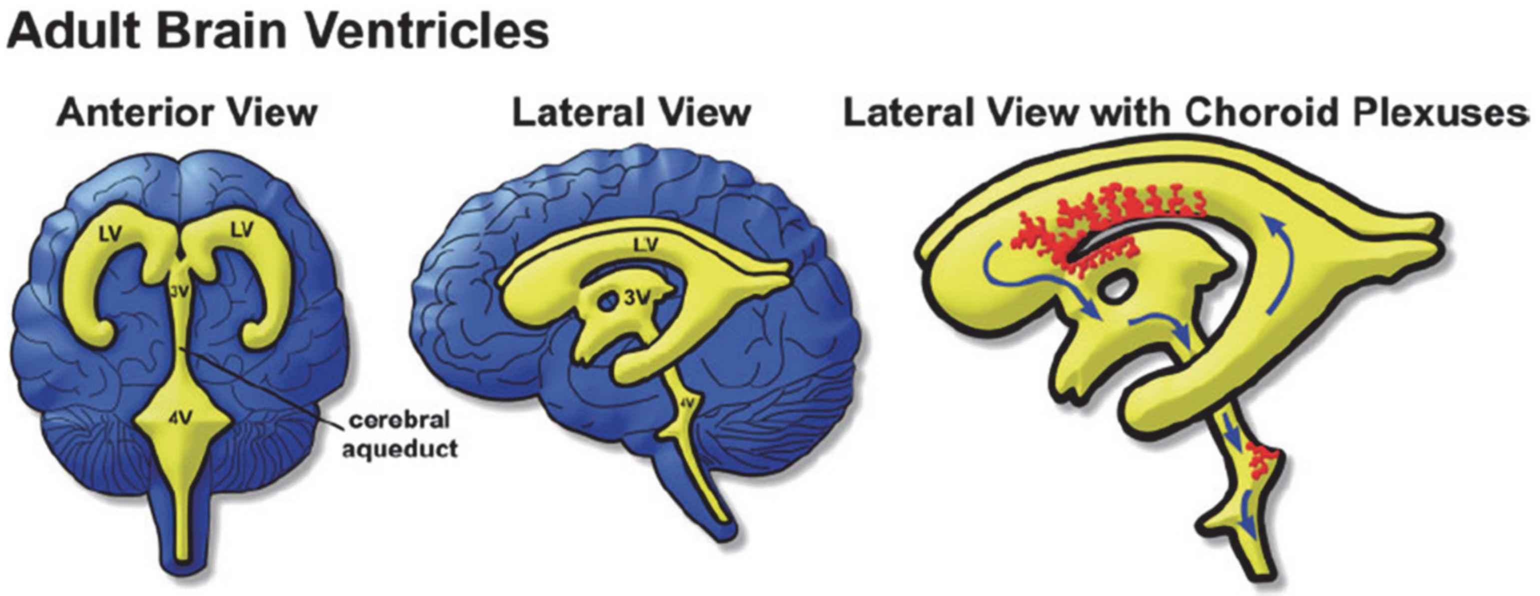

Figure 1.1. The adult brain ventricular system. Cartoon representation of adult human brain ventricles. Blue represents brain tissue and yellow shows brain ventricles. Choroid plexuses are in red, blue arrows designate direction of CSF flow. LV, lateral ventricle, 3V, third ventricle, 4V, fourth ventricle (Lowery and Sive, 2009).

according to the site on the ventricular wall (Brodbelt and Stoodley, 2007; Sakka et al., 2011).

1.3 The brain circulation and CSF hydrodynamics

1.3.1 The classical hypothesis based on choroid plexuses

The brain circulation or CSF circulation is a dynamic phenomenon (Figure 1.2). Classical model of brain circulation suggests that CSF circulates according to a unidirectional and rostrocaudal flow inside the ventricular cavities and a multidirectional flow in subarachnoid spaces with the exchange of various substances between the CSF and interstitial compartments. CSF produced by the choroid plexuses in the lateral ventricles travels through interventricular foramina to the third ventricle, and then the fourth ventricle via the cerebral aqueduct and finally to the subarachnoid spaces via the median aperture (foramen of Magendie) of the fourth ventricle (Redzic et al., 2005; Sakka et al., 2011). CSF flow is generated by the systolic pulse wave and rapid respiratory waves. Subcommissural organ (SCO) synthesizes SCO-spondin, which aggregates to form Reissner fibre that guide the CSF circulation through the cerebral aqueduct. In human the SCO disappears during postnatal development. Abnormality of the SCO could explain certain forms of congenital hydrocephalus.

CSF is reabsorbed and drained into arachnoid villi (AV), finger-like endothelium-lined protrusions of the arachnoid outer layer through the dura mater in the lumen of venous sinuses (Figure 1.3). In humans, arachnoid villi in lumbosacral nerve roots increase CSF absorption in response to gravity

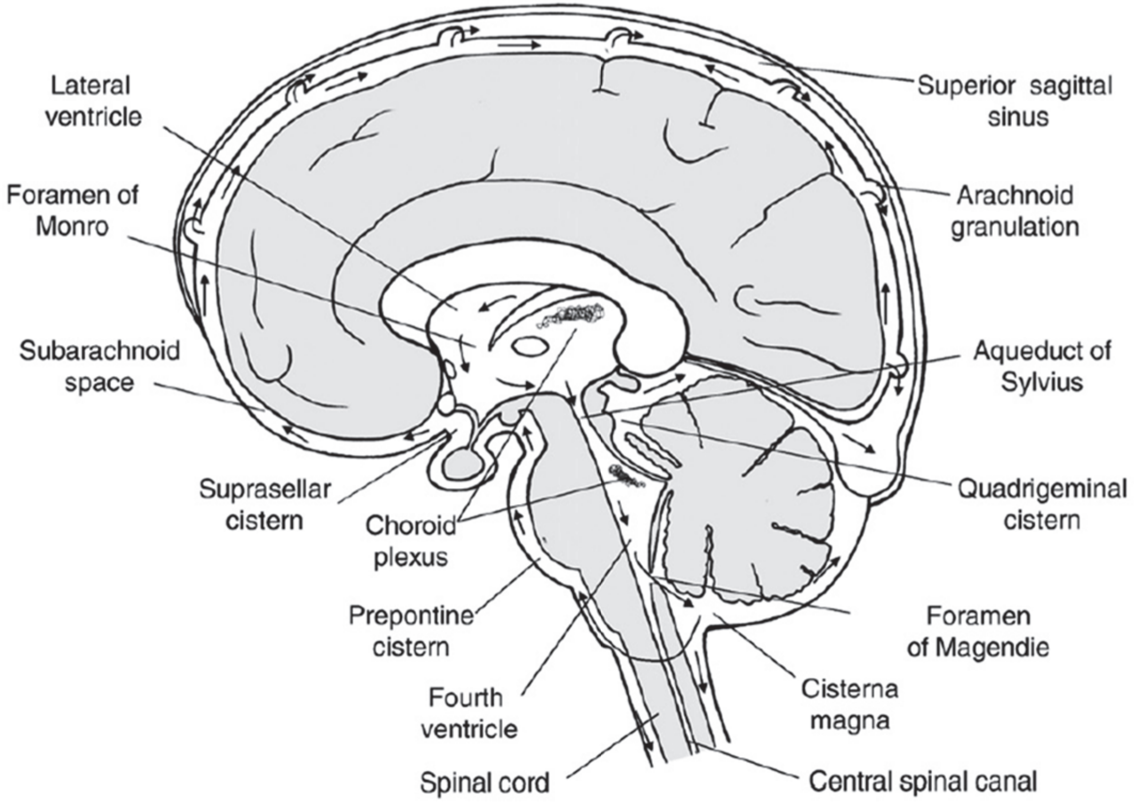

Figure 1.2. The classic model of CSF circulation in the human central nervous system. CSF is shown as the grey area and the arrows point the direction of CSF circulation and the sites of CSF absorption (Oreskovic and Klarica, 2010).

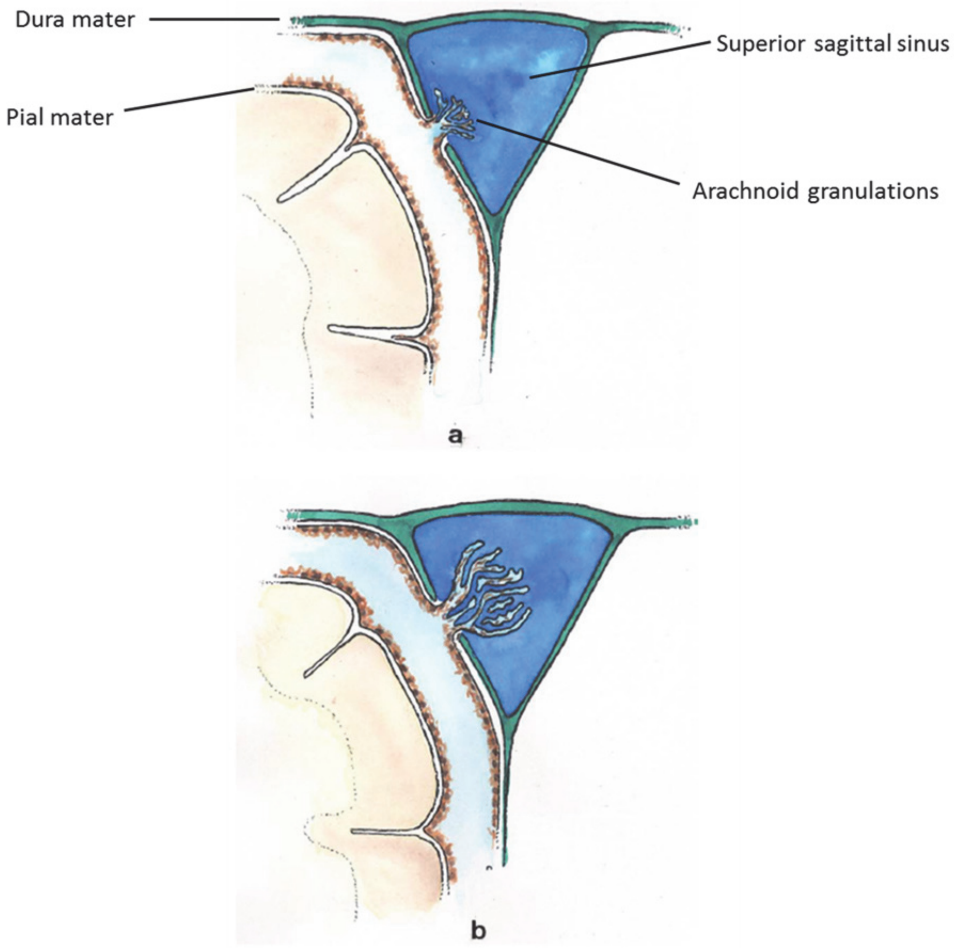

Figure 1.3. CSF absorption in relation to cranial arachnoid granulations. Arachnoid granulations are endothelium-lined finger-like meningeal protrusions into the cranial venous sinuses through the dura mater (a). They have a valve-like function. When cerebrospinal fluid pressure increases, arachnoid villi develop, thereby increasing their surface of exchange and cerebrospinal fluid absorption (Sakka et al., 2011) (Modified).

when body is in the upright position, and the absorbed CSF then enters the lymphatic system (Brodbelt and Stoodley, 2007; Sakka et al., 2011).

1.3.2 The new hypothesis based on CNS blood capillaries

Until now, the traditional model of CSF circulation has been accepted worldwide for nearly a hundred years, and is widely used in textbooks and is constantly referenced or cited as a matter of fact in most of the prestigious journals. However, this classical model has been challenged recently by experimental evidence gathered due to a renewed interest in CSF and brain development.

The new experiments all point to a new working hypothesis. CSF is constantly produced and absorbed in the whole CSF system as a consequence of filtration and reabsorption of water volume through the capillary walls into the surrounding brain tissue. CP are not the main source of CSF production. The CSF exchange between the entire CSF system and the surrounding tissue depends on physiological conditions that predominate within those compartments (Oreskovic and Klarica, 2010).

Formulation of the new hypothesis is mainly due to the fact that there is increasing amount of new experimental evidence challenging the classical hypothesis. First, removal of the CP from both lateral ventricles in human or monkeys results in no significant changes in the volume of CSF secretion nor in CSF composition. Even after a total choroid plexectomy the CSF is secreted at the rate of approximately 1 L per day. For many years treatment of hydrocephalus by choroid plexectomy remained the most popular form of surgical procedure for infantile hydrocephalus in the United States. However, over decades it became clear that bilateral extirpation and/or cauterization of the CP invariably failed to benefit the patients. Because of universally poor results, choroid plexectomy was abandoned by neurosurgeons as a treatment for hydrocephalus, and today it is an operation of historic interest only and has no place in the treatment of hydrocephalus (Oreskovic and Klarica, 2010). Second, when the aqueduct of Sylvius is subjected to complete blockage, neither increase of CSF pressure nor ventricle dilation is observed in cats (Klarica et al., 2009). Third, under normal CSF pressure, ^{3}H-water is rapidly reabsorbed into periventricular capillaries and is not delivered to subarachnoid spaces, suggesting that CSF bulk water is absorbed into brain ventricles itself (Bulat et al., 2008). Taken together, these experiments cannot be explained by and are clearly contradictory to the classical hypothesis according to which CSF is primarily produced in the CP, and then flows from the ventricles to the subarachnoid spaces, and is mainly reabsorbed into AV.

Thus, the new hypothesis is that CSF is produced and reabsorbed throughout the entire CSF-interstitial fluid (ISF) functional unit. ISF, the fluid in the cerebral parenchyma and CSF, the fluid in subarachnoid spaces, constitute a functional unit. The volumes are regulated through an osmotic gradient and hydrostatic pressure formed by the capillaries at one side and CSF-IF unit at the other side. Cerebral capillaries form the blood–brain barrier (BBB) and are characterized by endothelial cells with tight intercellular junctions. In fact, the endothelium of CNS capillaries contains Na-H antiporters (for transfer of substances across cellular membrane) and high NaKATPase activity (Figure 1.4). On the other hand, a diverse varieties of ion channels

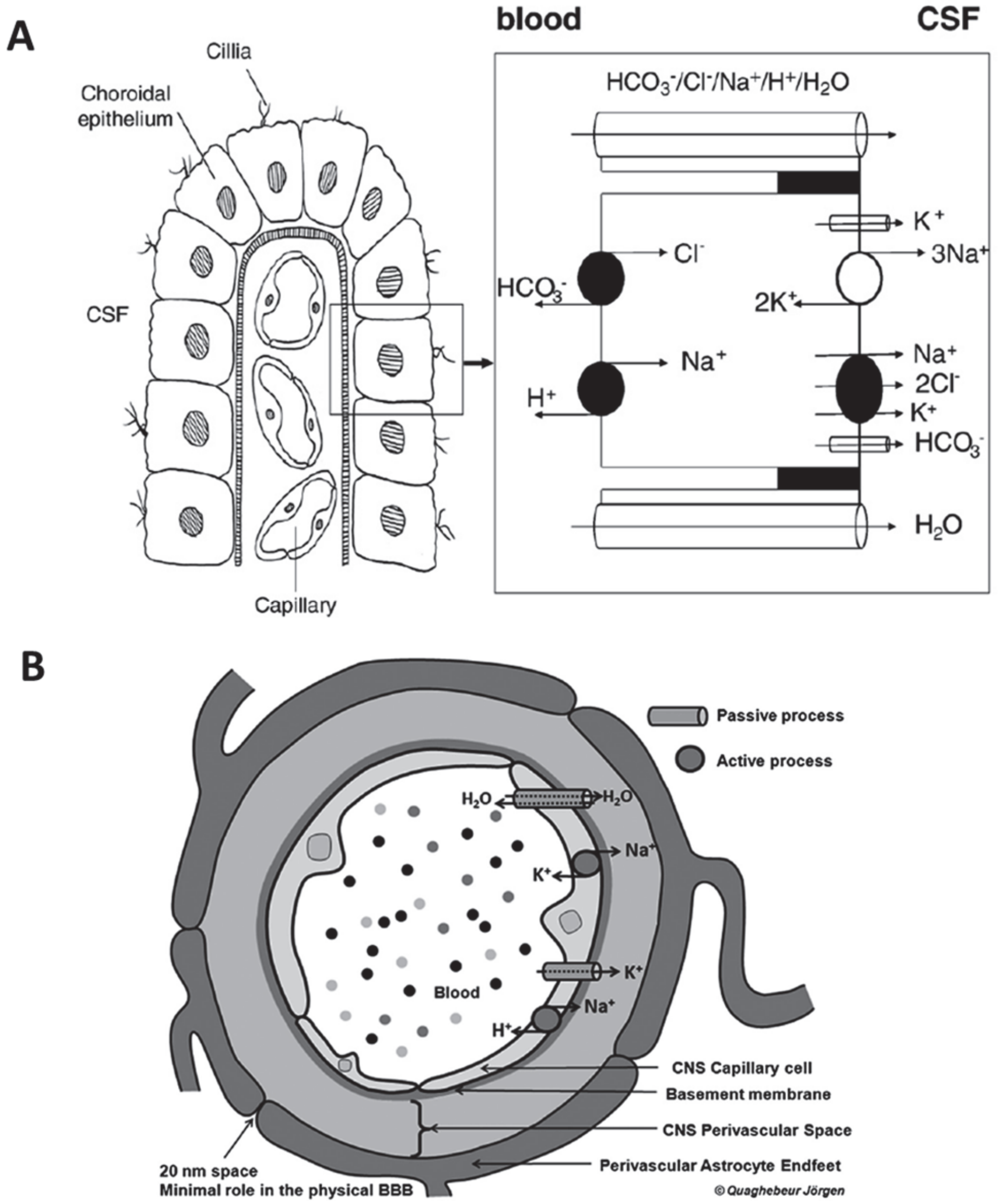

Figure 1.4. New hypothesis of CSF hydrodynamics based on capillary endothelium. (A). Schematic representation of CSF secretion. Inset shows the proposed Na+–K+ pump placed on the apical (CSF-facing) membrane. Aquaporin channels exist on the apical and basolateral membrane (Oreskovic and Klarica, 2010). **(B)** Cross section of a CNS capillary and its perivascular astrocytic endfeet (Chikly and Quaghebeur, 2013).

residing on the apical and basal-lateral membrane of ependyma cells lining the brain ventricles are being characterized (Brown et al., 2004). In addition, intravascularly injected FITC-conjugated FGF2 passes into the embryonic CSF in chick (Martin et al., 2006), suggesting a rapid fluid exchange between blood circulation and CSF. These results seem to support CSF production by capillary endothelium.

1.4 The embryonic ventricular system

Although it seems that emerging experimental evidences are more in favor of CSF production by capillary endothelium, transforming a classical model that has been established for a hundred years into a new model requires more conclusive studies. In humans, brain ventricles inflate several weeks prior to CP formation. In zebrafish, the ventricles begin inflating at 19 hpf (Lowery and Sive, 2005) but the CP is not formed until approximately 48 hpf (Bill et al., 2008; Garcia-Lecea et al., 2008). Similarly, all venous sinuses do not exist in rats until 20 days after birth. The arachnoid villi (AV) do not appear to exist before birth in humans (Sakka et al., 2011). They start developing at the time of birth and increase in number with age. Therefore, it is imperative that a mechanism exists to produce embryonic CSF (eCSF) for brain ventricle inflation and reabsorb eCSF for clearance. Whether the mechanisms regulating CSF hydrodynamics are conserved between embryos and adults remains to be elucidated. However, understanding eCSF hydrodynamics would definitely shed light on the understanding of the complexity of CSF circulation in adult brain.

The vertebrate embryonic brain originates from a columnar epithelium that comprises the neural plate. In humans, the neural plate develops early in the fourth week after fertilization, and later that week, completes the neurulation to form the neural tube (Figure 1.5, B). In zebrafish, this process happens during early somitogenesis. The neural plate converges and forms the neural keel, eventually fusing at the dorsal midline to form the neural rod (Figure 1.5, C). The fundamental mechanisms of neurulation appear to be largely conserved among vertebrates. Subsequently, the anterior portion of the tube becomes the brain and the posterior becomes the spinal cord. Towards the end of neurulation, a series of stereotypical constrictions, bends, and expansions occur to subdivide into the primary lumenized embryonic ‘brain vesicles’, forming the future forebrain, midbrain and hindbrain (Figure 1.5, A).

After lumen formation, the cavities of brain vesicles are filled with eCSF. Following early brain ventricle shaping and initial inflation, the ventricles undergo massive expansion. In zebrafish, this process happens between 17-24 hpf, a critical ‘window period’ for the initial brain ventricle inflation, neuroepithelial morphogenesis and ventricle expansion (Lowery et al., 2009). In mammals and chicks, spinal cord occlusion transiently seals off the brain ventricular space directly preceding this expansion period, which may then allow intraluminal pressure to promote ventricle enlargement (Desmond and Schoenwolf, 1985). It is not known whether this process also occurs in bony fish.

In terms of individual ventricle, live imaging studies suggest that the hindbrain ventricle of zebrafish does not open in an anterior-to-posterior sequence

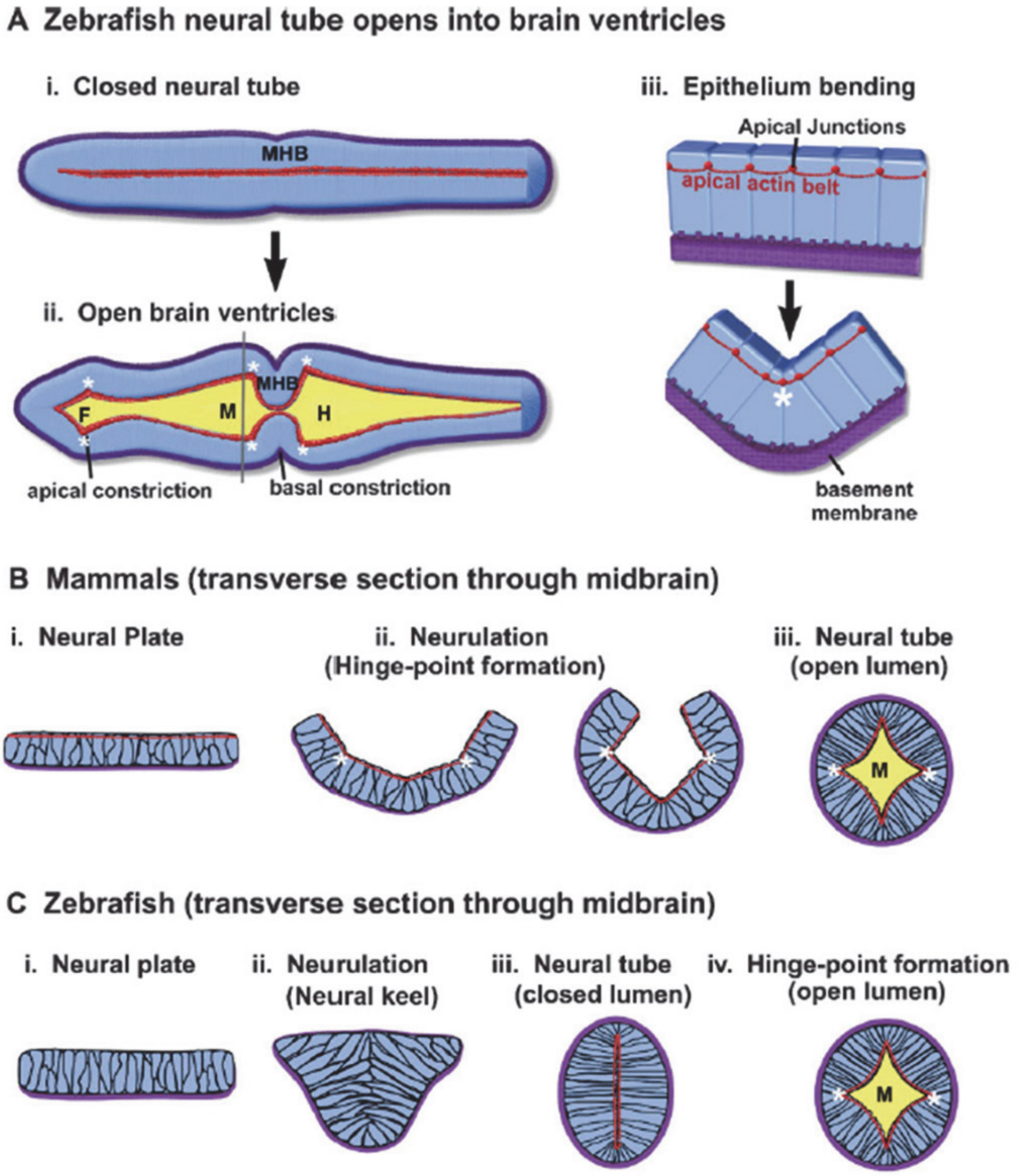
A Zebrafish neural tube opens into brain ventricles
i. Closed neural tube
MHB
ii. Open brain ventricles
MHB
F
M
H
apical constriction
basal constriction
iii. Epithelium bending
Apical Junctions
apical actin belt
basement membrane
B Mammals (transverse section through midbrain)
i. Neural Plate
ii. Neurulation (Hinge-point formation)
iii. Neural tube (open lumen)
M
C Zebrafish (transverse section through midbrain)
i. Neural plate
ii. Neurulation (Neural keel)
iii. Neural tube (closed lumen)
iv. Hinge-point formation (open lumen)
M

Figure 1.5. Neuroepithelial morphogenesis during brain ventricle development. (A). Schematic showing zebrafish neuroepithelium as it opens into the brain ventricles. After neurulation, the zebrafish neuroepithelium is a closed neural tube (i) connected by apical actin junctions and surrounded by a basement membrane (i,iii). As the brain ventricles open, the neuroepithelium bends in locations of apical constriction (white asterisks) and basal constriction at MHB (ii,iii). **(B).** Schematic depicting stages of neurulation in mammals, beginning with the columnar epithelium of the neural plate (i). Neurulation and hinge-point formation occur concurrently (ii), resulting in an open neural tube with hinge-points already formed. The lumen remains open and expands after neurulation is complete (iii). **(C).** Schematic depicting stages of neurulation in zebrafish, beginning with the columnar neural plate (i). Neurulation progresses through a ‘‘neural keel’’ stage (ii) and ends with a closed neural tube (iii). Subsequently, the neural tube opens and forms hinge-points to shape the ventricles (iv) (Lowery and Sive, 2009).

(Gutzman and Sive, 2010). Rather, opening occurs in a stereotypical sequence along the hindbrain, with initial openings between rhombomeres, and later coalescence of these openings into the hindbrain ventricle lumen. This mechanism of lumen opening is also observed in the zebrafish gut (Bagnat et al., 2007), where initial opening of multiple small lumens coalesce to form a single gut lumen. Thus, the strategy utilized during the brain ventricle lumen opening could be used to generate lumen in other tissues as well.

1.5 The embryonic CSF

1.5.1 eCSF is produced by neuroepithelial cells

Unlike a theory of the adult CSF hydrodynamics that is still in debate, there is no doubt that the neuroepithelium secretes the initial embryonic CSF (eCSF) to inflate the ventricle. The neuroepithelium directs the correct positioning of ventricles and later morphogenesis that shapes the brain. Importantly, it also directs the secretion of eCSF into the ventricular lumen resulting in inflation of the brain ventricles (Figure 1.6).

Only recently, a critical role of eCSF has been established for regulating survival and proliferation of neuroepithelial cells. The eCSF is in direct contact with the neuroepithelium, a pseudostratified cell layer comprising proliferating pluripotent neural stem cells (NSC) and primary progenitor cells. Neuroepithelial cells are radially elongated and contact both the apical (ventricular) and basal (pial) surfaces. They divide at the ventricular surface, forming a ventricular zone (VZ), but pull their nucleus towards the pial surface during interphase, a process called interkinetic nuclear migration (INM) (Merkle and Alvarez-Buylla, 2006). Symmetrical division of NSC at the VZ

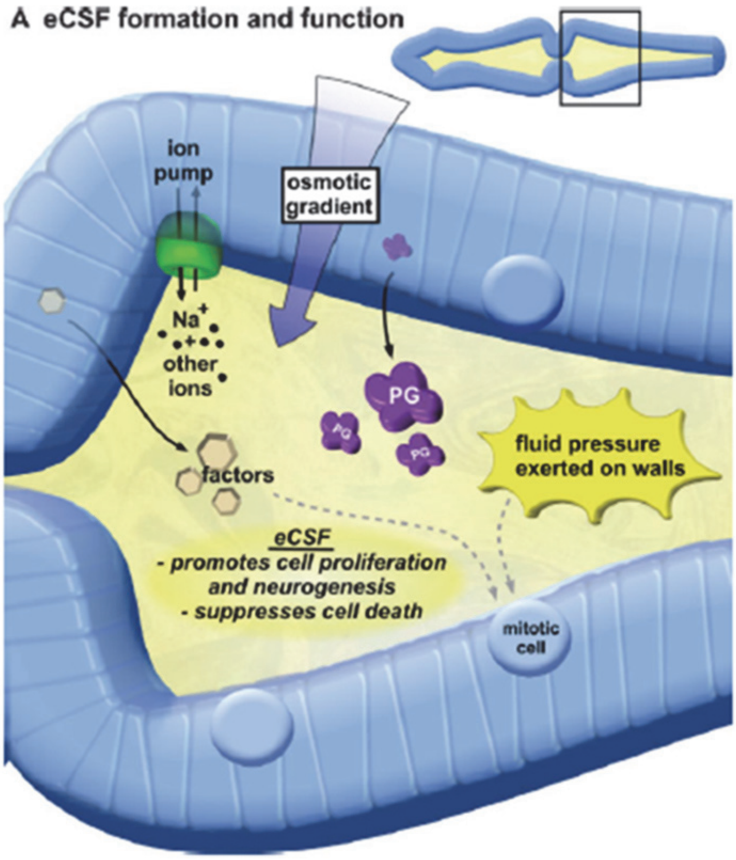

Figure 1.6. eCSF formation and function during brain ventricle inflation. Cartoon depicting eCSF secretion and function. Inset: dorsal view of embryonic brain, after initial lumen inflation, with enlarged area (hindbrain) boxed. Ion pumps and proteoglycan secretion are thought to form an osmotic gradient regulating fluid flow. Signaling and growth factors are also secreted. Both fluid pressure and growth factors stimulate cell proliferation and gene expression within the surrounding neuroepithelium. Not drawn to scale. PG: proteoglycans. Circular cells at ventricular surface are mitotic cells (Lowery and Sive, 2009).

establishes the pool of stem cells during the initial phases. Later, NSC divide either asymmetrically, generating a stem cell that remains in the VZ and a daughter cell that migrates radially outward or much more seldom symmetrically to form two NSC. The accumulation of daughter cells thickens the developing brain and radially stretches the neuroepithelial cells. This process has been well studied in mammals (Farkas and Huttner, 2008) and shown to be conserved in zebrafish (Alexandre et al., 2010; Leung et al., 2011).

It has been demonstrated in zebrafish that formation of eCSF requires the NaKATPase ion pump activity. Zebrafish *snakehead* mutant that lacks NaKATPase activity fails to inflate the brain ventricle, probably due to lack of osmotic gradient formed by this pump to generate fluid movement into the lumen (Chang et al., 2012; Lowery and Sive, 2005). Earlier studies in chick indicated that fluid movement into the brain ventricles could be also regulated by proteoglycans secreted by the neuroepithelium (Gato et al., 1993).

1.5.2 Roles of eCSF in brain ventricle development

eCSF is necessary for normal neuronal development, as drainage of eCSF results in reduced cell proliferation and increased cell apoptosis in the developing chick brain (Desmond and Jacobson, 1977). It has been suggested that one of the possible ways that eCSF increases neuroepithelial cell proliferation is by generating intraluminal pressure on the embryonic ventricular surface (Desmond et al., 2005), although the mechanism remains elusive.

Factors contained in the eCSF are also critical for regulating neuroepithelial proliferation. It has been suggested that composition of eCSF changes during development and between ventricles. Protein composition differs substantially between adult CSF and eCSF. eCSF is found to be protein-rich. It contains approximately 200 different proteins, including signalling and growth factors, extracellular matrix (ECM) proteins, transport and carrier proteins, enzymes and proteases (Parada et al., 2005; Zappaterra et al., 2007). To name a few, fibroblast growth factors (FGFs), insulin-like growth factors (IGFs), sonic hedgehog (Shh), retinoic acid (RA), bone morphogenic proteins (BMPs), Wnts and others are all found in eCSF (Martin et al., 2006; Zappaterra and Lehtinen, 2012). These factors are shown to have a role in promoting neuroepithelial growth, as isolated chick and rat embryonic brain cells are not able to replicate or undergo neurogenesis in defined medium, unless eCSF is added back to culture (Gato et al., 2005).

In fact, it seems likely that eCSF fluid serves as a route for trafficking of ligands or signalling molecules between the apical membrane of neural progenitors cells. In the early neural tube, GFP-tagged Shh is found in small vesicles enriched, within the apical cell cortex, at the basal body (Chamberlain et al., 2008). Also, the primary cilium of neural progenitor cells appears to be a novel site for the budding of extracellular membrane vesicles carrying the somatic stem cell marker prominin-1 (CD133) into the ventricular fluid (Dubreuil et al., 2007). Electron microscopy analyses of floor plate (FP) cells of chick embryos revealed exosome-like particles attached to the apical surface of ventricles with a tendency to stick with a cilia (Bachy et al., 2008). Therefore, membrane budding and vesicle trafficking could be of critical importance for cell cycle regulations and signal transductions en route eCSF across the apical membrane of neuroepithelium.

1.6 Transposon mediated insertional mutagenesis screen

While the gross anatomical development of the ventricles is well documented, the molecular mechanisms underlying this development remain poorly understood. Moreover, the long debates over CSF hydrodynamics, classical hypothesis and the new capillary endothelium hypothesis, are striving for the identification of key regulatory molecules and their functional mechanism that could greatly advance our understanding of CSF physiology and many other aspects of normal brain activities.

1.6.1 Overview of zebrafish forward genetic screens and brain morphology mutants

Forward genetic screens are important tools for identification of novel molecular regulators and understanding key gene pathways controlling development. In zebrafish, current established forward genetic tools include radiation mutagenesis, N-ethyl-N-nitrosourea (ENU)-based chemical mutagenesis and insertional mutagenesis using virus- and transposon-based vectors. Multiple large-scale chemical mutagenesis screens using ENU have successfully produced and characterized an impressive collection of zebrafish mutants that affect various biological processes. In spite of the high efficiency in generation of point mutations, the major limitation in this approach is the identification of genes whose mutations are responsible for the particular phenotype.

An alternative approach is insertional mutagenesis, in which an exogenous DNA serves as a mutagen and also functions as a molecular tag for identifying the gene whose disruption causes the phenotype. Insertion of DNA into most locations on a vertebrate genome has little or no effect on any gene or gene product, as exons tend to encode only 1% to 2% of most vertebrate genomes. However, insertion in the exon causes mutations, by direct disruption of the coding sequences of a protein (Figure 1.7, A). Also, insertion of exotic sequences usually leads to destabilization of the transcript through nonsense mediated mRNA decay.

A large scale insertional mutagenesis screen in zebrafish using pseudotyped retrovirus (Figure 1.7, B) has been carried out and generated a library of mutations (the Hopkins Library) that have been molecularly characterized, due to its insertional nature. Nearly 30% of the insertions are found to be in exons, whereas 70% of mutagenic insertions are in introns. For reasons that are not clear, these insertions usually result in the reduction or complete abrogation of endogenous RNA expression (Amsterdam et al., 2011).

Until today, mutants isolated from these large scale screens are still being annotated, characterized and classified. Lowery et al. (2009) have performed detailed phenotypic characterization of 16 zebrafish brain mutants and classified them into four categories: (1) midline separation defects (2) reduced ventricle size (3) midbrain-hindbrain boundary abnormalities (4) absence of brain ventricle lumen inflation. Analysis of these brain morphology mutants has allowed the definition of several steps and corresponding gene functions required for brain morphogenesis. Unfortunately, only one mutant from

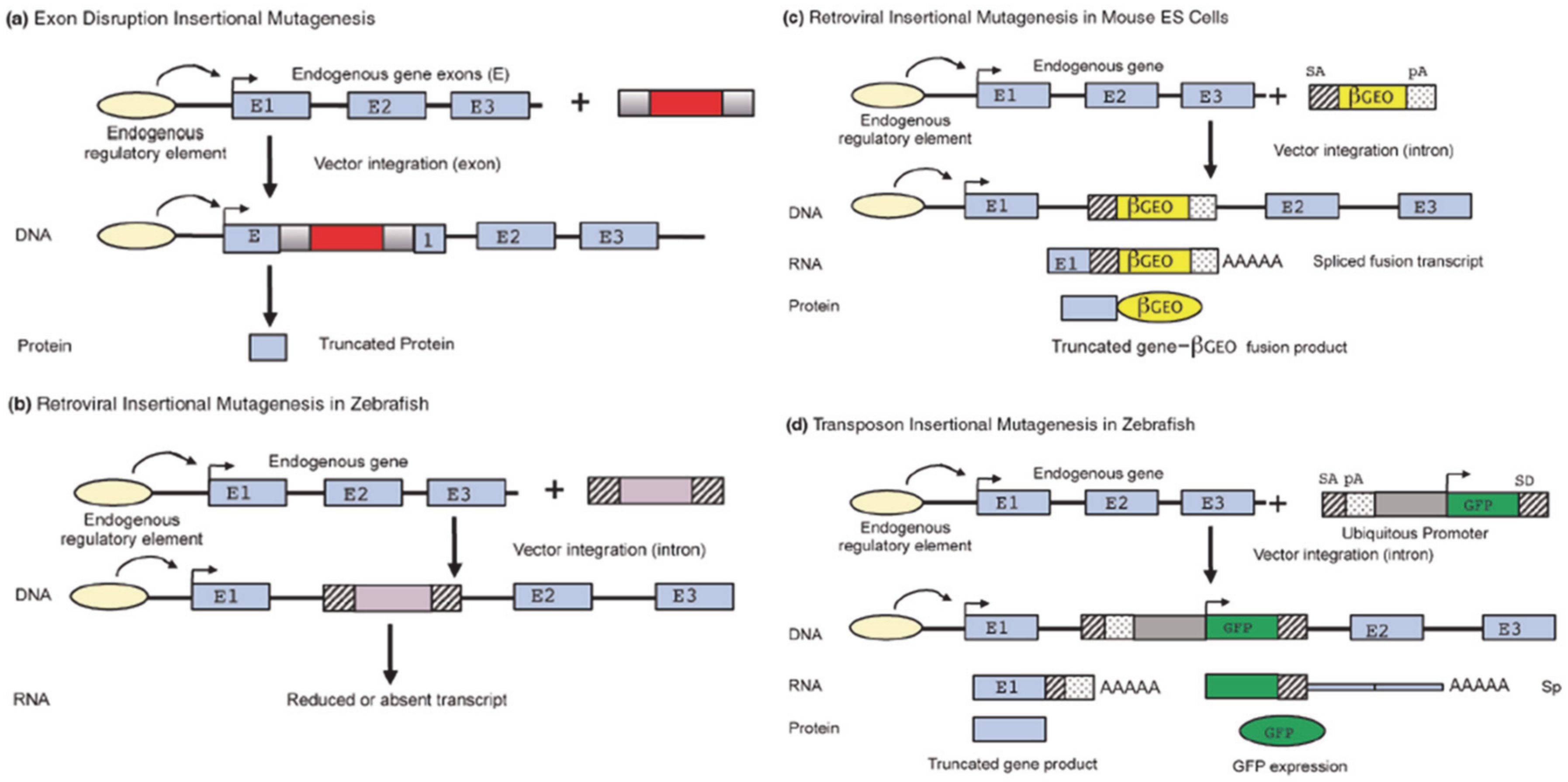
(a) Exon Disruption Insertional Mutagenesis
Endogenous gene exons (E)
E1
E2
E3
+
Endogenous regulatory element
Vector integration (exon)
DNA
E
1
E2
E3
Protein
Truncated Protein
(b) Retroviral Insertional Mutagenesis in Zebrafish
Endogenous gene
E1
E2
E3
+
Endogenous regulatory element
Vector integration (intron)
DNA
E1
E2
E3
RNA
Reduced or absent transcript
(c) Retroviral Insertional Mutagenesis in Mouse ES Cells
Endogenous gene
E1
E2
E3
+
SA
βGEO
pA
Endogenous regulatory element
Vector integration (intron)
DNA
E1
βGEO
E2
E3
RNA
E1
βGEO
AAAAA
Spliced fusion transcript
Protein
βGEO
Truncated gene−βGEO fusion product
(d) Transposon Insertional Mutagenesis in Zebrafish
Endogenous gene
E1
E2
E3
+
SA pA
GFP
SD
Endogenous regulatory element
Ubiquitous Promoter
Vector integration (intron)
DNA
E1
GFP
E2
E3
RNA
E1
AAAAA
AAAAA
Sp
Protein
GFP
Truncated gene product
GFP expression

Figure 1.7. Insertional mutagenesis strategies used in vertebrates. In each case, a schematized endogenous locus is represented by exons (E) and an endogenous regulatory element. A non-integrated vector is also shown above, with integrated vector below. Transcriptional start sites are shown as an arrow above each diagram. **(A).** Integration of DNA into a coding exon can mutate the locus, resulting in a truncated gene product. **(B).** Retroviral insertional mutagenesis alters the tagged locus using multiple methods, including the loss of the encoding transcript. **(C).** 5’ gene trapping in mouse embryonic stem cells. Shown is one approach whereby the resulting fusion transcript encodes a truncated gene product fused to the selectable marker protein. **(D).** Insertional mutagenesis in zebrafish using transposons. Based on 3’ exon or poly(A) trapping methods, this approach uses two components: a transcriptional termination cassette to truncate the integrated locus and a separate 3’ exon trap gene finding cassette. See text for details. pA, polyadenlyation signal; SA, splice acceptor; SD, splice donor (Sivasubbu et al., 2007).

categories (2) and (4) have the molecular lesion responsible for the mutant phenotype identified. The *snakehead* mutant displays an absence of brain ventricle inflation, due to a mutation in the NaKATPase activity, encoded by *atp1a1a.1* gene. The rest brain ventricle mutants are still waiting for their molecular identities to be established.

1.6.2 The transposon mediated insertional mutagenesis approach

To search for novel regulators of brain circulation, a forward genetic screen for mutants with efficient disruption of gene function that could ease the identification of the molecular nature for the mutation is desirable. Recently, transposon-mediated gene trapping methods developed for zebrafish demonstrated a great potential for efficient disruption of tagged genes (Sivasubbu et al., 2007). Traditionally gene trapping can be divided into a 5'- gene trap and 3'- gene trap. A 5'- gene trap vectors typically contain a splice acceptor immediately upstream of a reporter used for ES cell selection (such as βgeo) (Figure 1.7, C). Integration of the gene trap vector in a promoter, exon, or intron of transcriptionally active loci can generate a fusion transcript between the upstream coding sequence and the reporter. With a high efficiency splice acceptor and poly(A) signal serving as an artificial 3' terminal exon, this trap can disrupt the expression of the trapped locus by inducing truncation of the 'hijacked' transcript. Limitation of this method includes the requirement for an endogenous expression of the tagged gene. Furthermore, because the insertion can occur in any one of the three reading frames, only one-third of the loci that are in the correct reading frame will be identified by reporter (βgeo in this case), hence reducing the efficiency of identifying a trapped gene.

Recently, a combined 5’-3’ gene trap, named ‘gene-breaking’ transposon (GBT) vector, was developed to trap genes in zebrafish (Sivasubbu et al., 2007; Sivasubbu et al., 2006). This GBT vector uses the dual module, including a 5’ transcriptional terminator cassette to mutate the gene in concert with 3’ gene trapping as an alternative strategy to select for intragenic vector integrations (Figure 1.7, D). The ability of GBT vector to mutate genes upon intronic insertion is almost exclusively due to the 5’ transcriptional termination cassette, a function that is independent of the 3’ gene trapping mechanism. Furthermore, GBT-mediated trapping does not depend on the expression status or relative abundance of the endogenous transcript. Therefore, nearly all genes should be available for mutagenesis using this approach, which is a key advantage GBT-mediated gene traps. Combining the efficient insertion rate of *Tol2* transposon (Parinov et al., 2004), this *Tol2*-GBT insertional mutagenesis system offers great potential for screening of novel regulators of brain circulation in zebrafish.

In this work, the *Tol2*-GBT-mediated forward genetic screen was carried out. From 61 founder families, 130 insertion sites have been successfully mapped. Out of them, 32 insertions were found to be located in the intronic sequences with correct *cis*-orientation as tagged genes, hence potentially mutagenic. An additional four insertions were found in exons of genes. Morphological screening for brain defects in the mutant library indicated that Kv6.4b, a voltage-gated potassium channel subunit, encoded by *kcng4b* gene, is a novel regulator of embryonic brain ventricle lumen inflation, as mutant embryos with *Tol2*-GBT insertion in *kcng4b* locus displayed cell delamination from brain ventricular surface and hydrocephalus. This is the first demonstration that Kv6.4b activity is essential for eCSF volume regulation. Thus, the Kv6.4b mutant was selected for further functional characterization.

1.7 Voltage-gated potassium channels (Kv)

1.7.1 The principle subunits

Voltage-gated potassium (Kv) channels are K+ selective transmembrane proteins that allow diffusion of potassium ions across the plasma membrane along electrochemical gradient. These proteins serve a wide range of functions in both excitable and nonexcitable cells, including regulation of the resting membrane potential and control of the shape, duration, and frequency of action potentials (Bocksteins and Snyders, 2012; Pongs, 1999; Vacher et al., 2008).

A fully assembled Kv channel is a tetramer of the principle α subunits, arranged around a central aqueous pore (Figure 1.8, A). Each α subunit consists of six transmembrane segments (S1–S6) and a cytoplasmic NH2- and COOH-terminus (Figure 1.8, B). The S5 and S6 segments of each α subunit form the central pore with the pore loop (P), the region that contains the signature GYG sequence for potassium selectivity localized between both segments. The first four transmembrane domains S1–S4 comprise the voltage-sensing domain (VSD) that detects changes in the transmembrane potential, leading to opening or closure of the channel. Within the VSD, S4 contains positively charged residues and is therefore considered to be a major part of

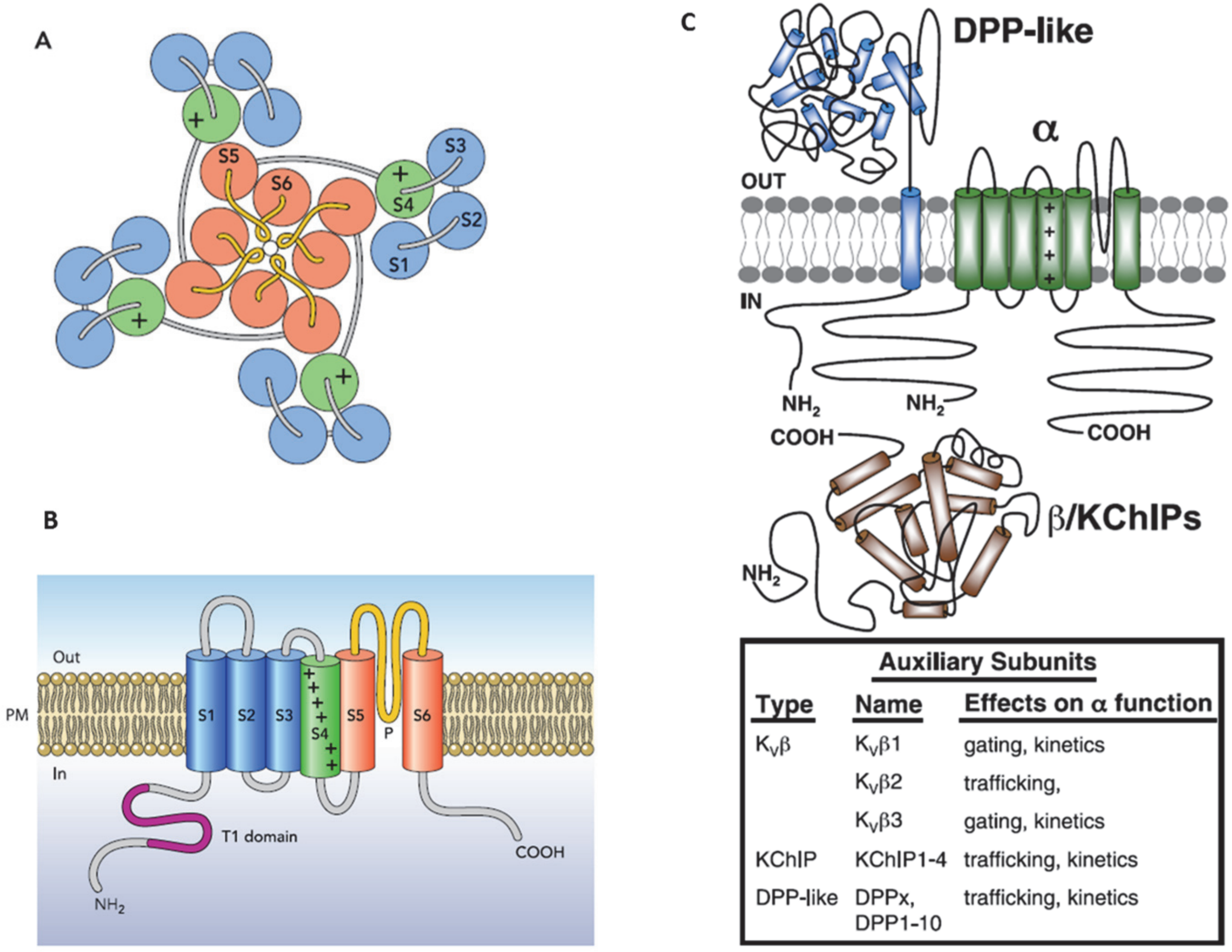

Auxiliary Subunits

Type	Name	Effects on α function
$K_V\beta$	$K_V\beta1$	gating, kinetics
	$K_V\beta2$	trafficking,
	$K_V\beta3$	gating, kinetics
KChIP	KChIP1-4	trafficking, kinetics
DPP-like	DPPx, DPP1-10	trafficking, kinetics

Figure 1.8. Depiction of the structure of a voltage-gated potassium (Kv) channel principal and auxiliary subunits. (A). A top view of a Kv tetramer in which the four subunits are arranged around a central pore. **(B).** Right a side view of an α subunit consisting of six transmembrane segments (S1-S6) and an intracellular NH2 and COOH terminus. The tetramerization domain T1 is situated on the NH2 terminus (Bocksteins and Snyders, 2012). **(C).** Schematic representation a single Kv subunit, four of which assemble to form functional Kv channels. Native channels also comprise auxiliary Kvβ (Kv1 subfamily) or KChIP and DPP-like (Kv4 family) subunits (Vacher et al., 2008).

voltage sensor. This domain detects a change in voltage across the membrane and its movement causes a conformational change in the channel, thereby opening or closing the channel. The NH2-terminus of Kv1–Kv4 subunits contains the tetramerization domain T1, which facilitates the assembly of α subunits into functional channels (Bocksteins et al., 2009b). In addition, the T1 domain restricts formation of homo- and heterotetramers by preventing tetramerization between incompatible subunits (i.e. subunits from different Kv1–Kv4 subfamilies). When four compatible T1 domains assemble, they arrange into the same four-fold symmetry as the transmembrane segments, forming a "hanging gondola" structure.

1.7.2 The auxiliary subunits

Native Kv channel complexes also contain a variety of auxiliary (both cytoplasmic and transmembrane) subunits (Figure 1.8, C) that are stable components of the channel complex. These subunits profoundly influence the functional properties of associated principal α subunits, and act as determinants of expression and localization of a channel (Vacher et al., 2008). For example, the bulk of Kv1 channel complexes in mammalian brains have associated Kvβ subunits. Four Kvβ subunit genes exist in the human genome. Inclusion of the Kvβ1.1 subunit in Kv channel complexes containing Kv1.1 or Kv1.2 dramatically alters the channel gating properties, converting the channels from sustained or delayed-rectifier type, to rapidly inactivating, or A type. In addition, another auxiliary subunit, KChIP, increases the surface density of the channel and slows the inactivation gating and speed of the recovery kinetics from inactivation when co-expressed with Kv4 channels.

Also, a transmembrane dipeptidyl-peptidase-like protein (DPPX) has been reported as an accessory subunit of native mammalian brain Kv4 channel complexes. Co-expression of different combinations of DPPX, KChIPs, and Kv4 subunits gives rise to A-type currents whose diverse biophysical properties match very closely the distinct properties of native somatodendritic A-type currents in different mammalian neurons (Vacher et al., 2008).

1.7.3 The silent subunits

Members of the Kv1–Kv4 subfamilies assemble into functional channels with a homotetrameric configuration. The functional diversity within these subfamilies is increased by forming heterotetramers with subunits of the Kv5, Kv6, Kv8, and Kv9 subfamilies. These latter Kv subfamilies are designated silent subunits because they fail to function as functional channels in a homotetrameric configuration and are retained in the endoplasmic reticulum (ER) (Ottschytsch et al., 2002; Ottschytsch et al., 2005). This retention is relieved by the selective co-assembly with members of the Kv2 subfamily in which the silent Kv subunits modulate the Kv2 currents by reducing the current amplitude, altering the inactivation and deactivation kinetics and shifting the voltage dependence of inactivation toward more hyperpolarized potentials.

Kv6.4 belongs to the Kv6 subfamily of silent subunits. Unlike the well studied Kv1-Kv4 subfamilies that are able to form homotetramers, the silent subunits are less studied. However, their essential regulatory functions as modifiers of Kv1-4 subunits are gradually being uncovered. First cloned by Ottschytsch et al. (2002) from a human cDNA library, Kv6.4 is not capable of forming functional homotetrameric channels. However, it can heterotetramerize with Kv2.1 principle subunits to form functional Kv2.1/Kv6.4 channel complexes when co-expressed in cultured cells. They presumably form in a 3:1 stoichiometry, as deduced from Kv2.1/Kv9.3 channel complexes (Kerschensteiner et al., 2005). Kv6.4 exerts several changes in the biophysical properties of Kv2.1 in Kv2.1/Kv6.4 channel complexes: a decrease in the current density (Bocksteins et al., 2009b) and a hyperpolarizing shift in the voltage-dependence of inactivation by ~40 mV, but without any significant effects on voltage-dependence of channel activation (Ottschytsch et al., 2005). Recently, gating current recordings from mammalian cells expressing Kv6.4 and/or Kv2.1 demonstrated that the gating charge movement of Kv2.1/Kv6.4 heterotetrameric channels displayed an extra component around the physiological K+ equilibrium potential, characterized by a second sigmoidal relationship of the voltage-dependence of gating charge movement (Bocksteins et al., 2012). This provides a mechanistic basis for the modulation of Kv2.1 channel inactivation gating kinetics by silent Kv6.4 subunits.

In this work, a forward genetic screen using transposon-mediated mutagenesis screen generated a Kv6.4b mutant, which displayed developmental defects in embryonic brain ventricle. Functional analysis provides the first *in vivo* evidence that Kv6.4b plays an essential role in regulating embryonic brain lumen inflation by modulating neuroepithelial cell proliferation and maintaining neuroepithelium integrity, presumably through the formation of Kv2.1/Kv6.4 heterotetramers in the ventricular zone of zebrafish embryonic brain.

Chapter 2. Materials and Methods

2.1 Zebrafish husbandry and embryos handling

Wild-type zebrafish (AB strain), transgenic lines including Tg (Fli: EGFP) and Tg (Gata1: DsRed) were obtained from the Zebrafish International Resource Centre (ZIRC). The fish were kept in IMCB zebrafish facility in closed circulating water systems (Aquatic Habitats, USA and Aquarien-Bau Schwarz, Germany) maintained at 28.5°C, under a 14-h light/10-h dark cycle. Pair-wise crosses were set in the evening by placing fish in breeding tanks, which consist of a plastic box with a wire-mesh bottom inserted into a 1-litre transparent plastic tank. Male and female fish were separated by a removable plastic divider to control the time of spawning. The divider was removed the next morning to allow the fish to mate. Eggs would fall through the wire mesh insert and were retrieved by emptying the water in the tanks through a plastic sieve, after which they were immediately rinsed with tap water and transferred to a 90mm Petri dish containing egg water. They were then kept in an incubator maintained at 28.5°C until the desired stage. Embryos were staged according to Kimmel et al. (1995) and times of development were expressed as hours post fertilization (hpf) at 28.5°C.

2.2 Plasmid constructs and morpholinos

The pX vector, containing the full GBT mutagenesis cassette flanked by mini*Tol2* sequences, was kindly provided by Dr. Stephen Ekker (Sivasubbu et al., 2006). All cDNA sequences of *kcng4a*, *kcng4b*, and *kcnb1* were obtained using Expand Long reverse transcriptase kit (Roche Diagnostics, Germany) using RNA isolated from wild type zebrafish embryos (AB strain) as template. RNA was isolated from pooled embryos at 24 hpf using the RNeasy kit

(Qiagen, the Netherlands). Typically about 100 embryos were snap-frozen in liquid nitrogen and homogenized in 350μl of buffer RLT. The rest of the protocol was performed in accordance with the manufacturer's guidelines.

Full length *kcng4b* was cloned into pTNT vector (Promega) using primer pair 5'-CCG CTCGAG GCCACC ATGCCCATCATCAGCAATG-3' and 5'-TGC TCTAGA TCAGATATCTTTGCAACATGC-3' with XhoI/Xba resctriction sites (underlined). Full length *kcnb1* was cloned into pCS2+ vector using primer pair 5'-CGC GGATCC GCCACC ATGGAGAAACCCTCGGCA-3' and 5'-CCG CTCGAG TCAAAGGCCCTTATCAAAAG-3' with BamHI/XhoI restriction sites (underlined). All PCRs were performed using Turbo pfu high fidelity polymerase (Stratagene) with standard protocols. Full length *kcng4a* cDNA was cloned into pGEM-T vector (Promega) by Dr Igor Kondrychyn (unpublished). The pEGFP-hKv6.4 plasmid, containing full length human kcng4 sequence tagged by EGFP at the C terminus, was kindly provided by Dr. Elke Bocksteins (Bocksteins et al., 2009b). All mRNA used for injection was in vitro transcribed using plasmid of interest linearized at the 3' end with respective restriction enzyme as template. 5' capped RNA was synthesized with the mMessage T7/SP6 kit (Ambion, USA). The typical reaction volume was 20 μl; containing 1 μg of DNA linearized at the 3' end of the insert for sense RNA, 2 μl 10X Reaction Buffer, 10 μl 2X NTP/Cap, 2 μl Enzyme Mix and nuclease-free water. The reaction was incubated at 37°C for 2 hours followed by addition of 1 μl of RNase-free DNase I. The tube was then incubated for another 15 minutes at 37°C, after which the RNA was cleaned up using the RNeasy Mini kit.

Transient knockdown of *kcng4b* gene expression was performed using splice site blocking morpholino (5'-TGCATTCGCCCTGTAAAAGAACAAA-3') targeting *kcng4b* intron 2 exon 3 (I2E3) junctions. Standard control morpholino with antisense sequence 5'-CCTCTTACCTCAGTTACAATTTATA-3' was used as negative control. Morpholinos were designed by and purchased from GeneTools (USA). MOs were resuspended from lyophilized powder, and then diluted to 1 mM stock with water and stored at room temperature. The MOs were then diluted to the appropriate concentrations and injected into one-cell staged zebrafish embryos.

2.3 TAIL-PCR method for mapping of GBT insertion sites

Specific primers and arbitrary primers

TAIL-PCR was performed according to Liu and Whittier (1995) with modifications (Parinov et al., 2004). Only phenol/chloroform purified genomic DNA was used for TAIL-PCR. A set of three nested Tol2 transposon-specific primers, designed for both the 5' and 3' ends of the transposon including:

SP5-1: 5'-ACTGGGCATCAGCGCAATTCAATTG-3';

SP5-2: 5'-GACTGTAAATAAAATTGTAAGGAG-3';

SP5-3: 5'-TTGATTTTTAATTGTACTCAAG-3';

SP3-1: 5'-CTCAAGTACAATTTTAATGGAGTAC-3';

SP3-2: 5'-ACTCAAGTAAGATTCTAGCCAGA-3';

SP3-3: 5'-CCTAAGTACTTGTACTTTCACTTG-3';

and following set of arbitrary (AD) primers:

AD-3: 5’-WGTGNAGNANCANAGA-3’;

AD-5: 5’-WCAGNTGWTNGTNCTG-3’;

AD-6: 5’-STTGNTASTNCTNTGC-3’;

AD-11: 5’-NCASGAWAGNCSWCAA-3’.

were used. All primers used in TAIL-PCR were HPLC purified. The following primers mixtures (containing 2 μM specific primer and 20 μM AD primer) were prepared:

(1) for primary PCR: SP5-1/AD-3, SP5-1/AD-5, SP5-1/AD-6, SP5-1/AD-11, SP3-1/AD-3, SP3-1/AD-5, SP3-1/AD-6 and SP3-1/AD-11;

(2) for secondary PCR: SP5-2/AD-3, SP5-2/AD-5, SP5-2/AD-6, SP5-2/AD-11, SP3-2/AD-3, SP3-2/AD-5, SP3-2/AD-6 and SP3-2/AD-11;

(3) for tertiary PCR: SP5-3/AD-3, SP-3/AD-5, SP5-3/AD-6, SP5-3/AD-11, SP3-3/AD-3, SP3-3/AD-5, SP3-3/AD-6 and SP3-3/AD-11.

Nested PCR conditions

Primary PCR (8 separate reactions for each primers mix) reaction was set up with 10x PCR buffer – 2 μl, 10 μM dNTP - 0.4 μl, Primers mix (for primary PCR) – 5 μl, DNA – 2 μl Taq polymerase (5U/μl) – 0.3 μl, Water – 10.3 μl. PCR cyclings were performed with a thermocylcer (PTC 200, MJ Research) using conditions as follow: first denaturation: 94°C, 2 min, 5 cycles of (1) 94°C, 30 sec; (2) 62°C, 1 min; (3) 72°C, 2.5 min; then (1) 94°C, 30 sec (2) 25°C 3 min (3) Ramp: 0.30/sec to 72°C (4) 72°C, 2.5 min; then 15 cycles: (1) 94°C, 10 sec; (2) 61°C, 1 min; (3) 72°C, 2.5 min; (4) 94°C, 10 sec; (5) 61°C, 1 min; (6) 72°C, 2.5 min; (7) 94°C, 10 sec; (8) 44°C, 1 min; (9) 72°C, 2.5 min, followed by final elongation: 72°C, 5 min. After that, 2 µl of the primary reaction was diluted in 20 µl of water and 2 µl of the diluted the mixture was used for the secondary PCR.

Secondary PCR (8 separate reactions for each primers mix) reaction was set up with 10x PCR buffer – 2 µl, 10 µM dNTP - 0.4 µl, Primers mix (for secondary PCR) – 5 µl, DNA (diluted from primary PCR) – 2 µl, Taq polymerase (5U/µl) – 0.3 µl, Water – 10.3 µl. PCR cyclings were performed using conditions as follow: 15 cycles of (1) 94°C, 10 sec; (2) 61°C, 1 min; (3) 72°C, 2.5 min; (4) 94°C, 10 sec; (5) 61°C, 1 min; (6) 72°C, 2.5 min; (7) 94°C, 10 sec; (8) 44°C, 1 min; (9) ramping 1.50/sec to 72°C; (10) 72°C, 2.5 min, followed by final elongation: 72°C, 5 min. After that, 2 µl of the primary reaction was diluted in 20 µl of water and 2 µl of the diluted mixture was used for the tertiary PCR. The rest of the secondary PCR products were kept at 4°C for the final electrophoresis.

Tertiary PCR (8 separate reactions for each primers mix) reaction was set up with 10x PCR buffer – 2 µl, 10 µM dNTP - 0.4 µl, Primers mix (for tertiary PCR) – 5 µl, DNA (diluted from secondary PCR) – 2 µl, Taq polymerase (5U/µl) – 0.3 µl, Water – 10.3 µl. PCR cyclings were performed using conditions as follow: 30 cycles of (1) 94°C, 15 sec; (2) 44°C, 1 min; (3) ramping 1.50/sec to 72°C; (4) 72°C, 2.5 min, followed by a final elongation: 72°C, 5 min.

Gel electrophoresis separation and sequencing

After all the nested PCR reactions were complete, 18 μl of the secondary and 20 μl of tertiary PCR products were loaded on 1% agarose gel. The secondary and tertiary products obtained with the same combination of SP/AD primers were loaded sequentially side by side for ease of comparison (for example, SP5-2/AD3—SP5-3/AD3 then SP5-2/AD6—SP5-3/AD6 and so on). The tertiary product typically displayed a shift by 51 bp for 5' flanking fragment and 30 bp for 3' flanking fragments. Normally, a tertiary product was typically amplified in higher quantities. However, as four different AD primers in combination with only one specific primer (either from the 5' or 3' end) were used, the final gel picture was usually complex and sizes of fragments amplified from the different SP/AD combinations differed substantially. Therefore, all products from the "band shift" (either secondary or tertiary) plus well-amplified tertiary products (even if there is no amplification after secondary reaction) were cut and subjected to purification.

PCR products were purified using PCR purification kit (Qiagen, the Netherlands) and eluted in 50 μl of EB buffer (10 mM Tris-HCl, pH 8.5). Products were sequenced directly by using 11 μl for the sequencing reaction plus 8 μl of BigDye and 1 μl of sequencing primer. Primers for sequencing of secondary and tertiary PCR products included:

5'-end sequencing primer, 5'-CCCCAAAATAATACTTAAGTACAG-3'

(for the fragments amplified using the combination of SP5/AD primers)

3'-end sequencing primer, 5'-GTACTTGTACTTTCACTTGAG-3' (for the fragments amplified using the combination of SP3/AD primers). Sequences were then mapped by BLAT programme (Ensembl) with zebrafish genome sequences to determine the insertion sites.

2.4 Whole-mount in situ hybridization

Embryo fixation and treatment

Embryos of desired stages were dechorionated manually using a pair of 26 gauge hypodermic needles and fixed overnight at room temperature. Briefly, staged embryos were chilled on ice for 5 mins to straighten their body and fixed in 4% PFA (paraformaldehyde) /PBS (0.8% NaCl; 0.02% KCl; 0.0144% Na_2HPO_4; 0.024% KH_2PO_4, pH 7.4) for 12 to 24 hrs at room temperature. Embryos younger than 15 hpf were fixed before dechorionation and the chorion was removed afterwards. Embryos older than 16 hpf were dechorionated before fixation. After fixation, the embryos were washed in PBST (0.1% Tween-20 in PBS) three times for 5 mins each on a rotator followed by treatment with 10 μg/ml of proteinase K (Roche Diagnostics, Germany) in PBST at room temperature. Embryos were then washed in PBST three times for 5 mins each. Embryos were then transferred to pre-hybridization buffer (50% formamide; 5X SSC; 50 μg/ml heparin; 500 μg/ml torula RNA; 0.1% Tween-20; pH 6.0) and pre-hybridized at 68°C for 4-16 hours. After prehybridization, embryos were either stored temporarily at -20°C or used immediately for hybridization.

Preparing of anti-sense DIG probes

Around 10μg of plasmid DNA was linearized at the 5' end of the gene of interest by digestion with an appropriate restriction enzyme at 37°C for 2 hrs.

1μg of linearized DNA was used to synthesize the DIG probe. The reaction was performed at 37°C for 2 hrs in a total volume of 20 μl containing 1μg of linearized DNA, 2 μl of 10X transcription buffer (Ambion, USA), 2 μl of DIG RNA labelling mix (Roche Diagnostics, Germany), 1 μl of RNase inhibitor (40U/ μl) (Promega, USA), 2 μl of T7/SP6 enzeyme (Roche Diagnostics, Germany). Following this reaction, 1 μl of RNase-free DNase I (Ambion, USA) was used to digest the DNA template at 37°C for 15 mins.

To clean-up the synthesized DIG probe, RNAeasy mini kit (Qiagen, the Netherlands) was used. Briefly, the reaction volumne was adjusted to a volume of 100 μl with RNAse-free water. 10 μl of β-mercaptoethanol was added to 1 ml of RLT buffer. This was followed by the addition of 350 μl of the RLT buffer to the diluted RNA sample that was subsequently mixed with 250 μl of 96-100% ethanol. This whole volume was then transferred to an RNeasy mini spin column that had been inserted into a collection tube. The spin column and collection tube was spun at 10000 rpm for 15 sec. 500 μl of RPE buffer was pipetted into the spin column and spun at 10000 rpm for 15 sec. Flow through was discarded and replaced with another 500 μl of RPE buffer. The column was spun at 10000 rpm for another 2 min. The RNAeasy column was then removed and placed onto a new 1.5 ml Eppendorf tube and 30-50 μl of RNase-free water was added into the RNeasy column and allowed to stand for 1 min. DIG-labeled RNA probe was then eluted out by micro-centrifuging the column at 10000 rpm for 1 min. The RNA probe was either stored at -80°C or used immediately.

Hybridization

Around 2-4 μl of DIG-labelled riboprobe was diluted in 200 μl of pre-hybridization buffer. The probe was denatured by heating at 68°C for 5 min followed by 2 min on ice. The denatured probe was then added to pre-hybridized embryos and hybridization was allowed to occur in a circulating water bath at 68°C overnight. This was followed by extensive post-hybridization washes in (1) 50% formamide in 2X SSCT for 2 x 30 min, (2) 2X SSCT for 15 min, and (3) 0.2X SSCT for 2 x 30 min. All washes were carried out at 68°C. Embryos were then rinsed in maleic acid buffer (MAB) at room temperature and incubated in 10% blocking solution (Roche) in MAB for 1 hour at room temperature.

Colour development

This was followed by incubation in anti-DIG antibody conjugated to alkaline phosphatase (1:5000 in blocking solution) overnight at 4°C or 4 hours at room temperature. Subsequently, embryos were washed with MAB for 4 x 20 min each followed by rinses of 3 x 5 min each in freshly prepared detection buffer (100 mM Tris pH9.5, 5 mM $MgCl_2$, 100 mM NaCl). Finally, the signal was detected with the chromogenic substrates by adding NBT (NitroBlue Tetrazolium) (Sigma); 4.5μl of a 50mg/ml stock in 70% dimethyl formamide and BCIP (5-bromo-4-chloro-3-indolyl phosphate) (Sigma); 3.5μl of a 50mg/ml stock in DMF) in 1 ml of detection buffer. The staining reaction was allowed to proceed in the dark at room temperature for 30 min to one hour, and the progress of staining was monitored from time to time under a dissecting microscope. For control and mutant embryos, the staining procedures were initiated and stopped at the same time. The reaction was stopped by removal of the staining solution followed by washes in PBST 2 x 10 min each. The stain was fixed in 4% PFA/PBS for 20 min at room temperature, after which embryos were stored in a solution of 50% glycerol in PBS.

2.5 BODIPY-FITC labelling of embryonic brain ventricles

Bodipy ceramide FITC-conjugated (Invitrogen, USA) was dissolved in DMSO to a stock concentration of 5 mmol/l. Embryos were soaked in 50 nmol/l bodipy ceramide solution in egg water overnight in the dark at 28.5°C. The embryos were then washed, dechorionated and placed in wells in 1% agarose for confocal microscopy. Confocal imaging was performed using a Zeiss LSM700 laser-scanning microscope, using standard confocal imaging techniques.

2.6 Alkaline phosphatase staining of zebrafish vessels

Zebrafish embryos were treated with PTU to prevent melanization starting after 24 hpf by adding PTU to embryo growth medium. Embryos were fixed at 72 - 96 hpf in 1.5mL centrifuge tube with 1mL 4% PFA in PBS at room temperature for 30 minutes. After disposal of PFA, 1mL 50% MetOH/PBST were added and incubated for 5 minutes. After that, liquid was removed and 1ml of 100% MetOH was added into the tube, followed by incubation for 5 minutes. After that, liquid was replaced with 1mL chilled acetone and incubated for 30 minutes at -20°C. The liquid was then discarded, and embryos were washed with 100% PBST 2 X 5 minutes each followed by 3X 5 minutes in detection buffer detection buffer (100 mM Tris pH9.5, 50 mM Mg Cl_2, 20 mM NaCl, 0.1% Tween20). Colours were developed by adding substrates containing NBT (NitroBlue Tetrazolium) (Sigma); 4.5µl of a 50mg/ml stock in 70% dimethyl formamide and BCIP (5-bromo-4-chloro-3-indolyl phosphate) (Sigma); 3.5µl of a 50mg/ml stock in DMF) in 1 ml of detection buffer. Staining was allowed to happen by careful monitoring in 15-30 minutes in tubes protected from light (cover with aluminum foil or place in drawer), After staining was complete, embryos were washed with 3 X 5 mins with PBST, and post fixed with 4% PFA for 30mins. After washing with PBST, embryos were transfer to 50% glycerol for 5 minutes, then to 87% glycerol for storage and imaging.

2.7 Cryosectioning of zebrafish embryos

Fixed embryos were embedded in molten 1.5% Bacto-agar (Difco, USA) containing 5% sucrose in detached caps of 1.5 ml Eppendorf tubes. The embryos were oriented before the agar solidified. The solidified agar blocks were removed from the caps and trimmed according to the desired plane of section. They were then transferred to 30% sucrose solution and incubated at 4°C overnight for cryoprotection. Individual blocks were mounted onto chucks, pre-chilled at -20°C, coated with frozen OCT compound (Leica, Germany). The agar block was then covered with a drop of OCT and frozen by submerging only the stem of the chuck in liquid nitrogen. The frozen assembly was allowed to equilibrate in a cryostat (Leica, Germany) for an hour before sectioning at -25°C. Normally, 12µm sections were cut and mounted on poly-L-lysine coated slides (Menzel-Gläser, Germany). The slides were dried on a hot plate set at 42°C for 30 min to an hour. These were either temporarily stored at -80°C in slide boxes or processed for immunohistochemistry immediately.

2.8 Immunohistochemistry on sections

All incubations and washes were performed in a humid chamber to prevent evaporation. To perform immunohistochemistry on sections, a circle was drawn around the cryosections on the slides with a PAP pen (DAKO, Denmark). Sections were rehydrated with PBST 3 x 10 min and blocked for 1 hour with blocking reagent (Roche Diagnostics, Germany). The sections were then incubated with primary antibody overnight at 4°C, followed by washes with PBST 4 x 15 min and incubation for 2 hours at room temperature or 4°C overnight with Alexa Fluor-conjugated secondary antibody. Sections were washed again in PBST 4 x 15 min and mounted immediately for photography in VectaShield (Vector Labs, USA) after sealing with nail polish.

2.9 Whole mount immunohistochemistry

Fresh embryos were collected at appropriate stages and were fixed with 4% PFA/PBS overnight at RT. 5X PTU was added to prevent pigmentation for later stage embryos. The next morning, the embryos were washed in PBST thrice for 5 mins each and replaced with 100% methanol for storage at -20°C. Embryos were rehydrated in a stepwise fashion of decreasing MeOH concentration in 1X PBST (75%, 50%, 25% MeOH/1X PBST). To improve antigen retrieval by antibody, embryos were equilibrated in 150 mM Tris-HCl, pH 9.0 for 5 mins and heat treated at 70°C for 15 mins in a water bath. Embryos were washed with dH_20 twice for 5 mins each and treated with ice cold acetone at -20°C for 20 mins to improve permeability. Acetone was washed away by rinsing six times with 1X PBST for 5 mins each and replaced with blocking reagent (Roche Diagnostics, Germany) for at least an hour. Primary antibodies were added at appropriate working dilutions in PBDT (1X PBS, 1% BSA, 1% DMSO, 0.5% Triton-X100, ddH$_2$O) and incubated overnight in 4°C. After which, the primary antibodies were removed and washed with 1X PBST for 4 times at 20 mins each. Embryos were re-blocked with the same blocking reagent for another hour at room temperature. Alexa Fluor-conjugated secondary antibodies were added. Secondary detection was allowed to occur for at least 2 hours to overnight in 4°C. After that, the antibodies were removed and the same washing steps followed. To preserve staining, embryos were kept in 50% glycerol/50% PBST or Vectashield mounting medium (Vector Labs, USA) at 4°C until subjected to confocal microscopy analysis.

Primary antibodies used: anti-phosphohistone H3 (PH3, mouse antibody, Millipore, USA), anti-αPKC (rabbit antibody, Santa Cruz, USA). Secondary antibodies used: AlexaFluor-488 or AlexaFluor-555 (Invitrogen). All primary antibodies were used at a dilution of 1:200. All secondary antibodies were used at a dilution of 1:500. Staining with AlexFluor-555-conjugated Phalloidin and DAPI were performed at a dilution of 1:500 in PBST and by incubating with embryos for 15mins at room temperature, followed by washing with PBST for three times.

For cell proliferation quantification, PH3-labeled cells in each z-series of the midbrain-hindbrain boundary and hindbrain regions were counted and averaged. Average z-series areas of the regions were measured using ImageJ software, and by determining the approximate area occupied by each cell, total cell number and the percentage of labeled cells in each region were calculated.

2.10 Embryo mounting and imaging using bright-field microscopy

For imaging live embryos under a upright dissecting microscope (Olympus, Japan), embryos were anesthetized with tricaine and transferred to 3% methyl cellulose on a concaved glass slide and conveniently orientated by manipulating embryos by dissection needles under a dissection microscope. For flat specimen, the yolk of the selected embryo was removed completely with needles. The de-yolked embryo was then placed onto a slide with a small drop of 3% methyl cellulose and adjusted to a proper orientation by a needle. Excess liquid was removed with tissue paper. Digital images were taken using a camera mounted to an AX-70 microscope (Olympus, Japan) with iSolution lite ver. 7.8 imaging software supplied by the MicroOptics and processed using ImageJ software.

2.11 Fluorescent and Confocal Microscopy

Fluorescent expression in live transgenic embryos was visualized and documented using an Olympus SXZ16 or a Leica MZ FLIII stereomicroscope equipped for UV epifluorescence light source (ebq100, Leica). For confocal imaging, embryos were anesthetized and live-mounted in 2% low melting agarose in Mat-Tek confocal dish for inverted configuration of the confocal system. Embryos in agarose were covered with 1X egg water supplemented with PTU and tricaine and maintained at 28°C using the fitted thermostat chamber. Confocal images were acquired using Zeiss LSM700 scanning confocal systems (Carl Zeiss Inc., Germany) using lasers at appropriate wavelengths and bandpass filters. Z-stacks images were taken at desired intervals using a 10X Plan-Neofluar 0.3 objective and 63X water immersion objective. All images were collected using the ZEN 2009 lite version (Carl Zeiss Inc., Germany) software, and processed using ImageJ software.

Chapter 3. Results

3.1 *Tol2*-mediated gene-breaking transposon (GBT) cassette

To search for novel regulators of brain circulation, we took an unbiased approach by conducting a forward genetic screen. A *Tol2*-mediated ‘gene-breaking’ mutagenesis strategy was chosen due to its reported high efficiency in integration into zebrafish genome and strong gene ‘termination’ effect once integrated (Sivasubbu et al., 2006). The ‘gene-breaking’ transposon (GBT) mutagenesis cassette (Figure 3.1), kindly provided by Dr. Stephen Ekker, combines both protein trap and 3’-exon trap features. The protein trap contains an efficient carp β-actin exon1/intron1 splice acceptor (SA) and a strong polyA terminator ensuring disruption of transcripts upon integration into intronic sequences irrespective of the reading frame of the trapped gene. The 3’-exon trap consists of the carp β-actin promoter driving the ubiquitous expression of GFP followed by a carp β-actin exon1/intron1 splice donor (SD) sequences. This ensures ubiquitous expression of GFP ORF as a fluorescent marker for identification once the cassette is integrated regardless of expression status of the trapped gene. The whole cassette was flanked by mini-*Tol2* sequences, which allows for efficient integration in genome once co-injected with *Tol2* transposase mRNA into zebrafish one-cell stage embryos (Parinov et al., 2004). Therefore, the GBT-based forward genetic screen used in this study theoretically allows unbiased search for all candidate gene responsible for regulating brain circulation.

3.2 Statistics and summary of the insertional forward genetic screen

The GBT-mediated forward genetic screen was conducted in a standard way (Figure 3.2). As summarized in Table 1, the GBT cassette on a plasmid and

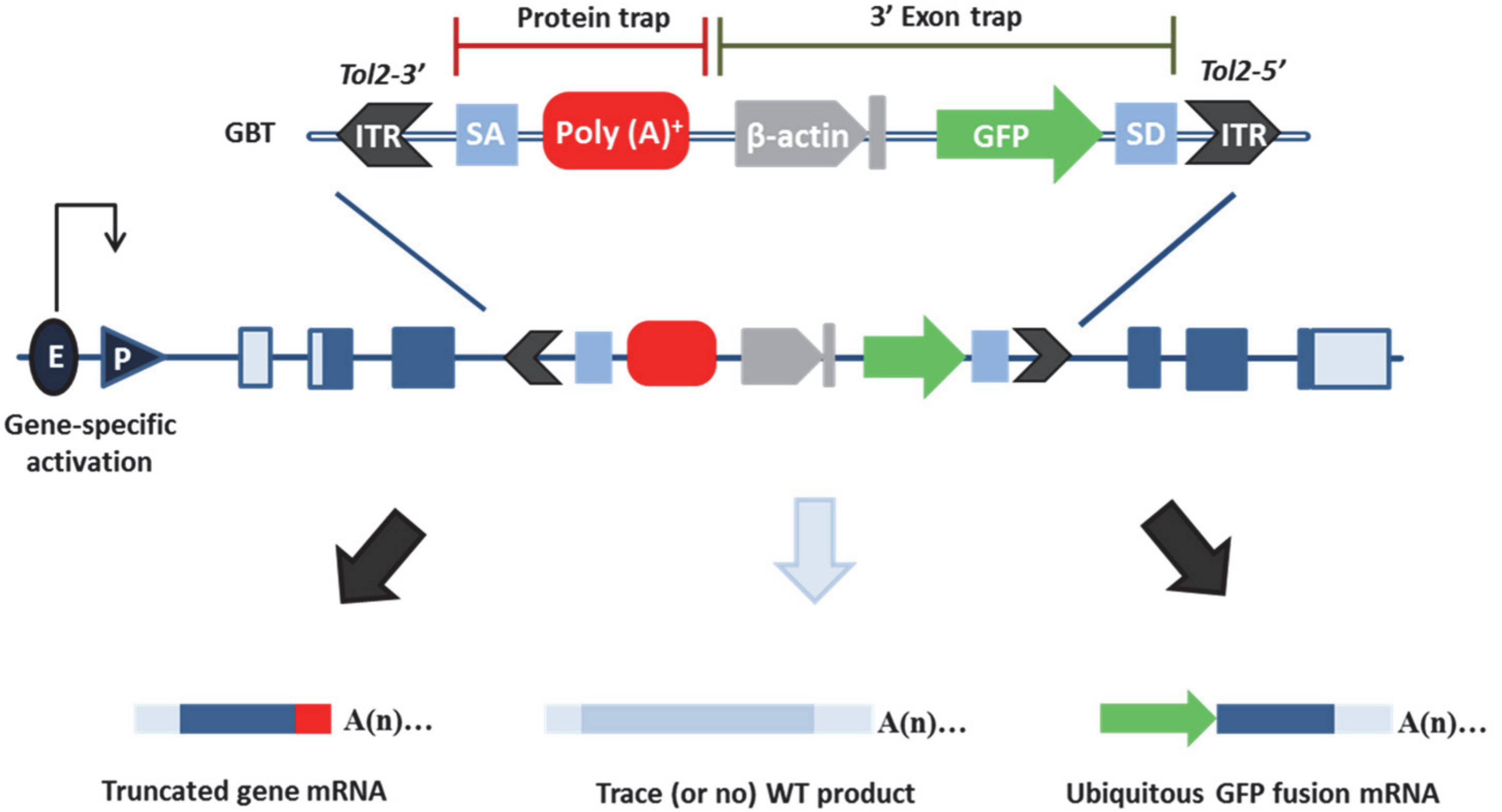

Figure 3.1. Schematic representation of the Tol2-mediated GBT vector composed of a protein trap cassette and a 3’ exon trap casette. ITR: inverted terminal repeat; **SA**, splice acceptor: **poly(A)**: polyadenylation signal with extra transcriptional terminator; **β-actin**: carp beta-actin enhancer, promoter, noncoding exon and intron 1 sequences; **SD**, splice donor; **E**, enhancer; **P**, promoter.

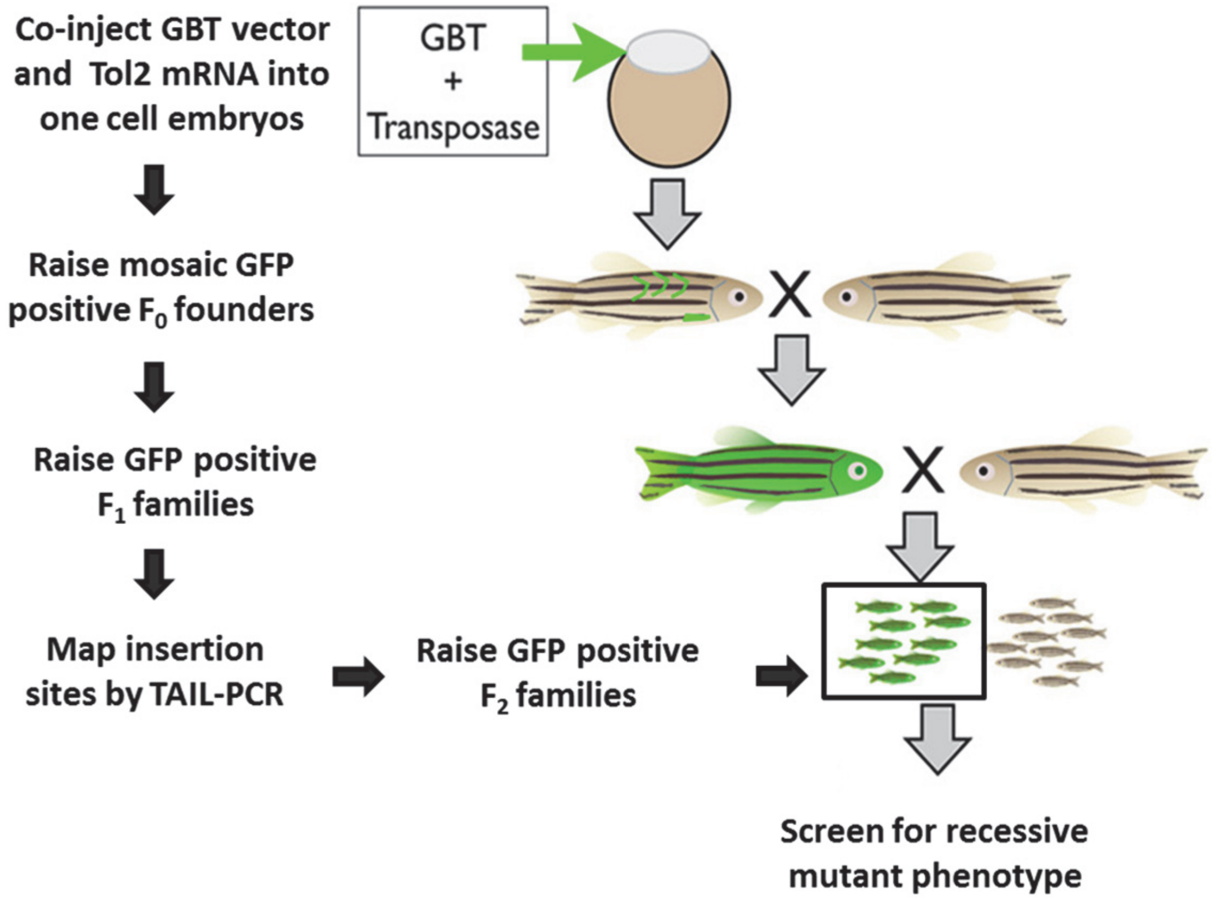

Figure 3.2. Schematic diagram of the protocol used to generate and screen for mutations using GBT vectors.

.

Table 1 Statistical summary of *Tol2*-GBT screen

Embryos injected	4347	Percentage of GFP positive embryos	n = 4347/697
GFP positive mosaic embryos	697	(after injection)	16%
Fish mated	350	Transgenesis rate	n = 61/350
Founder F_0 identified	61		17%
F_1 fish mapped by TAIL-PCR	87	No. of insertion sites per F_1 fish	n = 130/87
Insertion sites mapped	130		1.49
Within transcribed region	71	Percent of insertion sites located within the transcribed region	n = 71/130 54%
Insertions in Exon	4	Direct disruption of coding sequences	
Insertion located in intron with correct *cis* orientation	32	Potentially mutagenic according to GBT cassette's gene disruption mechanism	

Tol2 transposase mRNA were injected into 4347 one-cell staged zebrafish embryos and 697 of them showed mosaic GFP expression by 24 hpf. These embryos were selected and raised to grow into adults. When they reached adulthood, 350 were mated to wild type AB fish to screen for stable F_1 generations. Among them, 61 founders that had germ-line integration were identified. This number indicated a founder rate of 17.4%, which was reasonable in a forward screen setup. Among all founders used to establish F_1 families, a germline transmission rate ranging from 5% to 62% was observed, consistent with previous reports on the mosaic nature of cassette integration in the germline (Parinov et al., 2004; Sivasubbu et al., 2006; Urasaki et al., 2006). Due to this reason, unless otherwise stated, two fish from each subfamily were randomly chosen for mapping of GBT integration sites by TAIL-PCR method. This strategy allows maximizing the chance of mapping all possible integration sites while minimizing wasting effort in mapping of repeated insertion sites within the same F_1 subfamily.

All sequence mapping was conducted by BLAT against Ensemble zebrafish genome assembly. Upon the first round of 'raw' mapping, 130 insertion sites were identified (Appendix, Table 1). Among them, 71 insertions were found to be within transcribed regions. Also, 32 insertions were located in intronic sequences with GBT cassette having the correct *cis*-orientation with respect to the tagged gene (Table 2). These were selected as potential candidate mutants for in-cross to screen for recessive mutant phenotype. Four insertions in the exons were also identified. As insertion of the large GBT cassette into the exon causes direct disruption of coding sequences, these four insertions are mutagenic (Table 2). Although majority of the F_1 fish that had been mapped

Table 2. List of GBT insertions in introns with correct *cis*-orientation and exons

Family	F/M	Chr.	Nucleotide	Ori	Region	EntrezGene	Gene Name
GB2	F	9	20507646	+	Intron	hao2	Hydroxyacid oxidase 2 (long chain); zgc:63690
GB3	M	5	28196229	+	Intron	bco2a	beta-carotene oxygenase 2a, gene in reverse strand
GB4	F	7	59,166,786	+	Intron	kcng4	Potassium Voltage-gated channel, subfamily G, member 4
GB6	F	12	16188779	-	Intron	rnls	renalase, FAD-dependent amine oxidase; zgc:92286
GB8	F	5	66192334	-	Intron	anxalc	annexin A1c
GB8	M	9	14418062	-	Intron	BOS5P8_DANRE	human and mouse par-3 partitioning defective 3 homolog B
		3	30400051	-	Intron	rarab	retinoic acid receptor alpha b
GB10	M	9	13612198	+	Intron	fer1.6	fer1.6
GB19	M	17	6164025	-	Intron	zgc:162968	taxilin beta b (txlnbb)
GB21	M	19	45887390	-	Intron	zfpm2b	fog2
		1	51540469	-	Intron	spast	Spastin (SPG4)
GB25	F	2	38,401,308	+	Intron	si: ch211-119o8.5	Membrane, GTP binding, predicted
GB26	F	9	34609414	-	Intron	ildr2	Immunoglobulin-like domain containing receptor 2
GB27	M	2	41105313	-	Intron	BOV309_DANRE	BOV309_DANRE, gene in forwards direction
GB29	F	5	63009435	+	Intron	aspa	aspartoacylase
GB29	M	12	9769698	-	Intron	erbb2	Affects Schwann cell development, DRG formation
GB31	M	1	29,199,477	+	Intron	coro2a	Coronin, actin binding protein, 2A
GB31	F	9	17,190,689	-	Intron	myo1bl2	Myosin 1b-like 2
	F	2	20651394	+	Intron	aire	Insertion in 2nd transcripts in: B8A5S7_DANRE
GB36	F	4	9704423	+	Intron	flncb	flncb(EST)
GB37	M	17	40754171	+	Intron	LOC559917	MSH4
GB38	F	22	17734730	-	Exon	Polr2eb	Polymerase (RNA) II (DNA directed) polypeptide E,b
		21	32997806	+	Intron	zgc: 175145	zgc:175145
GB39	F	6	9280536	-	Exon	pglyrp2	Peptidoglycan recognition protein 2
GB39	M	3	38802936	+	Intron	gna12	Guanine nucleotide binding protein (G protein) alpha 12
GB40	F	24	36459061	-	Intron	zgc:171660	zgc:171660
GB40	M	19	39448166	-	Intron	asb4	Ankyrin repeat and SOCS box-containing 4
GB43	F	15	33210214	+	Exon	lsrl	Lsr like
GB43	M	2	53671163	+	Intron	zgc:153304	zgc:153304
GB44	F	7	15154427	+	Intron	pax6b	Pax6b
GB46	M	21	17767753	+	Intron	atp2a2b	ATPase, Ca++ transporting, cardiac muscle, slow twitch 2b
GB47	M	14	22272178	+	Intron	zgc: 66433	zgc: 66433
GB48	F	15	886441	+	Exon	LOC555761	FAM115A/C
GB59	F	14	9933075	+	Intron	tmem129	transmembrane protein 129
		1	30194560	-	Intron	si:dkey-7m11.2	KCNQ5
GB61	F	1	1010110	+	Intron	zgc:92834	N-6-adenine-specific DNA methyltransferase 1, N6AMT1

by TAIL-PCR had one or two insertions, some had more than two. A maximum number of five insertions in a single F_1 fish was observed in this screen (Appendix, Table 1).

As illustrated in Figure 3.2, F_1 fish that had insertion sites mapped by TAIL-PCR were out-crossed to establish respective F_2 subfamilies. This step helped to further segregate mutants with multiple insertions and also increased the heterozygote F_2 population to be in-crossed to screen for mutant phenotype. Since sequence information mapped by TAIL-PCR was available, specific primers pairs were used for genotyping of individual adult F_2 fish before their incross. Only carriers of insertions in correct *cis*-orientation with respect to the tagged gene and were able to segregate into single copy of insertion were in-crossed. Insertions tagging genes encoding metabolic enzymes were excluded from the screen.

Mutant phenotype screen was carried from day 1 to day 5 by looking for obvious morphological defects under a bright-field dissecting microscope. At least three in-crosses were made for each specific tagged gene to confirm the phenotype. Mutants that displayed interesting phenotype were further studied by transferring to appropriate transgenic background for analyzing specific structures or *in situ* hybridization for expression of certain morphological markers.

3.3 Examples of insertional mutants identified in the screen

3.3.1 GB44: *pax6b* mutant provides proof-of-concept evidence that insertional of *Tol2*- GBT cassette disrupts gene function

As a proof-of-concept that the insertional cassette causes mutations, we first looked at GB44 with insertion in the *pax6b* locus (Figure 3.3, A). Pax6 is a well-conserved transcription factor that plays key role in the development of eye, brain and pancreas in vertebrates. Pax6 has two DNA-binding domains, a paired domain and homeobox domain, and also a transactivation domain at the C-terminus. At least two ENU-mediated zebrafish *pax6b* mutant alleles are available. The *sunrise* (*sri*) mutant, harboring a missense mutant in the homeobox domain, displays a microphthalmia (small eye) phenotype with abnormal lens and cornea. The mutant displays a normal number of α and β pancreatic cells. Adult *sri* mutants are viable and fertile (Kleinjan et al., 2008). On the other hand, analyses of phenotype of a novel *pax6b* null mutant, $pax6b^{SA0086}$, demonstrated that in absence of Pax6b function embryos lost almost all β cells and the number of δ cells was strongly reduced and the number of ε cells significant increased in confirmation of a key role of *pax6b* in pancreatic endocrine cell differentiation (Verbruggen et al., 2010).

In this study, the GBT cassette was inserted in the intronic sequence of *pax6b* between exon 10 and exon 11. Based upon predication of the protein trap and 3'-exon trap function, this insertion should result in truncation of the C-terminal part of the transactivation domain. In addition, the carp β-actin promoter should drive ubiquitous GFP expression as a marker for identification of mutagenic insertion (Figure 3.3, B).

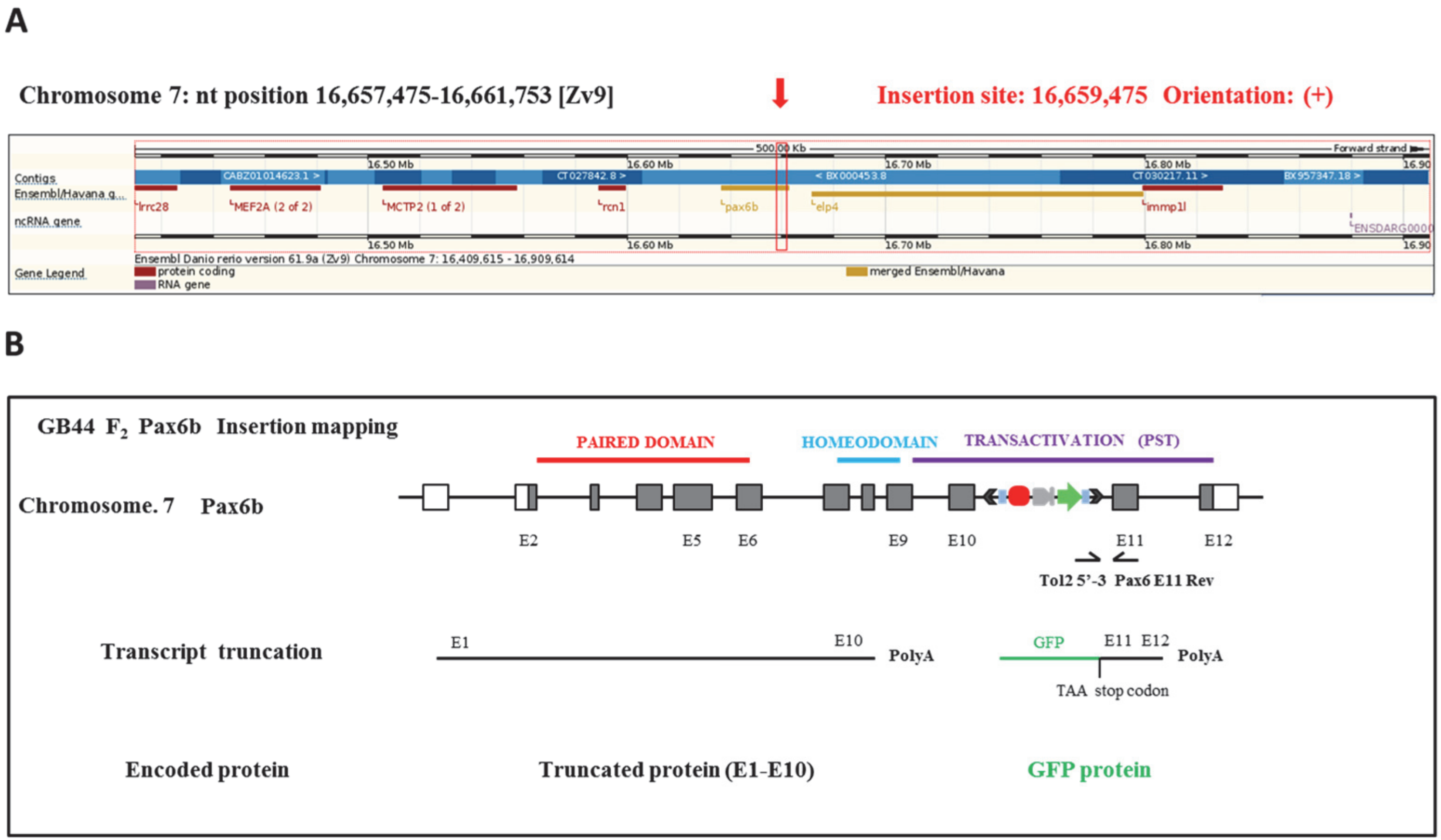

Figure 3.3. Schematic illustration of GBT insertion in the *pax6b* locus and its gene truncation mechanism. A. Illustration of insertion site in the *pax6b* locus of Zv9. **B.** Insertion of GBT cassette in intronic sequence between exon10 and exon 11 of *pax6b* gene leads to truncation of the C-terminal part of the transactivation domain. The carp β-actin promoter would drive ubiquitous GFP expression as a marker for identification.

GB44 homozygotes displayed a phenotype of microphthalmia (small eye) at 6 dpf (Figure 3.4, A, B). The number of embryos with phenotype followed mendelian distribution. Transverse section at the eye of 3 dpf larva with DAPI staining of the nuclei showed that *pax6b* mutant embryos had smaller lens, malformation of retinal layer and excessive cells at the ciliary marginal zone (CMZ) as compared to wild-type controls (Figure 3.4, C, D). Interestingly, the GFP expression pattern in *pax6b* mutant embryo was distinct from other GBT insertional lines in this screen, where GFP expression looked ubiquitous similar to actin expression. In contrast, in the GB44 line GFP expression was much higher in the eye and brain (Figure 3.4, E) in a pattern resembling native *pax6b* expression (Kleinjan et al., 2008). Two possible explanations exist for this phenomenon. Firstly, there could be some embedded *pax6b* enhancer sequences within the region nearby of the cassette such that during DNA and chromatin folding it enhanced the GFP expression through *cis*-activation of the carp β-actin promoter in the cassette. Alternatively, since the GFP transcript still retained the 3'-UTR sequence of native *pax6b* (Figure 3.3, B), it could be under regulation of certain regulatory elements driving expression of *pax6b*. Numbers of insulin-producing β-cells were also reduced in *pax6b* mutant embryos as shown by *in situ* hybridization of insulin transcripts (Figure 3.4, F, G).

In conclusion, these analyses of the phenotype of *Tol2*-GBT *pax6b* mutant are in concert with that of previously reported *pax6b* mutant alleles, thus providing proof-of-concept evidence that the *Tol2*-GBT cassette once integrated in correct *cis*-orientation into the zebrafish genome truncates the transcript and disrupts gene function.

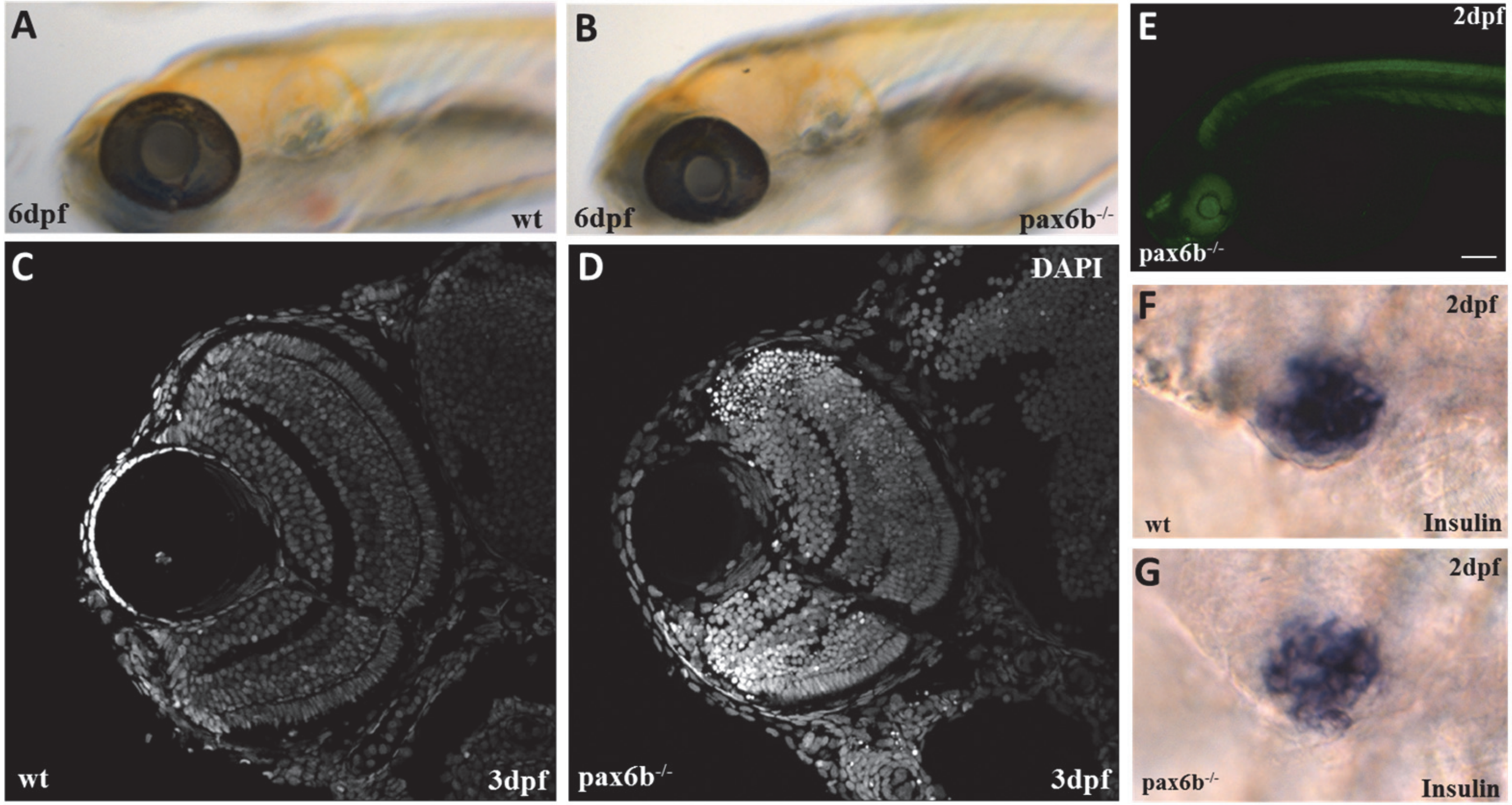

Figure 3.4. Phenotype of the insertional *pax6b* mutant embryos. A, B. Morphology of embryos at 6dpf under brightfield dissecting microscope. Homozygotes displayed a phenotype of microphthalmia (small eye). **C, D.** Transverse section at the eye region of 3dpf larva with DAPI staining of the nucleus. **E.** Intensified GFP expression at the eye and brain region in the GB44 *pax6b* line. **F, G**. *in situ* hybridization of insulin transcripts at 2dpf.

3.3.2 GB26: *ildr2* mutant embryos develop pericardial edema

GB26 line had insertion in the immunoglobulin-like domain containing receptor 2 (*ildr2*) locus (Figure 3.5, A). GBT cassette insertion was mapped in between exons 2/3, which could result in truncation of a large part of the C-terminal part of the protein (Figure 3.5, B).

Homozygous *ildr2* embryos showed no obvious heart defect at 1 dpf, such as initial heart looping and pumping (data not shown). However, mutant embryos developed severe pericardial edema at 2 dpf (Figure 3.6, A, B), although pumping of both atrium and ventricle continued. From all inter-crosses made so far, around 25% of progenies from heterozygous parents showed a phenotype in blood circulation, implying 100% phenotypic penetrance.

To better characterize the circulation defects, the mutant allele was transferred into Tg(Gata1a:DsRed) transgenic background, in which erythrocytes (red blood cells) were marked by DsRed fluorescent protein. By confocal imaging, it was shown that the majority of erythrocytes were stuck at the pericardial region of the *ildr2* mutant embryos at 2 dpf; very few erythrocytes were circulating (Figure 3.6, C-F).

Interestingly, the pericardial edema seemed to be reduced from 3 dpf onwards, indicating that the function of *ildr2* is essential within a developmental 'time window' around 2 dpf. Although a function of *ildr2* has been less studied in zebrafish so far, Watanabe et al. (2013) reported that ildr2 levels were reduced in diabetes susceptible DBA mice. Livers in ildr2 knockdown mice were steatotic, with increased hepatic and circulating triglycerides and total

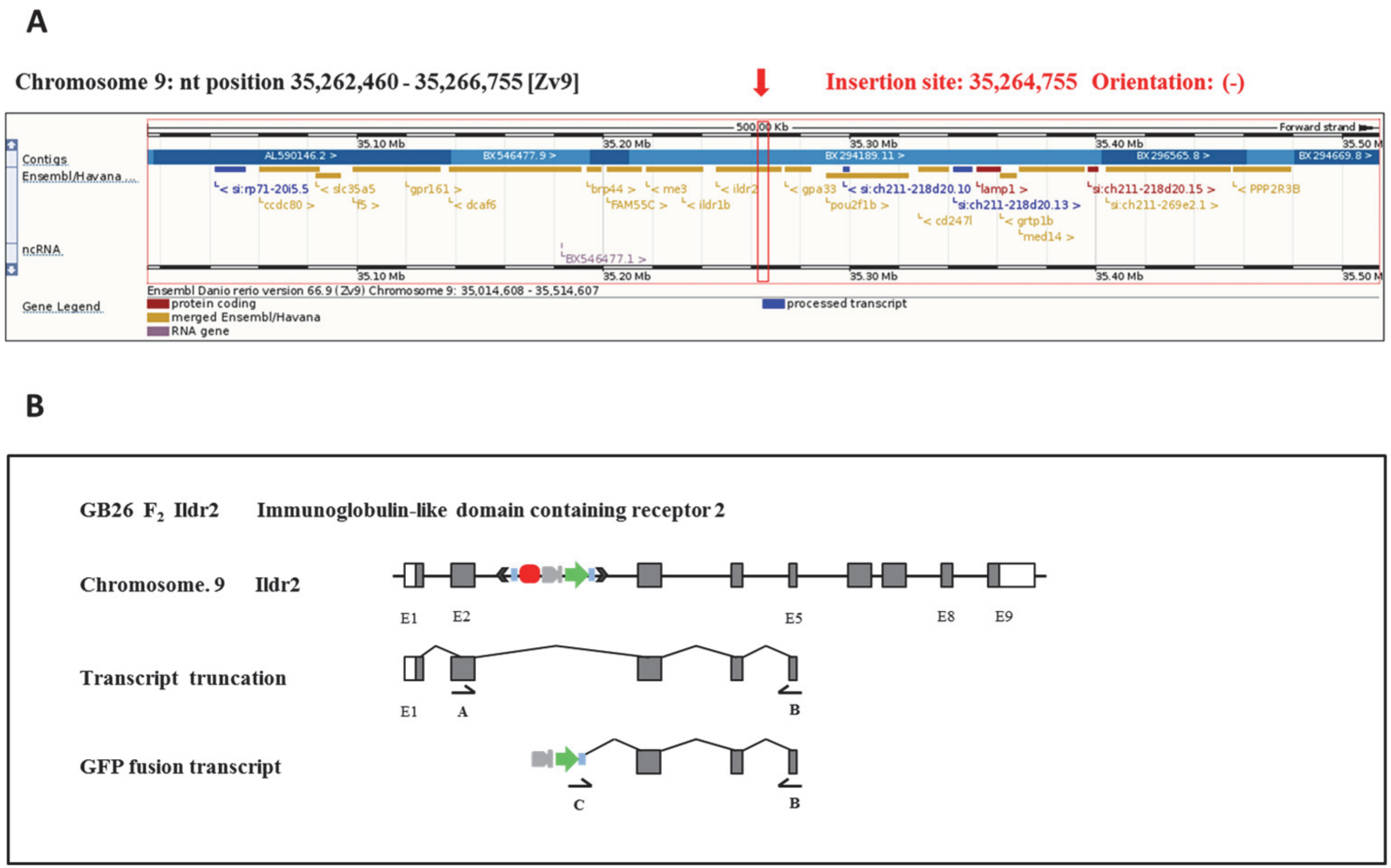

Figure 3.5. Schematic illustration of GBT insertion in the *ildr2* locus and its gene truncation mechanism. A. Illustration of insertion site in the *ildr2* locus of Zv9. **B.** Insertion of GBT cassette in intronic sequence between exon2 and exon 3 of *ildr2* gene leads to truncation of majority of the C-terminal part of the protein. The carp β-actin promoter would drive ubiquitous GFP expression as a marker for identification.

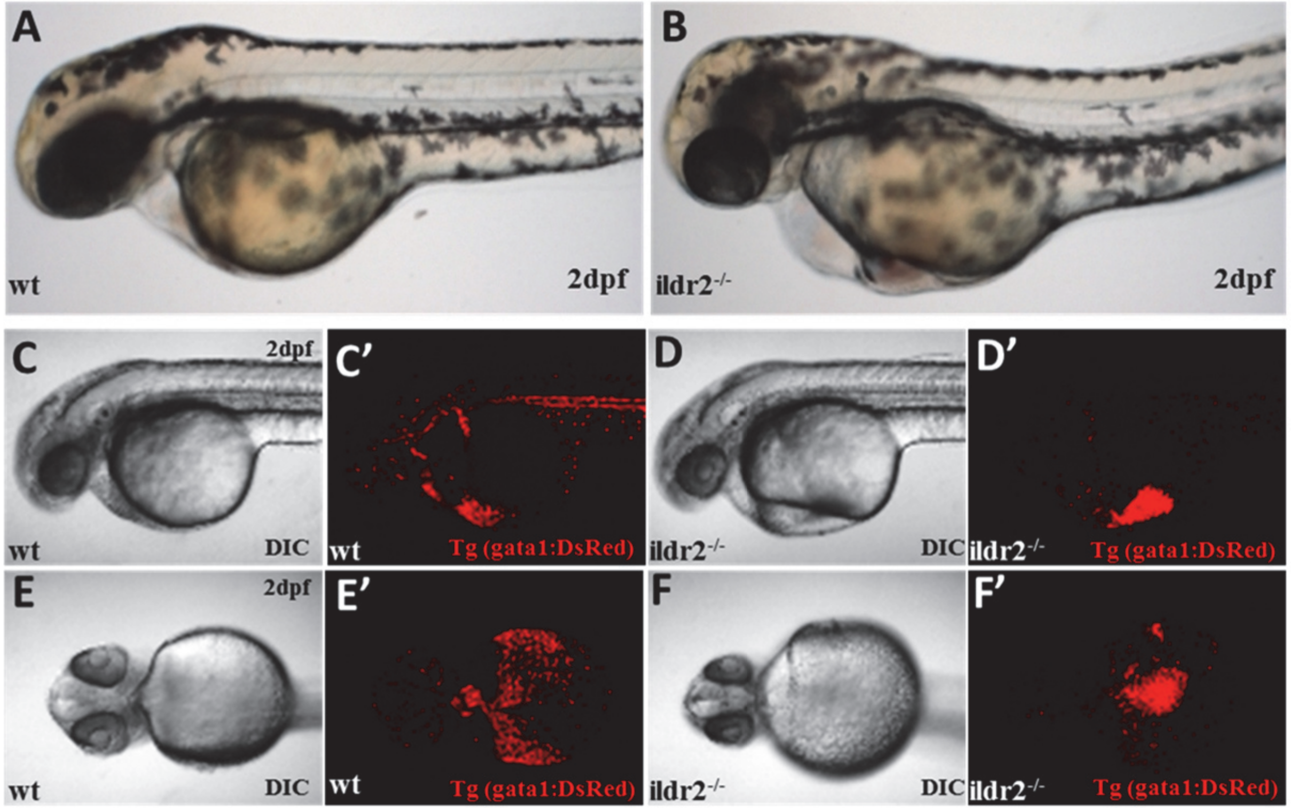

Figure 3.6. Phenotype of *ildr2* mutant embryos. A, B. Morphology of embryos at 2dpf under brightfield dissecting microscope. Homozygous mutant embryos developed severe pericardial edema. **C-F.** Majority of the erythrocytes were stuck at the pericardial region of the *ildr2* mutant embryos at 2dpf. Little erythrocytes were left in circulation. C, D**.** DIC images, lateral view. C’, D’. Corresponding confocal images. E, F. DIC images, ventral view. E’, F’. Corresponding confocal images.

cholesterol. Increased circulating VLDL, without reduction in triglyceride clearance suggested an effect of reduced hepatic ILDR2 on hepatic cholesterol clearance. In animals that overexpress ildr2, hepatic triglyceride and total cholesterol levels were reduced. Higashi et al. (2013) showed that two LSR-related proteins, immunoglobulin-like domain-containing receptor (ILDR) 1 and ILDR2, are also localized at tricellular contacts (TCs) and recruit tricellulin, although the barrier function of ildr2 is much weaker as compared to ildr1. In human, mutation in a related gene, *ILDR1*, causes a familial deafness, DFNB42 (Borck et al., 2011). The authors provided evidence that mutant proteins were defected in recruiting tricellulin, suggesting tricellulin recruitment to tight junction is required for hearing. Whether *ildr2* has conserved function in zebrafish in regulating lipid metabolism or whether it is involved in tight junctions to provide tissue barrier function is still unknown, and the exact mechanism of how *ildr2* functions during zebrafish development remains to be elucidated. The *ildr2* insertional mutant allele generated in this screen thus provides a useful tool for further characterization.

3.3.3 GB43: *lsr* mutant: lipolysis stimulated lipoprotein receptor

Another interesting mutant that came out from this screen is GB43 that carries an insertion linked with *lsr*. This insertion is in an exon (Table 2), therefore directly disrupting the coding sequence of the gene. *lsr* encodes the lipolysis stimulated lipoprotein receptor. *lsr* was identified as a paralogue of *ildr2* (Dokmanovic-Chouinard et al., 2008), and both are homologues of human *ILDR2*. Therefore, two paralogues genes were identified together in one single insertional screen.

It has been reported that *lsr* expression was observed by *in situ* hybridization in the pancreas of zebrafish larvae at 48 and 72 hpf. Also, injection of morpholino against *lsr* caused a general delay in endodermal development and disruption of β-cell development, evidenced by a scattered β-cell phenotype. Injection of *ildr2* morpholino produced a less severe phenotype in terms of β-cell disruption， but also with endodermal development delay (Dokmanovic-Chouinard et al., 2008). The authors concluded that both paralogues might play an important role in endodermal development in zebrafish with specific effects on embryonic β-cells.

Although when crossed to homozygosis, GB43:*lsr* mutants showed no obvious morphological phenotype under bright-field microscope (data not shown), further characterization with molecular markers might reveal interesting phenotypes especially when combining the studies with analyses of its paralogue, the GB26:*ildr2* mutant.

3.3.4 GB8: *pard3b* mutant embryos displayed pigment formation defects

The GB8 line has an insertion in the *pard3b* (par-3 partitioning defective 3 homolog B) locus in Chr.9. Like many other zebrafish genes, there are two paralogues of *pard3b* in zebrafish, the other located in Chr.1. Neither has been studied so far. *In situ* hybridization revealed that *pard3b* (Chr.9) is expressed exclusively in the pronephric duct of zebrafish embryos (Dr. Igor Kondrychyn, unpublished).

GB8: *pard3b* mutant displayed pigment formation defects as early as pigmentation started to develop at 1 dpf. When wild-type zebrafish started to show visible pigment formation at eyes, head and trunk skin, no pigment formation could be observed in *pard3b* mutant embryos (Figure 3.7, A, A'). In mutants, pigment started to appear progressively later from 2-6 dpf, although both the intensity of the pigment and distribution of pigment cells were much reduced as compared to wild type embryos. For example, the dorsal stripe started to appear in the mutant at 2 dpf, but the lateral strip parallel to the horizontal myoseptum and the ventral stripe appeared at a much later stage (Figure 3.7, B-H). At higher magnification, melanophores were visible with no obvious cell shape defects (data not shown). Yellow pigment forming xanthophores were present in the mutant.

Similar to other zebrafish mutants with pigment formation defects, *pard3b* mutants were able to develop to term and were sexually fertile. Adult *pard3b* homozygote fish displayed phenotype typical of melanin formation defects as evidenced by its red retina and lack of black stripes. However, unlike *nacre* mutant (Lister et al., 1999), which had a complete lack of melanocytes due to mutation in the *mitfa* gene, *pard3b* mutant phenotype was milder. It had visible pale-coloured stripes interspersed by the yellow stripes of xanthophores. This was also consistent with the embryonic phenotype evidence by reduced but not complete lack of melanin formation.

In zebrafish, embryonic pigment pattern is formed by cells derived from neural crest cells that migrate along specific pathways to their final position in the embryo (Moreira and Deutsch, 2005). This process is generally completed by 6 dpf. During the larva-to-adult metamorphosis occurring from the second to the fourth week, larval pigment pattern is generally replaced by the adult

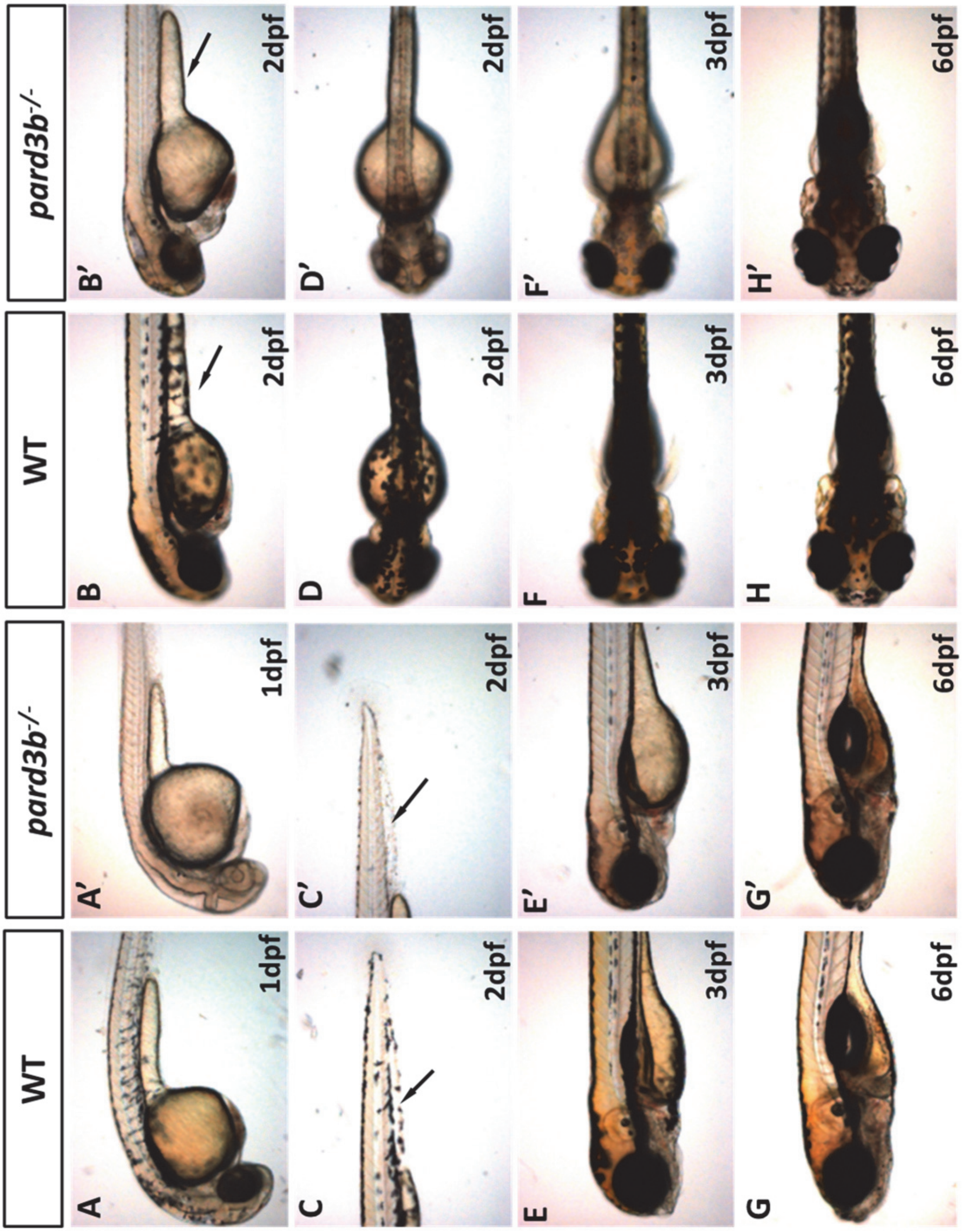
WT
pard3b$^{-/-}$
WT
pard3b$^{-/-}$
A
1dpf
A’
1dpf
B
2dpf
B’
2dpf
C
2dpf
C’
2dpf
D
2dpf
D’
2dpf
E
3dpf
E’
3dpf
F
3dpf
F’
3dpf
G
6dpf
G’
6dpf
H
6dpf
H’
6dpf

Figure 3.7. Phenotype of *pard3b* mutant embryos. Homozygous *pard3b* mutant embryos displayed pigment formation defects. **A-H**. Morphology and pigment pattern of wild type embryos from d1-d6 under brightfield dissecting microscope. A'-H'. Morphology and pigment pattern of homozygous *pard3b* mutant embryos from d1-d6 under brightfield dissecting microscope. Notice the difference of pigment of the ventral strip and yolk sac strip between wild type and mutant embryos (arrowed).

pigment pattern. Our analyses revealed that *pard3b* regulates pigment formation in both embryonic and adult stages, although the exact mechanism of how *pard3b* regulates pigment formation in zebrafish remains to be elucidated. In this regard, detailed characterization of pigment pattern in mutant embryos and adults are required. The homozygote viable *pard3b* mutant thus provides an excellent model for such studies.

3.3.5 GB21 mutant: heart and brain ventricle defects

GB21 mutant has two insertional sites mapped by TAIL-PCR (Appendix, Table 1). However, several other difficult to read sequences generated that were not helpful to map the insertion by BLAT are therefore not shown. The exact insertional site could not be confirmed by using specific primer pairs due to repetitive false positive results. Other possible insertion site(s) may exist as well. To confirm the identity of insertion sites additional out-crosses and detailed mapping are necessary.

Although mapping is incomplete, GB21 mutant displayed an interesting phenotype. No obvious morphological defects were observed before 24 hpf. However, starting from ~26 hpf onward, mutant embryos showed small heart and highly underinflated brain ventricle, with obvious midline separation defects in the fourth ventricle. Embryonic tail curved dorsally (Figure 3.8, A, A’). At day 2, mutant embryos displayed eyes with spotty retinal pigmented epithelium (RPE) and yolk dented by pericardial edema (Figure 3.8, B, B’). Shorter head and heart defects were observed at day 3 (Figure 3.8, C, C’). GB21 mutant displayed phenotype similar to *has* (*heart and soul*) mutant, which had a mutation in *pkci* (protein kinase C, iota) (Horne-Badovinac et al.,

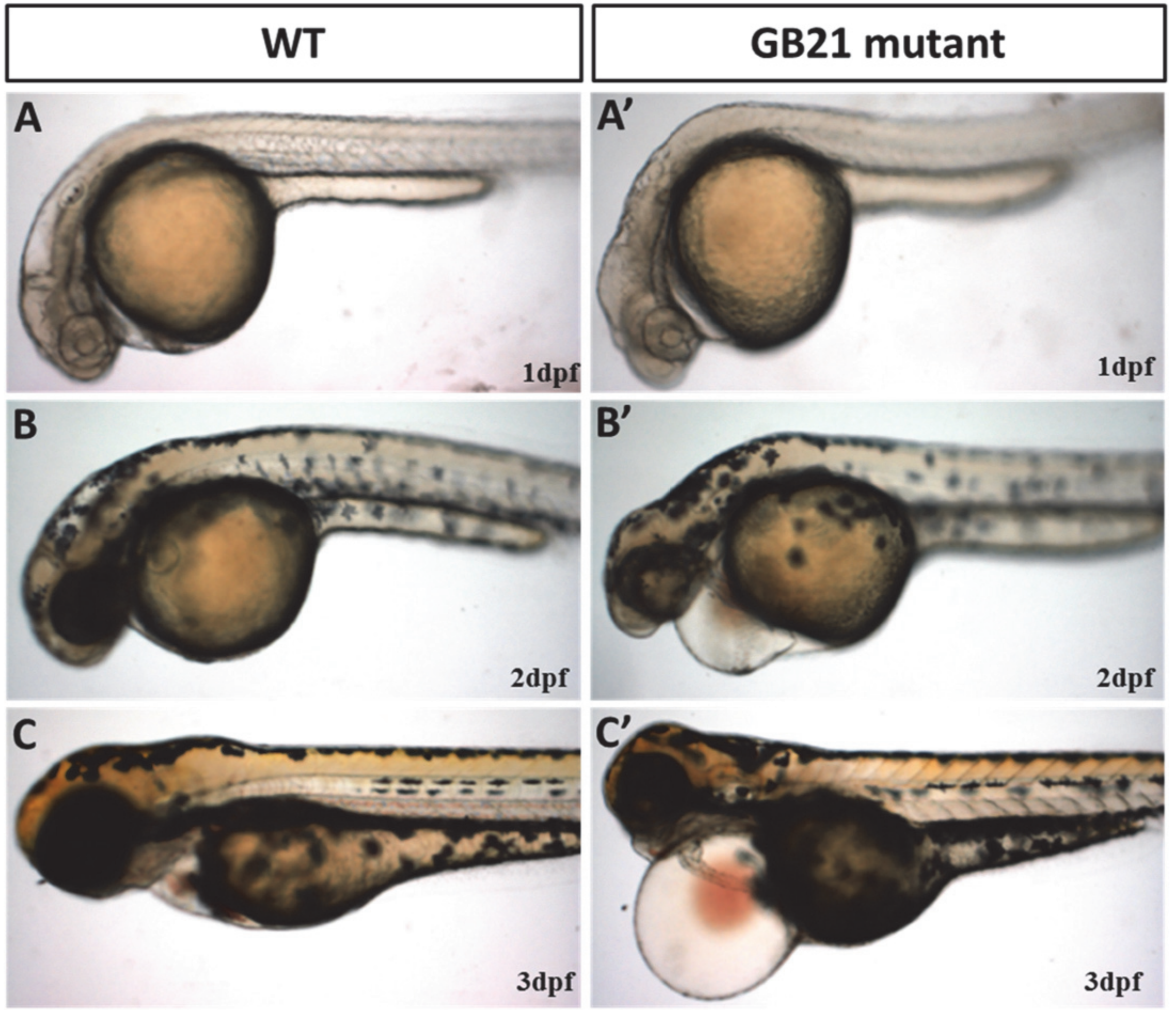

Figure 3.8. Phenotype of GB21 mutant embryos. A-C. Morphology of wildtype (A-C) and mutant embryos (A'-C') from d1-d3 under brightfield dissecting microscope. Mutant embryos displayed eyes with spotty retinal pigmented epithelium (RPE) and yolk dented by pericardial edema at d2 and shorter head and heart defects at d3.

2001). The initial heart circulation-independent brain ventricle inflation, occurring at 17-21 hpf (Lowery et al., 2009), was not affected in GB21 mutant. However, later brain ventricle expansion, which is heart circulation dependent, was affected in GB21 mutant. Indeed, the zebrafish *heart and soul* (*has*) is required tissue-autonomously within the myocardium for normal heart morphogenesis (Rohr et al., 2006). Thus, it could be hypothesized that the brain ventricle phenotype observed in GB21 mutant might be a consequence of heart developmental defects. Due to this reason and its unresolved insertion site, this mutant was not selected for further characterization in this study, although it is definitely an interesting mutant for future studies.

3.4 Functional characterization of *kcng4b* mutant

3.4.1 GB4: mutant has insertion in the *kcng4b* locus

The GB4 line has insertion in the *kcng4b* locus of Chr.7 (Figure 3.9, A). The GB cassette was mapped with correct *cis*-orientation between E2 and E3 of *kcng4b*, the only two coding exons of the *kcng4b* gene, which encodes a protein that consists of 535 amino acid (aa) residues. Based on the design and mechanism of function of the GBT cassette (Figure 3.1), the insertion should cause truncation of the protein resulting in a polypeptide of only the N-terminal half (containing only coding exon 2) of 249 aa residues. Based on Kcng4b protein domain structure, a peptide with the first 249 aa residues of Kcng4b comprise the T1 domain and S1 domain, whereas lacks S2-S6 as well as the pore domain. This truncated peptide thus could not form a functional silent subunit. As the stop codon of GFP ORF still exists in the GFP and exon 3'-fusion transcript, the rest of the protein will not be encoded (Figure 3.9, B).

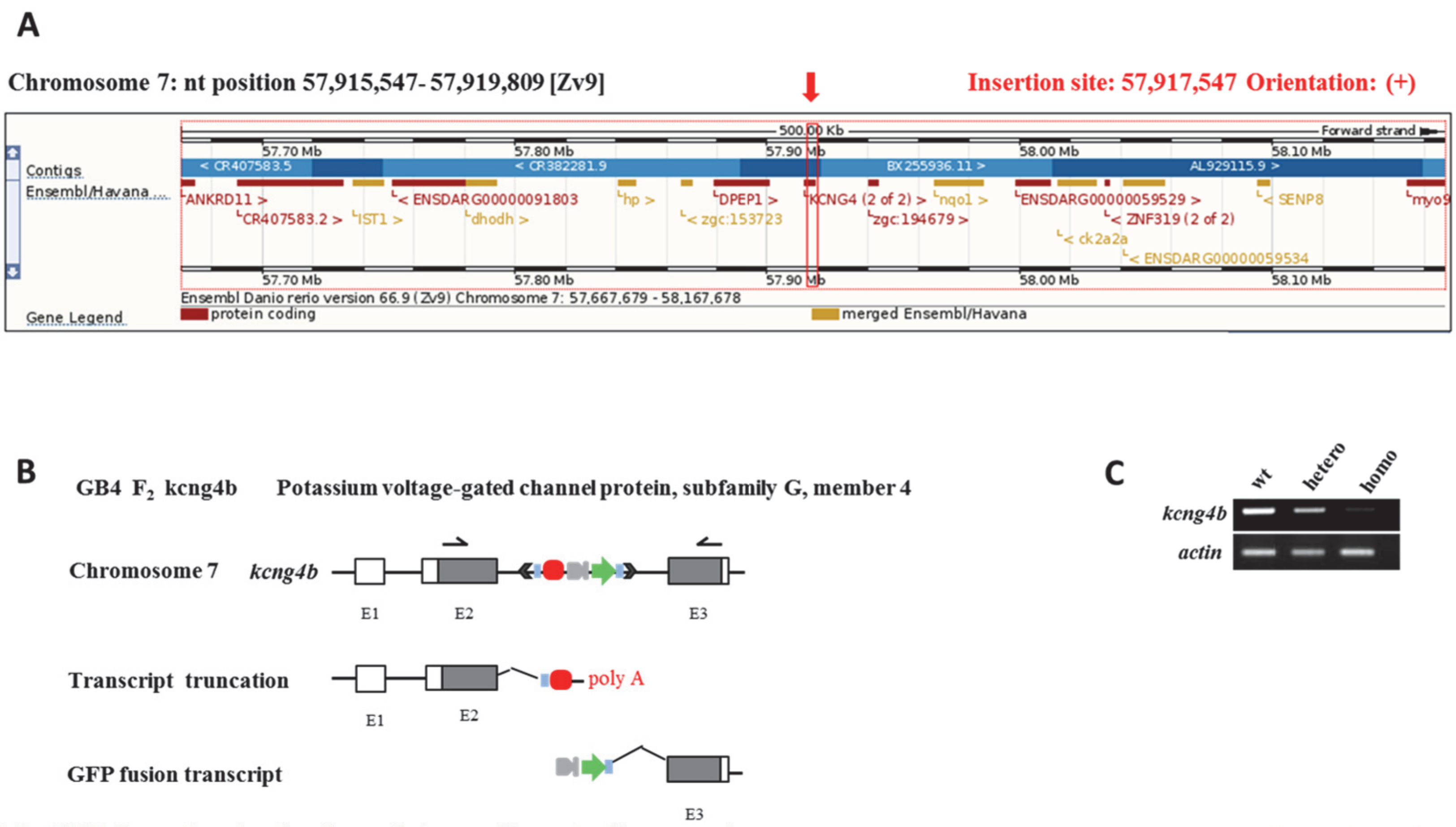

Figure 3.9. GBT insertion in the *kcng4b* locus disrupts the gene function by truncating the transcripts. A. Illustration of GBT insertion site in the *kcng4b* locus of Zv9. **B.** Schematic illustration of gene disruption strategy of GBT. Insertion of GBT cassette in intronic sequence between exon2 and exon 3 of *kcng4b* gene leads to truncation of the protein into only the N-terminal half of 249 amino acids, which comprises the T1 domain and S1 domain, whereas lacks S2-S6 as well as the pore loop. This truncated peptide thus could not form a functional silent subunit. **C**. RT-PCR detection of full length *kcng4b* transcripts in wild type, heterozygous and homozygous embryos, with actin as an internal control.

Reverse transcription polymerase chain reaction (RT-PCR) was performed to check the full-length transcripts in *kcng4b* heterozygote and homozygote embryos. As expected, full length *kcng4b* transcripts were decreased in heterozygote and almost absent in homozygote embryos (Figure 3.9, C), although trace amount of full length transcript was still detectable. This phenomenon was consistent with previous reports that GBT cassette would generally lead to a 95% knockdown effect of gene it inserted in (Sivasubbu et al., 2006), which usually is sufficient for loss of function.

3.4.2 Loss of *kcng4b* function caused embryonic brain ventricle defects

kcng4b mutant embryos displayed no obvious morphological defects at blastula and gastrula stages. However, mutant embryos displayed cells delaminating from the brain ventricular surface (ventricular zone) and aggregating inside the ventricle lumen around 20-24 hpf (Figure 3.10, A-D). At around 32 hpf, mutant embryos started to show a hydrocephalus phenotype, and developed an inflated brain ventricle around 48 hpf (Figure 3.10, E and F). In severely affected mutants, dents in the yolk close to the heart and short yolk extension were observed (Figure 3.10, F'), implying that apart from brain ventricles, *kcng4b* might have specific functions in circulation and endodermal development. No obvious brain necrosis was observed in mutant embryos until 24 hpf, indicating that the brain ventricular phenotype was not a result of cell death in the brain by apoptosis. As *kcng4b* developmental function was not analyzed and the mutant embryos showed brain circulation defects, which met the target for this screen, this mutant was selected for further functional characterization.

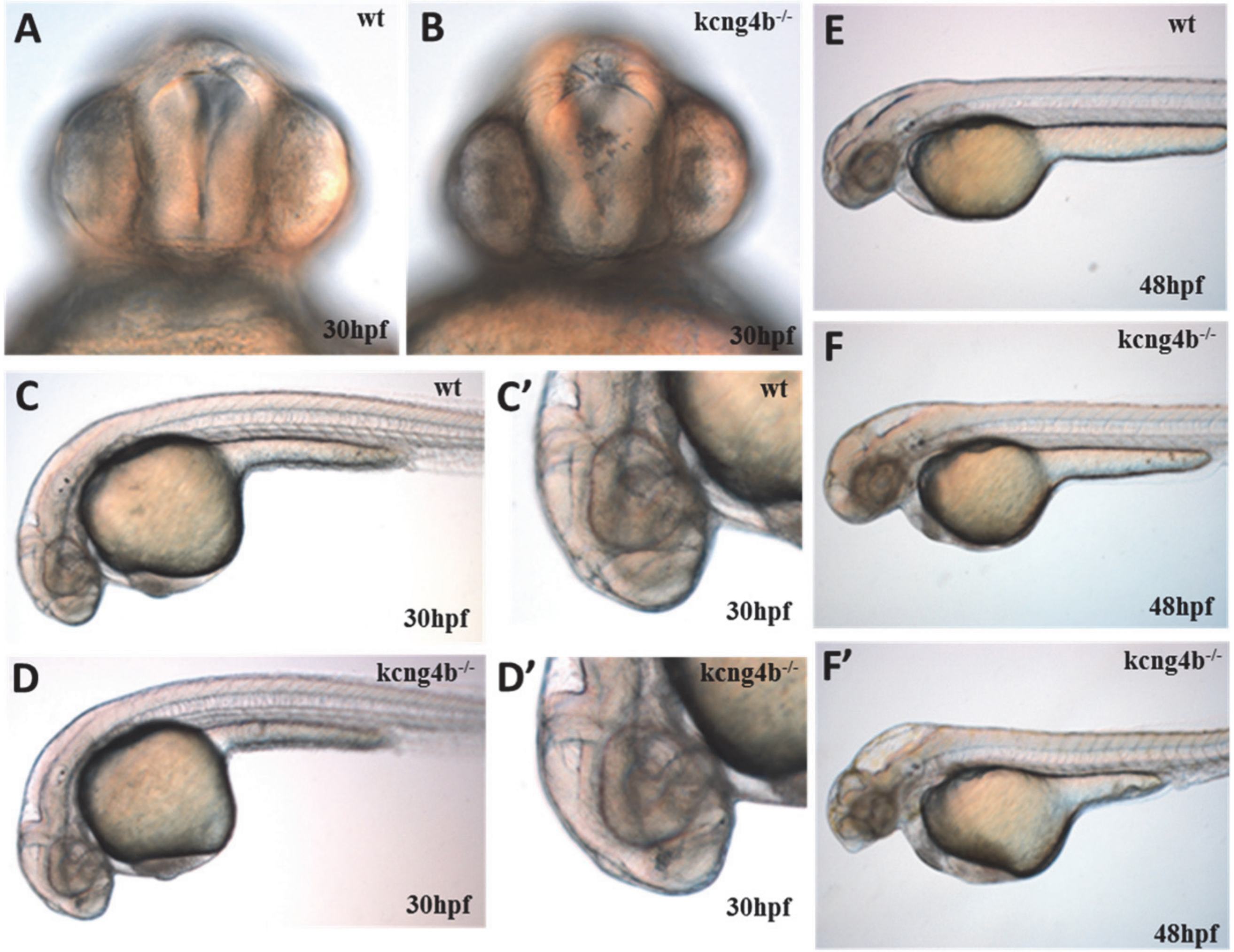

Figure 3.10. Phenotype of *kcng4b* mutant embryos. A-D. Mutant embryos displayed cells delaminating from the brain ventricular surface (ventricular zone) and aggregating inside the ventricle lumen. A,B, frontal view. C,D, lateral view. **E, F.** Mutant embryos displayed hydrocephalus phenotype, and developed highly inflated brain ventricles. F’. Severely affected mutant also displayed dented yolk and shorter yolk extension.

To verify whether the observed phenotype was indeed due to a loss of *kcng4b* function, we injected different doses of *kcng4b* splice site blocking morpholino (MO) into one-cell stage embryos. This morpholino targets the splice site of intron 2 and exon 3 (Figure 3.11, A) and causes a defect of splicing resulting in a transcript that retains the intron 2 sequence (Figure 3.11, B), which causes a truncation of the Kcng4b. In fact the protein truncation effect of this morpholino mimicked that of GB cassette insertion as both mutant and morphant will have only exon 2 sequences processed. The RT-PCR results confirmed that full-length *kcng4* transcripts were decreased in a dose-dependent manner in morphants (Figure 3.11, B).

As expected*, kcng4b* morphants displayed a phenotype that mimicked that of *kcng4b* mutants. At 24 hpf, an aggregation of cells delaminated from the ventricular zone was observed in forebrain lumen of morphant injected with a dose of 0.15 pmol of MO or higher (Figure 3.11, C). Morphants injected with 0.45 pmol of MO displayed dented yolks, short yolk extensions, and ventrally curved tails similar to that in severely affected mutants (Figure 3.10, F'). Consistently, the hydrocephalus phenotype could be observed around 48 hpf. Morphants that received a high dose of MO displayed severely inflated brain ventricles (Figure 3.11, C). Thus, a transient loss of Kcng4b function caused by MO injection confirmed that the brain ventricle defects observed were due to a loss of *kcng4b* function in the mutant.

3.4.3 Two paralogues of *kcng4* with distinct tissue specific expressions

Kcng4 encodes a potassium voltage-gated channel, subfamily G, member 4, or Kv6.4 in short. It has been demonstrated in cell culture experiments that in

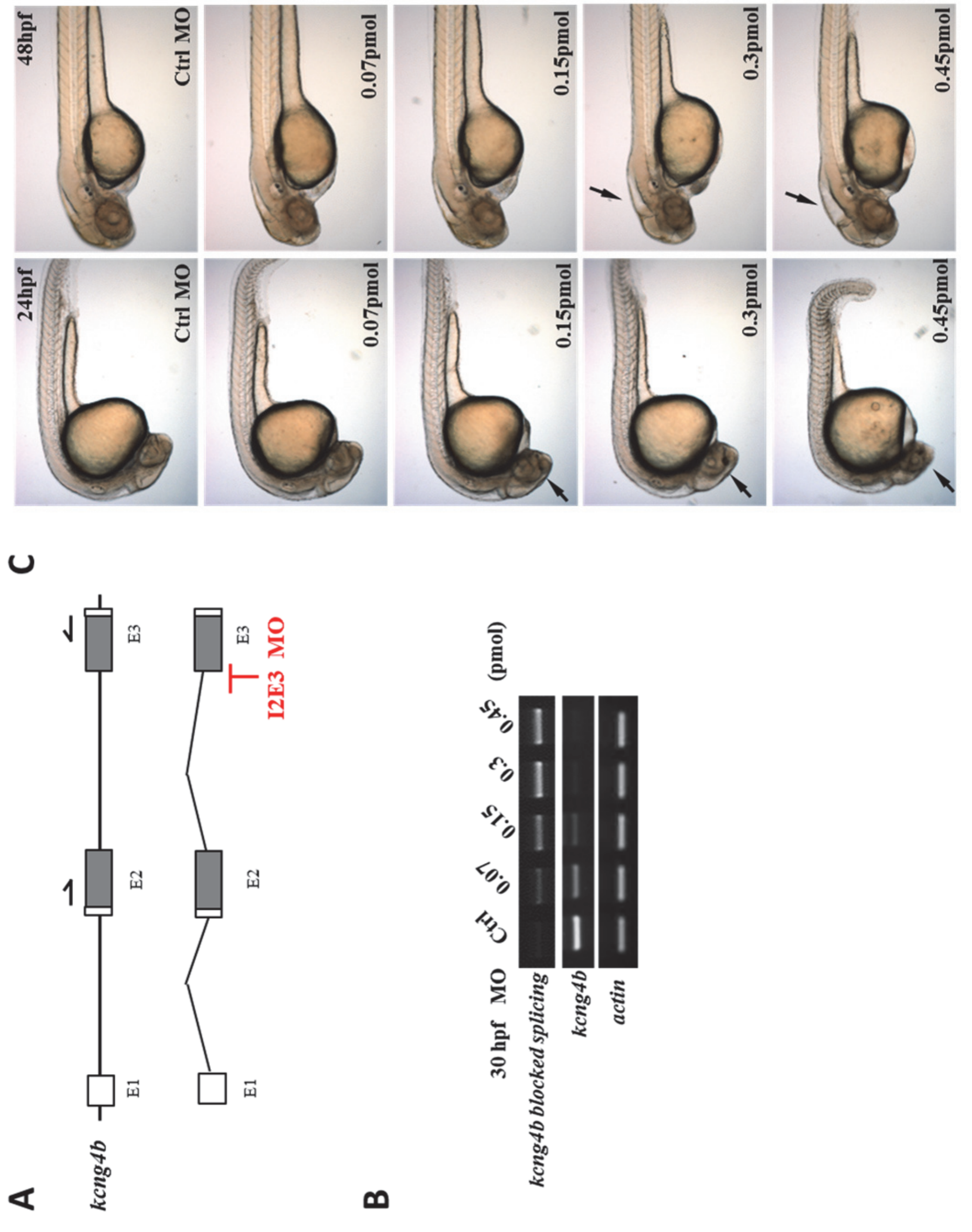
A
kcng4b
E1
E2
E3
I2E3 MO
B
30 hpf MO
Ctrl
0.07
0.15
0.3
0.45
(pmol)
kcng4b blocked splicing
kcng4b
actin
C
24hpf
48hpf
Ctrl MO
0.07pmol
0.15pmol
0.3pmol
0.45pmol

Figure 3.11. Transient loss-of-function of *kcng4b* by morpholino injections recapitulated *kcng4b* mutant phenotype. A. Schematic illustration of *kcng4b* I2E3 MO targeting the splice site of intron 2 and exon 3 of kcng4b. **B**. RT-PCR analyses of full-length *kcng4b* transcripts in morphant embryos. Injection of kcng4b MO resulted in decreased kcng4b transcripts and increased intronic sequence retention in a dose-dependent manner. **C.** *kcng4b* morphants displayed phenotype that mimicked kcng4 mutant embryos in a dose-dependent manner. Arrow: aggregation of delaminated cells from the ventricular zone at 24 hpf and hydrocephalus at 48 hpf.

order to form a functional voltage-gated potassium channel (Kv), four α subunits are needed to form tetramers (Vacher et al., 2008). Like all Kv α subunits, Kv6.4 contains an N-terminal T1 domain, and six transmembrane domains (S1-S6) (Ottschytsch et al., 2002), so it may form heterotetramers with electrically active α subunits such as those encoded by *Kcnb1* (Bocksteins et al., 2009b).

Due to partial genome duplication of bony fish, many genes have two copies, or two paralogues, in zebrafish. Not surprisingly, two paralogues of *kcng4* exist in the zebrafish genome. The insertional mutant isolated in this screen has an insertion in *kcng4b* of Chr.7 (Ensembl Gene ENSDARG00000051892), which encodes a protein of 535 amino acid (aa) residues. The other paralogue, *kcng4a* was found to be located in Chr.18 (Ensembl Gene ENSDARG00000062967) with a protein size of 538 aa residues. Both paralogues have very similar exon/intron structures, with a non-coding exon 1 and two exons 2 and 3 each encoding roughly half of the protein.

3.4.4 Expression of *kcng4a* in sensory cells

To determine whether the two *kcng4* paralogues of zebrafish have conserved domain structure, a multiple sequence alignment was performed between *kcng4* sequences of human, mouse, chicken, frog and zebrafish. It turned out that Kcng4 has a highly conserved domain structure among vertebrates. The two zebrafish paralogue, *kcng4a* and *kcng4b*, has highly conserved T1 domain and S1-S6 domains (Figure 3.12). In addition, the most essential S4 domain working as a voltage sensor and the pore domain for K+ selectivity had 100%

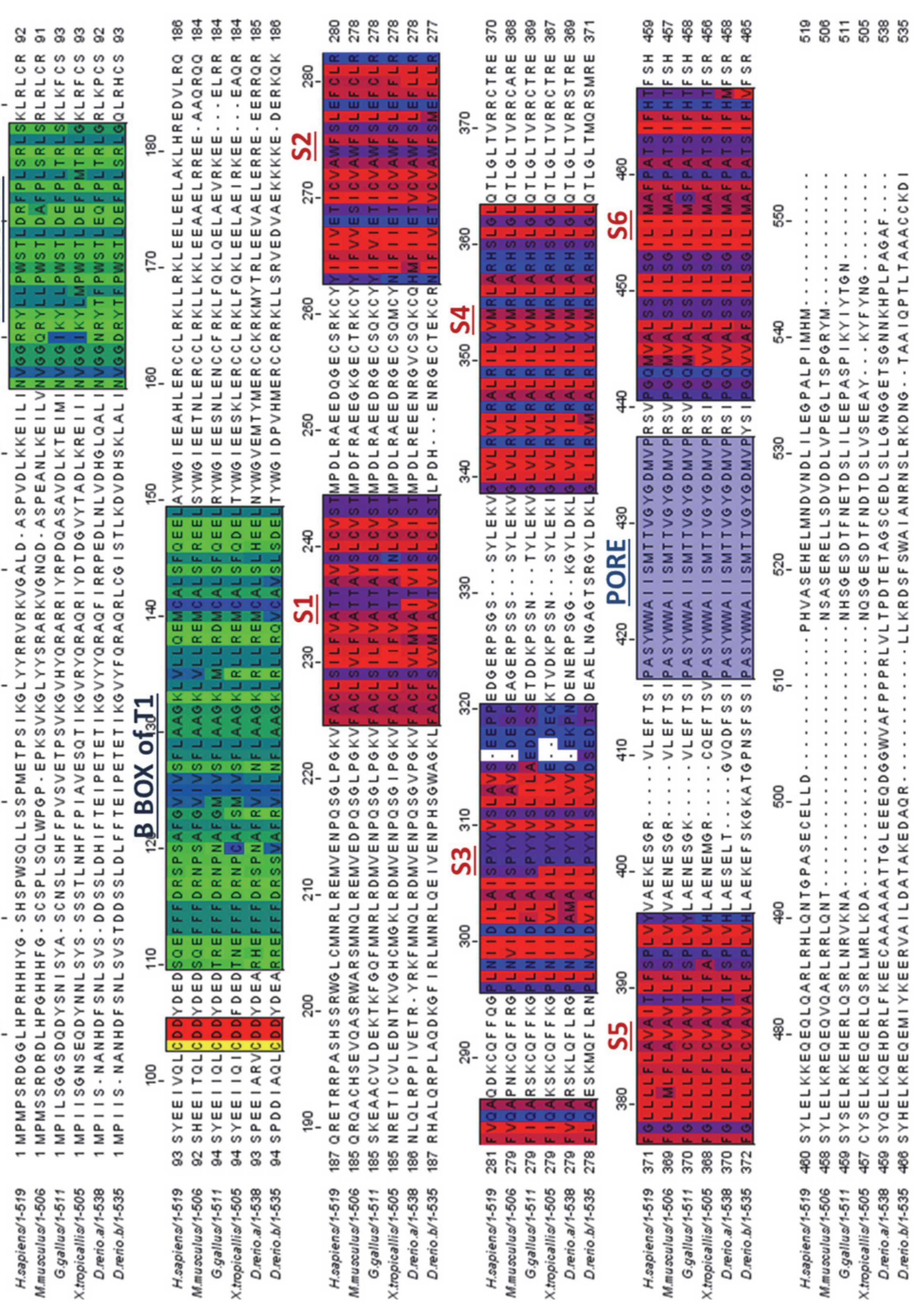
A BOX of T1
B BOX of T1
S1
S2
S3
S4
S5
S6
PORE
H.sapiens/1-519
M.musculus/1-506
G.gallus/1-511
X.tropicalis/1-505
D.rerio.a/1-538
D.rerio.b/1-535

Figure 3.12. Multiple sequence alignment of Kcng4a and Kcng4b with other vertebrate kcng4 and depiction of their domain structure. ClustalW alignment of zebrafish Kcng4a and Kcng4b sequences with human, mouse, chicken, frog Kcng4 sequences. Amino acids corresponding to the T1 domain (containing A box, CCD, and B box), S1-S6 (the six transmembrane domain) and the pore loop were shaded.

identity among all vertebrate sequences aligned here, implying a conserved function of Kv6.4 between zebrafish and other vertebrates.

To differentiate the embryonic specific roles of *kcng4a* and *kcng4b*, both genes were cloned from cDNA of pooled wild type zebrafish embryos, and *in situ* hybridisation was performed to determine their respective expression pattern. Surprisingly, although they share a very similar domain structure, the two paralogues had a very distinct expression pattern during embryonic development.

kcng4a transcripts were detected in the sensory cells of cranial ganglia, including the trigeminal ganglion (TG) (Figure 3.13, B), Rohon-Beard (RB) cells in the spinal cord, and on the lens surface (Figure 3.13, B). Around 30 and 48 hpf, transcripts of *kcng4a* were detected bilaterally at the dorsal part of the spinal cord and also in characteristic positions in the hindbrain typical for RB cells (Figure 3.13, A, C, D). In zebrafish, RB cells are primary sensory neurons present in the embryonic spinal cord during embryonic and early larval stages, which respond to mechanosensory stimulation. A RB neuron has a cell body, two central axons and a peripheral dendrite. One central axon projects rostrally to the hindbrain and another caudally within the spinal cord, whereas the peripheral axon extends dorsolaterally from the spinal cord, runs through segmental myotomes and innervates skin, where free nerve endings are formed (Bernhardt et al., 1990). During ~2-4 dpf, RB cells undergo programmed cell death, which is caused by sodium-current mediated electrical activity (Svoboda et al., 2001). It has been reported that an inhibitor of voltage-gated sodium channel or knockdown of an α subunit of voltage-gated

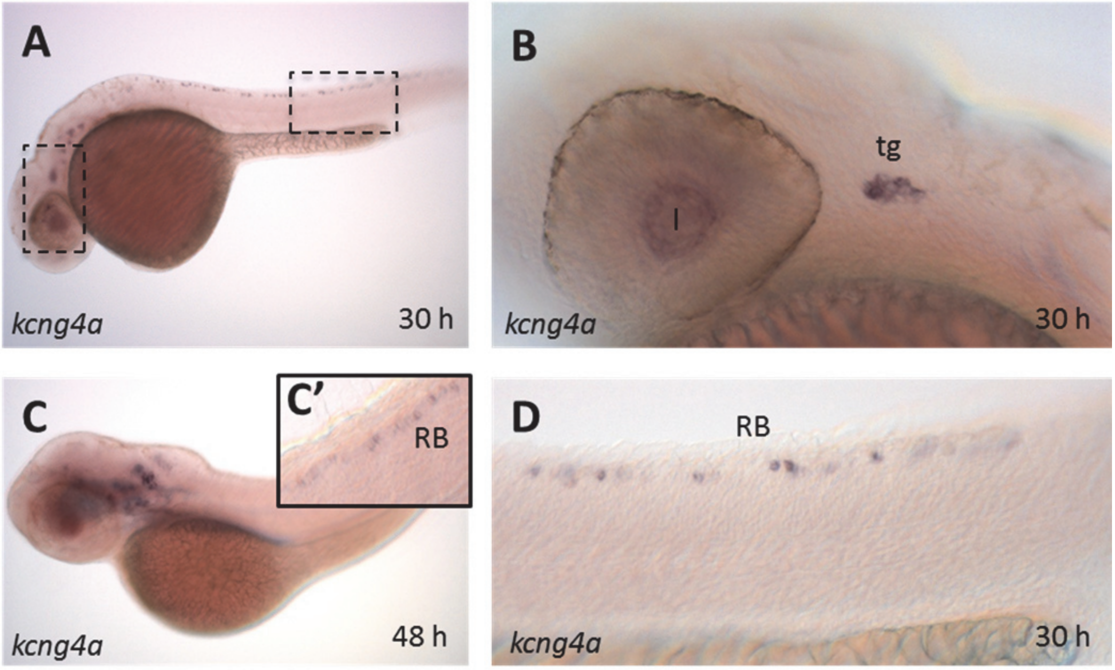

Figure 3.13. Expression of *kcng4a* in sensory cells. *kcng4a* transcripts were detected in the sensory cells of cranial ganglia, including the trigeminal ganglion (tg) and Rohon-Beard (RB) cells in the spinal cord and on the lens surface (l). **A, B, D.** – 30 hpf, **C.** – 48 hpf. The position of B, D (blowups of A) is marked on A by boxes. C'- blowup of the area of spinal cord of embryo shown in C.

sodium channels (Nav1.6a) decreased the RB cell death (Pineda et al., 2006). Recently, it has been reported that knockdown of *atp1a3a*, the α3 subunit of NaKATPase ion pump, caused depolarization of RB neurons in zebrafish, suggesting impaired neuronal excitability. This was further supported by observing altered response to tactile stimuli and reduced mobility in those embryos (Doganli et al., 2013). Thus, it is not difficult to hypothesize that *kcng4a*, encoding the Kv6.4a subunit of Kv channel, might also have similar function in controlling electrical activity in RB neurons. A reverse genetic approach, either by injection of MO against *kcng4a* or generation of targeted *kcng4a* mutant, could be taken to verify *kcng4a* function in future investigations.

3.4.5 Expression of *kcng4b* in the ventricular zone of the embryonic brain

In contrast to *kcng4a*, *kcng4b* transcripts were found to be mainly expressed at 24 hpf in the brain ventricular zone. *In situ* hybridization with an antisense RNA probe showed that *kcng4b* mRNA was expressed in neuroepithelial cells lining the lumen of forebrain, midbrain and hindbrain ventricles as well as the central canal of the spinal cord (Figure 3.14, A, B). These areas together form the ventricular zone of neural tube (Merkle and Alvarez-Buylla, 2006). When embryonic neurogenesis progressed to 30 and 48 hpf, expression of *kcng4b* in the ventricular zone remained and expression in other tissues started to appear. These included the ear vesicles, eye lens and CMZ, some ventral tissues of the brain, and intersegmental vessels (ISV) of the trunk (Figure 3.14, C-G). The expression pattern of *kcng4b* in neuroepithelial cells at the

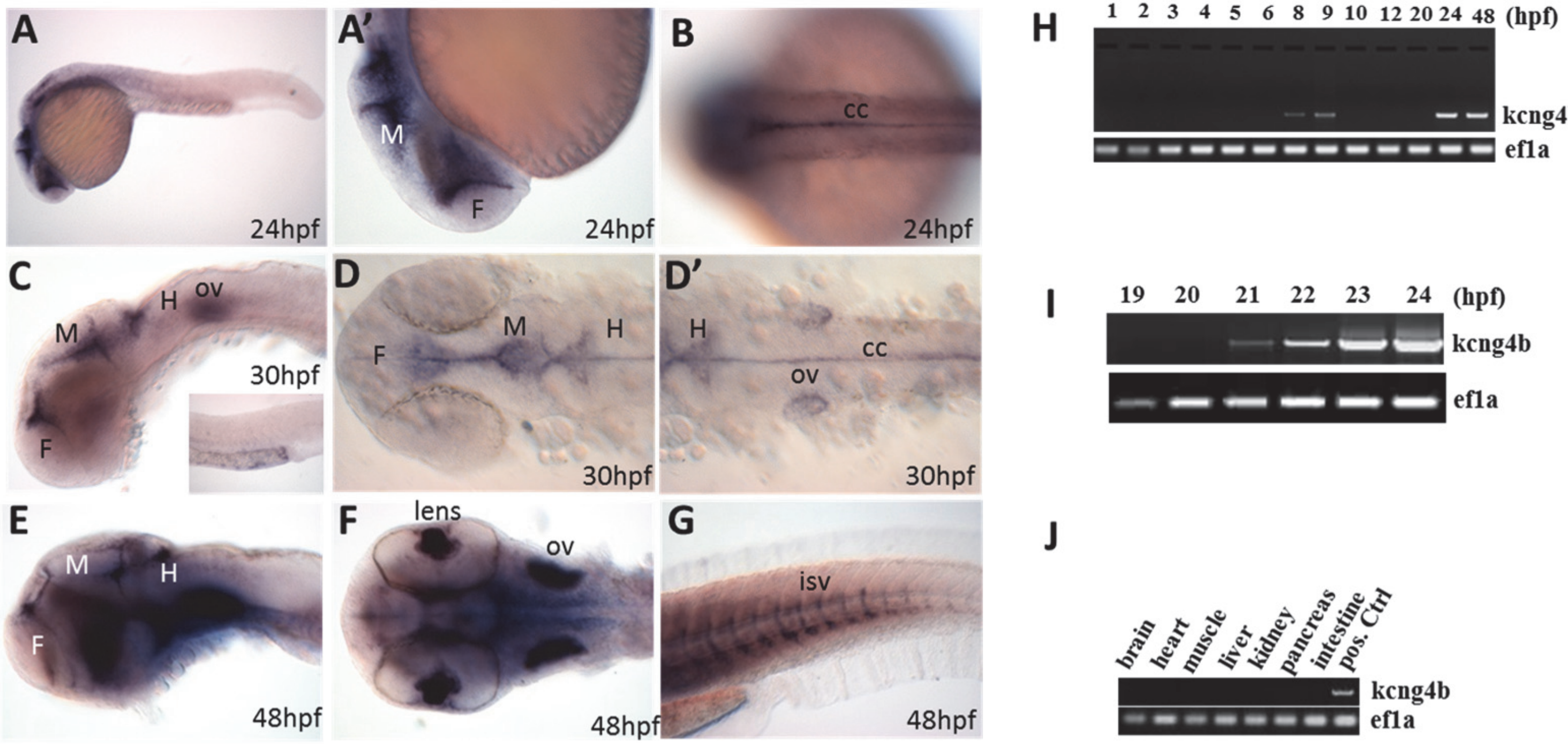

Figure 3.14. Expression of kcng4b in brain ventricular zone and ISV. A-G., Expression pattern of *kcng4b* during development. It was detected in the ventricular zone and intersegmental vessels (ISV). **H.** Developmental expression profile of *kcng4b* as detected by RT-PCR consists of two phases. **I.** Detailed analysis of the second phase of *kcng4b* expression**. J.** *kcng4b* is not expressed in adult tissues examined. F: forebrain, M: midbrain, H: hindbrain, ov: otic vesicle, cc: central canal.

ventricular zone provided an explanation for delamination of cells from the ventricle and hydrocephalus observed in *kcng4b* mutants.

The drastically different expression pattern of *kcng4a* and *kcng4b* implied that during evolution each paralogue adopted its own tissue-specific role. As mammals (mouse and human) have only one *Kcng4*, it remains to be elucidated whether the combined function of both paralogues are conserved during embryogenesis of mice or human.

To further analyze the expression of *kcng4b* during embryonic development, the RT-PCR amplification of full-length *kcng4b* transcripts was performed with a time-course study on RNA isolated from different embryonic stages (Figure 3.14, H). This excluded a maternal role of *kcng4b* as no transcripts could be detected before mid-blastula transition (MBT). Also, no expression was detected throughout blastula, gastrula and early segmentation except that transient expression of *kcng4b* was observed around 8-9 hpf although the specific site of this expression was not identified. An abundant expression was only detected around 24 hpf. Since mutant embryos displayed brain ventricular defects, a more detailed RT-PCR amplification was performed from 19-24 hpf. Transcripts of *kcng4b* started to appear at 21 hpf and were continuously detected later on (Figure 3.14, I). During this period the timing of *kcng4b* expression coincides with the 'window period' when an inflation of embryonic brain ventricle is happening (Lowery and Sive, 2005). This implies a functional role of Kcng4b in regulating development of the brain ventricle. Expression pattern of *kcng4b* in adult tissue was also examined by RT-PCR. However, no expression of this gene was detected in all the adult tissues examined, including brain, heart, muscle, liver, kidney, pancreas and intestine (Figure 3.14, J). Taken together, the tissue-specific pattern of *kcng4b* expression in the ventricular zone and its timing suggested that *kcng4b* functions during early development of brain ventricular system.

3.4.6 *kcng4b* controls inflation of brain ventricles

As knockdown of *kcng4b* caused hydrocephalus, we wonder whether overexpression of this Kv channel subunit would have the opposite effect. Zebrafish embryos injected with *in vitro* synthesized *kcng4b* mRNA at one-cell stage did not display obvious growth delay in terms of overall morphology when compared to stage-matched wild type control embryos (Figure 3.15, A, A'). However, injected embryos displayed absence of brain ventricles from the time that embryonic brain lumen expansion started, i.e. 17 hpf onwards.

To visualize the brain lumen in detail, FITC conjugated BODIPY was used to label extracellular and lumen spaces. The two time points, 21 hpf and 24 hpf, were taken to monitor initial brain inflation and subsequent lumen expansion. When opening of hindbrain ventricle could be clearly observed in wild type control embryos at 21 hpf, embryos injected with *kcng4b* mRNA still display fully sealed neuroepithelia (Figure 3.15, B and C). By 24 hpf, an opened midbrain optocoele lumen and further expanded hindbrain ventricle could be clearly seen in wild type control embryos (Figure 3.15, D). At this stage some more affected embryos injected with *kcng4b* mRNA still displayed completely sealed neuroepithelia (Figure 3.15, E), whereas mildly affected embryos, slightly inflate hindbrain ventricles but midbrain optocoele remains fully sealed (Figure 3.15, F). Interestingly, albeit brain ventricles were absent,

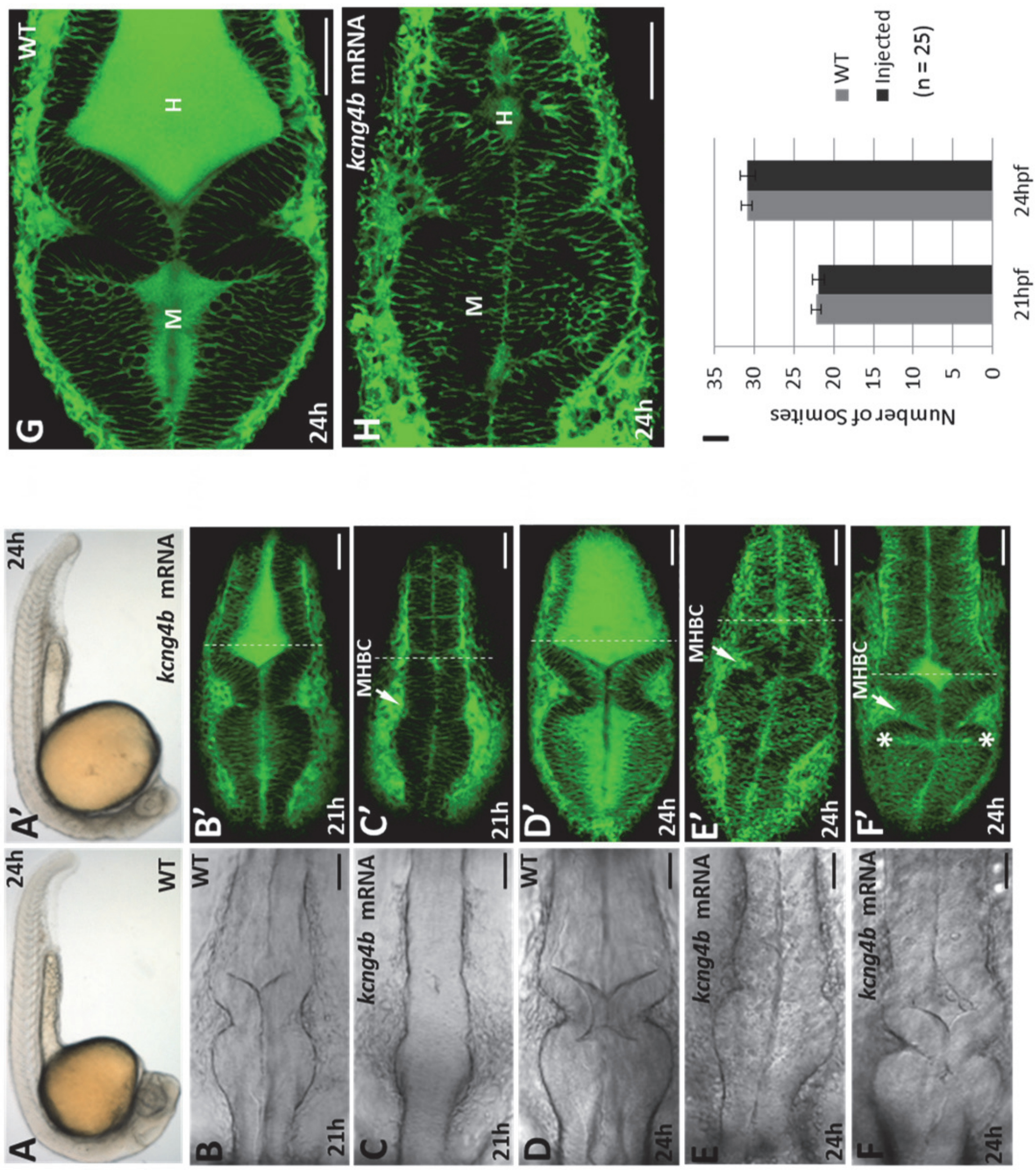
A
24h
WT
A’
24h
kcng4b mRNA
B
WT
21h
B’
21h
C
kcng4b mRNA
21h
C’
MHBC
21h
D
WT
24h
D’
24h
E
kcng4b mRNA
24h
E’
MHBC
24h
F
kcng4b mRNA
24h
F’
MHBC
*
*
24h
G
WT
M
H
24h
H
kcng4b mRNA
M
H
24h
I
Number of Somites
35
30
25
20
15
10
5
0
21hpf
24hpf
WT
Injected
(n = 25)

Figure 3.15. Overexpression of *kcng4b* blocked ventricle formation. A, B. Morphology of embryos under dissecting microscope, lateral view **C-H**, Confocal images of FITC-BODIPY labeled embryos showing midbrain and hindbrain ventricle morphology. **I.** Number of somite counts. A, C, E. wt control; A’, C, E, F. embryos injected by *kcng4b* mRNA. G, H, single confocal scanning images of brain ventricles. MHBC: midbrain-hindbrain boundary constrictions. Asterisks: apical constrictions.

midbrain-hindbrain boundary constriction (MHBC) was present in severely affected embryos. In addition, the apical constriction started to form in mildly affected embryos (Figure 3.15, E and F). This suggested that the early primary patterning of neurogenesis and subsequent shaping of the neuroepithelium were not affected by *kcng4b* mRNA overexpression.

During neurogenesis in mammals, the nucleus of a dividing neuroepithelial cell migrates to the brain ventricular zone prior to mitosis (Merkle and Alvarez-Buylla, 2006). Similarly in zebrafish neuroepithelia, apical migration of nuclei during G2 was demonstrated as a prerequisite for all cell cycle progression (Leung et al., 2011). Gutzman and Sive (2010) observed that in zebrafish neuroepithelium these dividing cells temporarily adopt a rounded cell shape instead of the normal columnar shape of neuroepithelial cells. Under higher magnification, the neuroepithelial cell shape could be visualized with BODIPY labelling. Rounded cells could be found in close proximity to the midbrain and hindbrain lumen in wild type embryos (Figure 3.15, G), particularly abundant in the midbrain where the lumen was about to inflate. In contrast, only a few round-shaped cells were observed in the hindbrain neuroepithelium of *kcng4b* mRNA injected embryo, where a small lumen started to form. This phenomenon was even more manifested in the midbrain (Figure 3.15, H), which could be due to the lack of intraluminal pressure and fluid flow required for neuroepithelia proliferation (Lowery and Sive, 2009).

No significant difference was observed in somite number between wild type embryos and stage-matched embryos injected with *kcng4b* mRNA at the two time points, when ventricular lumen size was assessed (Figure 3.15, I). Also, no obvious differences were observed by other morphological parameters used to stage zebrafish embryos (data not shown). Thus, the underinflated brain ventricle phenotype was not due to general developmental delay. Since *kcng4b* mutant displayed hydrocephalus (i.e. excessive inflation of brain ventricles), whereas overexpression of *kcng4b* mRNA leads to insufficient ventricle inflation, hence *kcng4b* functions to modulate brain ventricle inflation during embryonic neurogenesis.

To test whether the regulatory function of *kcng4b* on brain ventricle inflation could be performed by Kcng4 genes of mammals, C-terminal EGFP-tagged human kcng4 (hkcng4) mRNA was synthesized *in vitro* and injected into one-cell staged zebrafish embryos. Expression of EGFP-tagged hKCNG4 protein could be detected at sphere stage and it seems to be localized to one side. At shield stage and later epiboly stage expression continued relatively uniformly (Figure 3.16, A-D). By 24 hpf, embryos failed to develop brain ventricles (Figure 3.16, E and F), i.e. a phenotype same as the one caused by injection of zebrafish *kcng4b* mRNA. This suggested an evolutionarily conserved function of hKCNG4 in regulating embryonic brain ventricle inflation. Again, the absence of brain ventricle in *hKCNG* mRNA injected embryos was not due to general developmental delay, as staged by the lens diameter (Figure 3.16, E and F). However, the percentage of embryos displaying absence of brain ventricle was much lower compared to the efficiency of zebrafish *kcng4b* (Figure 3.16, G). This could be due to different codon preferences between mammals and teleosts and/or EGFP tag at the C-terminus of the human protein or some functional divergence between human and zebrafish genes.

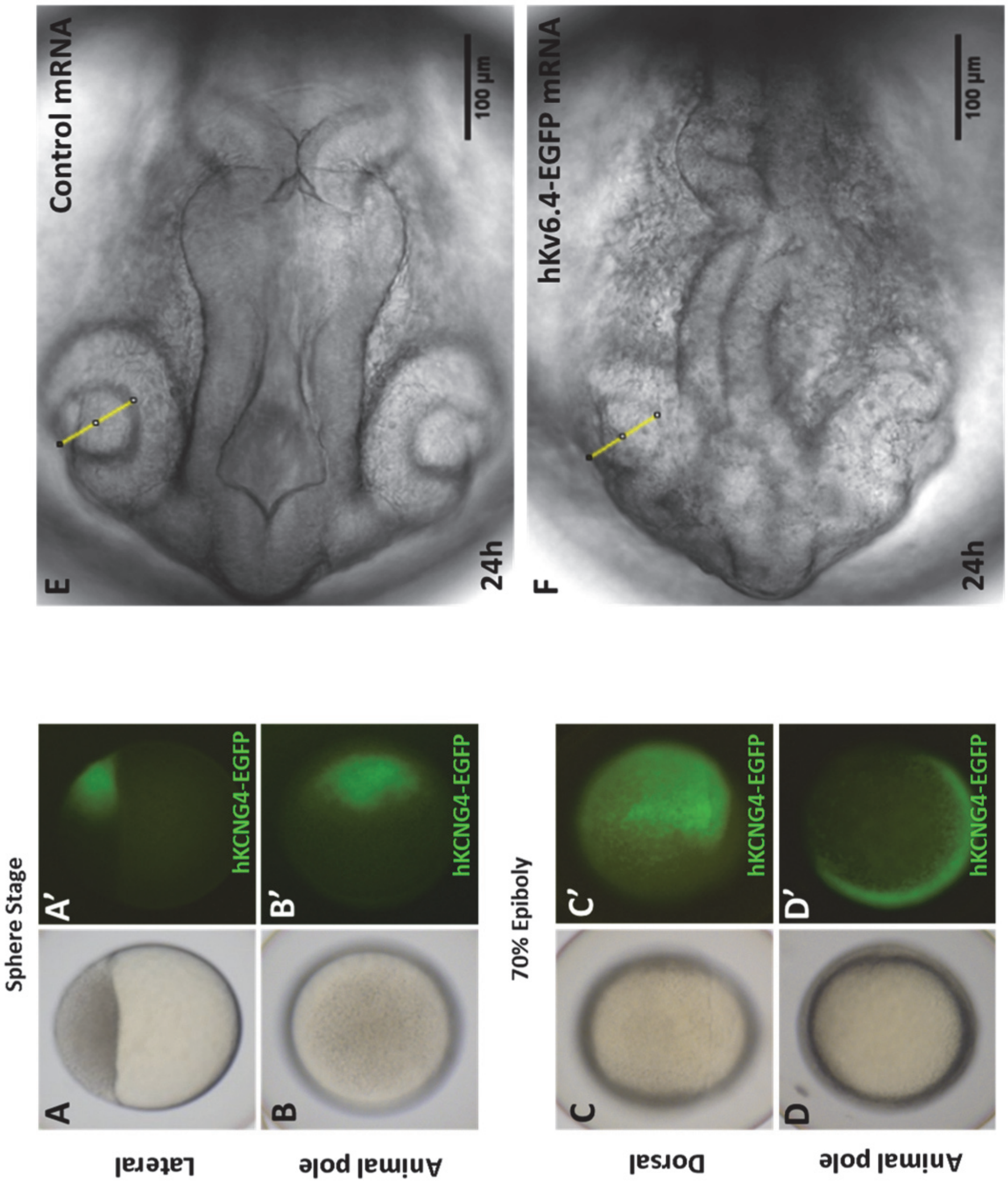
Sphere Stage
Lateral
Animal pole
A
A'
hKCNG4-EGFP
B
B'
hKCNG4-EGFP
70% Epiboly
Dorsal
Animal pole
C
C'
hKCNG4-EGFP
D
D'
hKCNG4-EGFP
E
Control mRNA
24h
100 µm
F
hKv6.4-EGFP mRNA
24h
100 µm

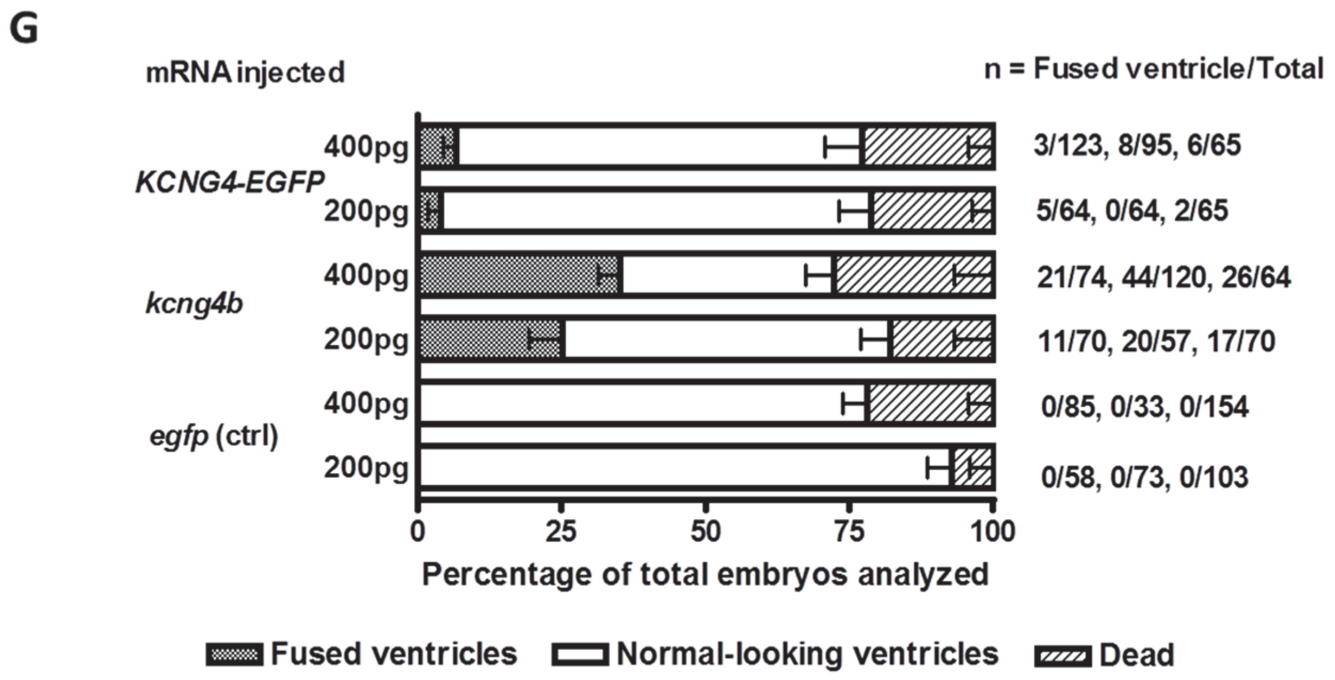

Figure 3.16. Overexpression of hkcng4-EGFP in zebrafish embryos blocked ventricle formation. Injection of hkcng4-EGFP mRNA into zebrafish embryos caused absence of brain ventricles. **A-D.** Detection of human KCNG4-EGFP at sphere and shield stages by fluorescent microscopy. **E, F.** Dorsal view of brain ventricle. **G**. Comparison of number of embryos with absence of brain ventricles by injection of zebrafish *kcng4b* or human *KCNG4-EGFP* mRNA.

3.4.7 Functional antagonism of *kcnb1* and *kcng4b* during ventricle inflation

The failure to inflate the ventricle in embryos injected with *kcng4b* mRNA was very similar to that in the zebrafish *snakehead* mutant. The *snakehead* neural tube undergoes normal ventricle morphogenesis but the ventricles do not inflate. It has been reported that *snakehead* has a mutation in the NaKATPase gene *atp1a1a.1*, and the lack of ventricle might probably be due to impaired ion transport (Lowery and Sive, 2005). This implies that *kcng4b*, encoding a Kv channel silent α subunit, might have a function similar to that of NaKATPase in regulating ion transport into the embryonic ventricle lumen. It is necessary to note that although with all of the hallmarks of a voltage-gated K channel subunit, Kv6.4 subunits did not produce K currents in mammalian cells (Ottschytsch et al., 2002). When expressed alone these subunits were retained in the endoplasmic reticulum. Electrophysiology experiments using patch-clamp assays have demonstrated that Kv6.4, as an electrically silent potassium channel α subunit, must form a heterotetramer with another α subunit, Kv2.1, in order to form functional Kv channels to be present on the plasma membrane (Ottschytsch et al., 2005).

Kv2.1 is encoded by the *kcnb1* gene. To determine whether Kv2.1 is indeed involved in embryonic lumen formation, *kcnb1* was cloned and its expression pattern during embryogenesis was examined by RNA *in situ* hybridization. Expression pattern of *kcnb1* is similar to that of *kcng4b* with transcripts of *kcnb1* mainly found at the brain ventricular zone, i.e. neuroepithelial cells lining the lumen of forebrain, midbrain and hindbrain throughout the three developmental stages examined (Figure 3.17). This is similar to expression

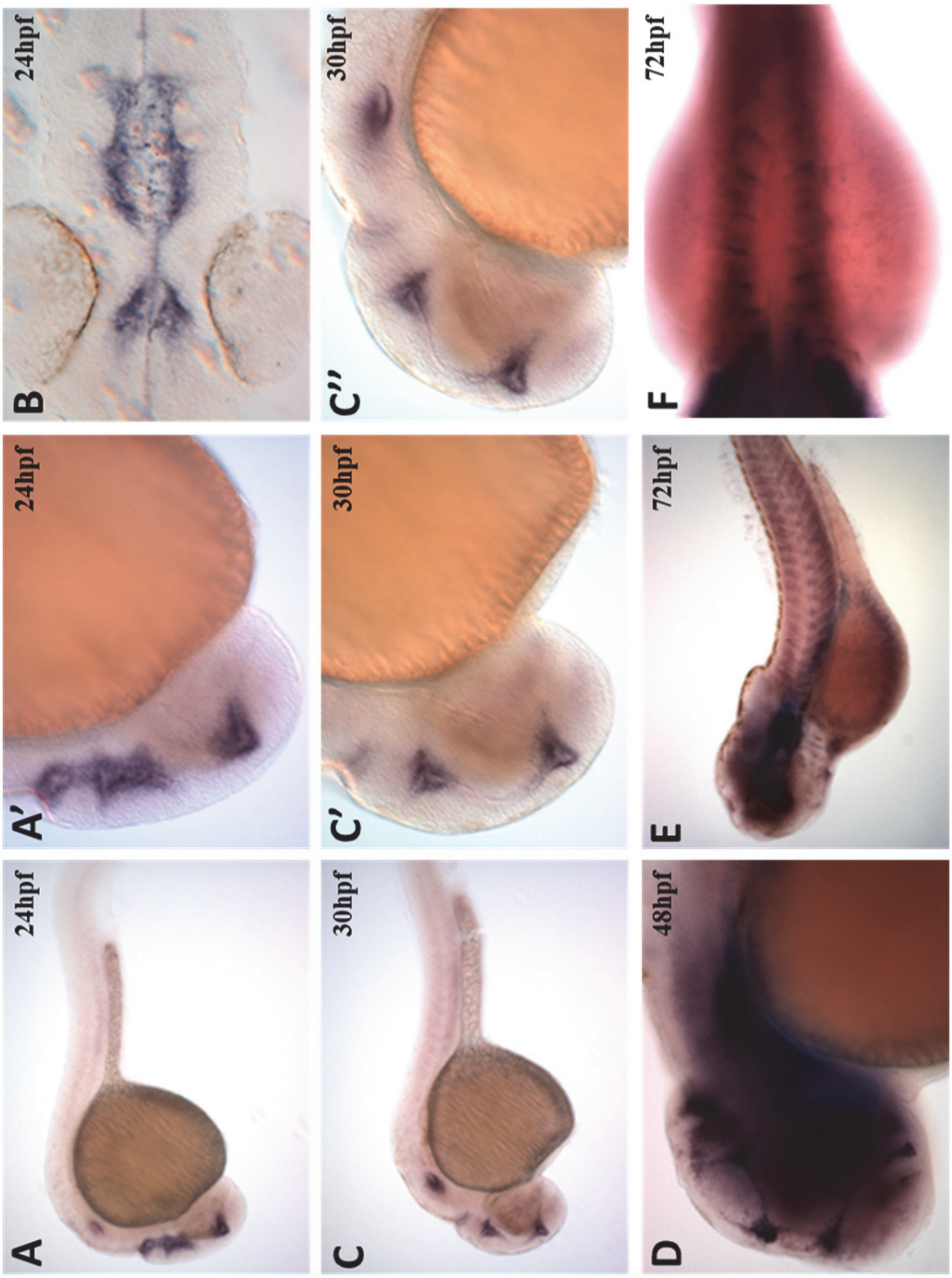
A
24hpf
A'
24hpf
B
24hpf
C
30hpf
C'
30hpf
C''
30hpf
D
48hpf
E
72hpf
F
72hpf

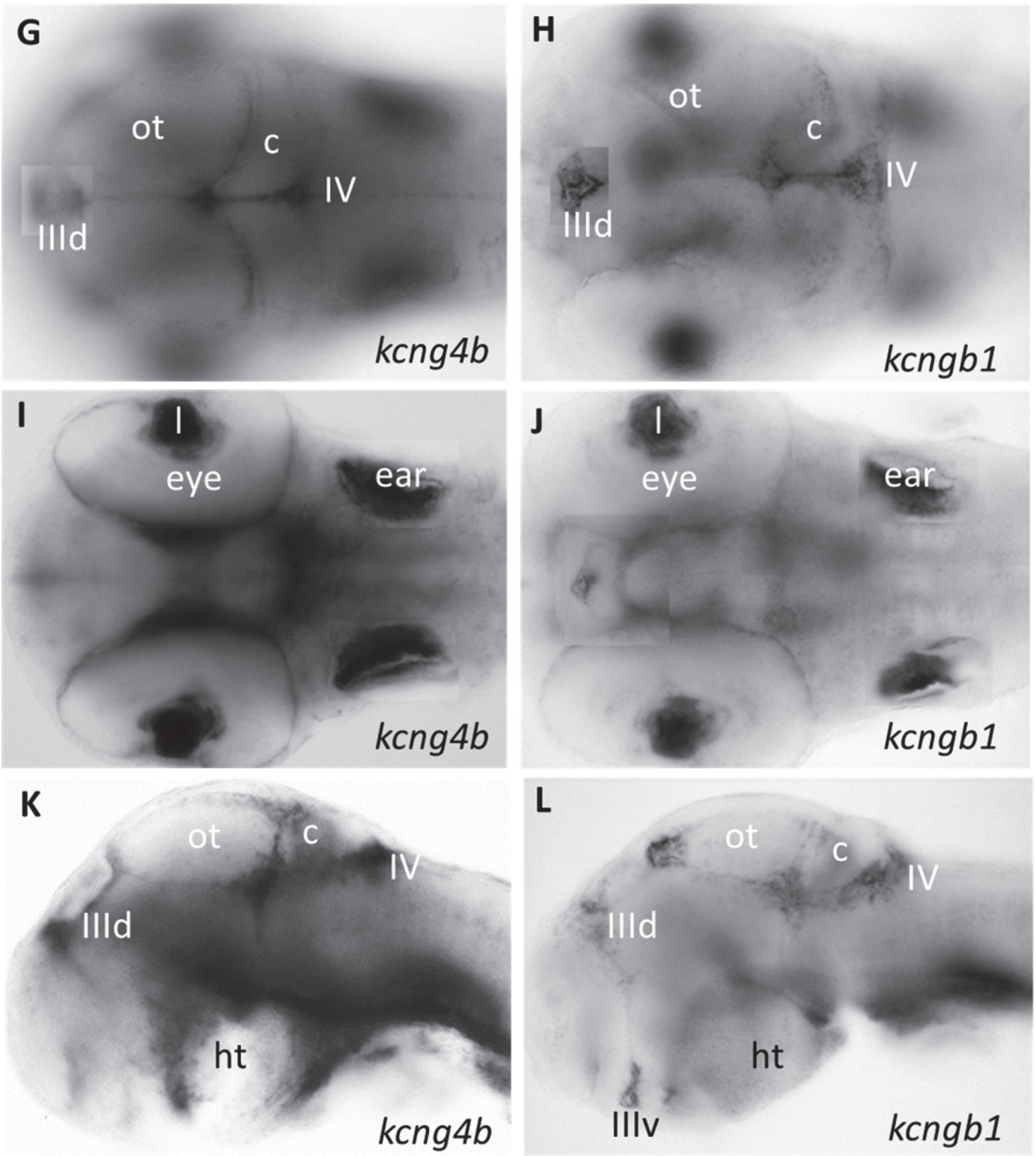

Figure 3.17. Similar expression pattern between *kcnb1* and *kcng4b.* A-G., Expression pattern of *kcnb1* during embryonic development. Transcripts of *kcnb1* were mainly detected in the ventricular zone and at the ear vesicles, lens, ventral part of the brain, intersegmental vessels (ISV) and weakly at somites intersomitic vessels (ISV). **G-L.** Comparison of expression patterns of *kcng4b* and *kcnb1* at 72 hpf. G-J. dorsal view, composite images of two optic planes; G, H. dorsal planes; I, J. ventral planes. K, L. lateral view after removal of eyes. Abbreviation: c. cerebellum, ht. hypothalamus, l. lens, ot. optic tectum, IIId. dorsal III-rd ventricle, IIIv , ventral III-rd ventricle, IV. IV-th ventricle.

pattern of *kcng4b* (Figure 3.14). Also similar to *kcng4b*, transcripts of *kcnb1* were found to be present at the ear vesicles, lens, ventral part of the brain, and weakly at somites. The expression patterns of two genes were also similar at 72 hpf (Figure 3.17, G-L). Given the fact that *kcng4a* displayed drastically different expression in sensory cells, it could be hypothesized that *kcng4b*, not *kcng4a*, is the regulatory subunit controlling *kcnb1* function during ventricle inflation in zebrafish brain.

Kv2.1 belongs to Kv2 subfamily of voltage-gated potassium channels. Kv2.1 is the principle Kv channel underlying the delayed-rectifier (I_{DR}) currents in most mammalian brain neurons. Specifically, I_{DR} currents are important in regulating somatodendritic excitability in hippocampal and cortical pyramidal neurons (Misonou et al., 2005). Kv2.1 was found to be ubiquitously expressed in almost all adult tissues in human (Ottschytsch et al., 2002), whereas the more location specific regulatory subunit, Kv6.4, was thought to diversify the function of Kv2.1 in specific tissues (Bocksteins and Snyders, 2012).

An alignment of multiple *Kcnb1* genes, including zebrafish, human, mouse, chicken and frog revealed high homology among all these genes. In particular, the ~300 amino acid core domains comprising the S1-S6 transmembrane domain and pore loop regions were almost identical (Figure 3.18). As core domains form the major voltage-sensing apparatus (S4) and the ion-selective pore (pore loop), a function of Kv2.1 could be highly conserved among all vertebrates.

To determine the functional role of Kv2.1 during embryogenesis, *in vitro* transcribed *kcnb1* mRNA was injected into one-cell stage zebrafish embryos.

Overexpression of *kcnb1* mRNA phenotypically mimicked the *kcng4b* loss-of-function mutant with cells delaminating from the ventricular zone were found inside the brain lumen (Figure 3.19, A, B) at 24 hpf. This suggested opposing roles of Kv2.1 and Kv6.4 during embryonic brain ventricle development, since increased amount of Kv2.1 led to same effect as a decrease in Kv6.4. Taken together, it could therefore be postulated that the silent subunit, Kv6.4b, functions to regulate Kv2.1 function during lumen formation, probably through formation of Kv6.4b/Kv2.1 heterotetramers that modulate the I_{DR} currents density and membrane potential of Kv2.1 homotetramers.

3.4.8 Inhibitory role of *kcng4b* on neuroepithelial proliferation

BODIPY labelling of brain ventricles revealed a reduction in a number of rounded (dividing) neuroepithelial cells in embryos injected with *kcng4b* mRNA (Figure 3.15, G and H). To confirm that, immunostaning of phospho-histone-3 (PH3) positive mitotic cells were performed on these embryos. PH3 staining demonstrated that dividing neuroepithelial cells were located mainly in the brain ventricular zone in embryos injected with *kcng4b* mRNA similar to wild type controls (Figure 3.20, A). However, the number of mitotic cells was reduced almost by half (Figure 3.20, B). Therefore, overexpression of *kcng4b* mRNA caused a reduction in proliferation of neuroepithelial cells.

To test whether depletion of *kcng4b* function would have the opposite effect, PH3 staining was performed on *kcng4b* mutant embryos at two developmental stages – 24 hpf and 48 hpf. As expected, an excessive cell proliferation was detected in the mutant neuroepithelium. The average number of PH3-positive cells in *kcng4b* mutant neuroepithelium increased around 2.5 folds at 24 hpf

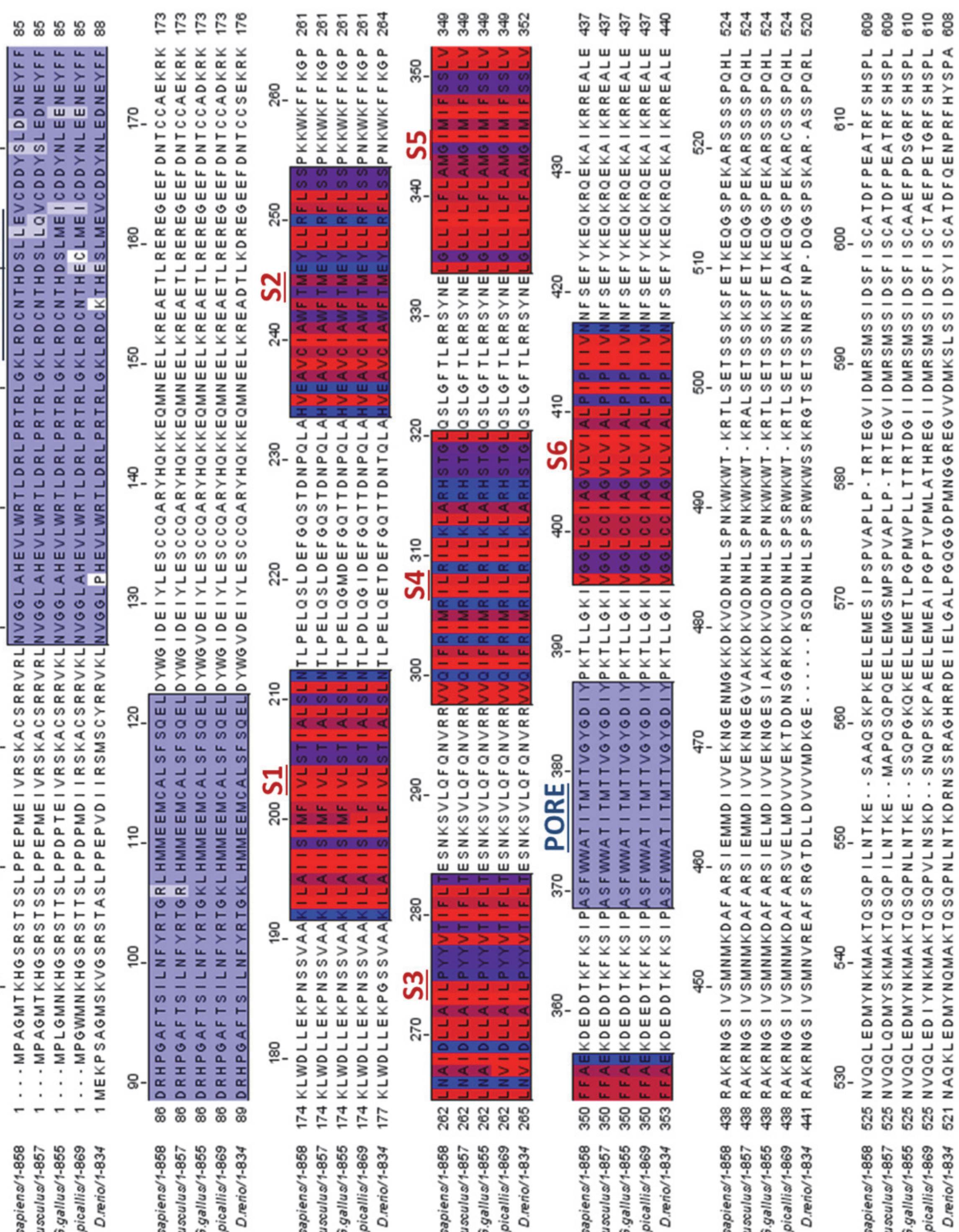
T1 DOMAIN
S1
S2
S3
S4
S5
S6
PORE
H.sapiens/1-858
M.musculus/1-857
G.gallus/1-855
X.tropicallis/1-869
D.rerio/1-834

Figure 3.18. Multiple sequence alignment of zebrafish *kcnb1* with other vertebrate kcnb1 and depiction of their domain structure. ClustalW alignment of zebrafish *kcnb1* sequences with human, mouse, chicken, frog kcnb1 sequences. Amino acids corresponding to the T1 domain, S1-S6 (the six transmembrane domain) and the pore loop were shaded. Only the first ~600 amino acids were shown.

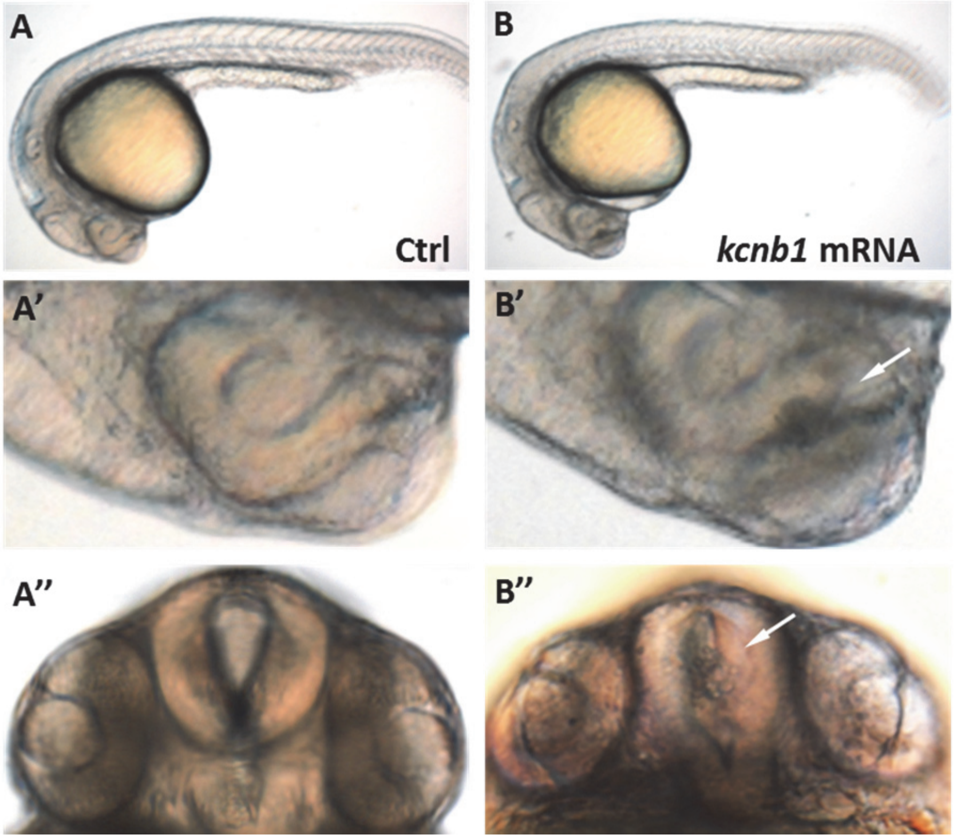

Figure 3.19. Overexpression of *kcnb1* mRNA phenotypically mimicked the *kcng4b* loss-of-function mutant. Embryos injected with *kcnb1* mRNA displayed cells delaminating from the ventricular zone inside the brain lumen (arrowed). **A**. Wild type control embryos at 24 hpf. **B**. *kcnb1* mRNA injected embryos at 24 hpf. A.B. lateral view. A'.B'. lateral view of forbrain (magnified). A''.B''. frontal view.

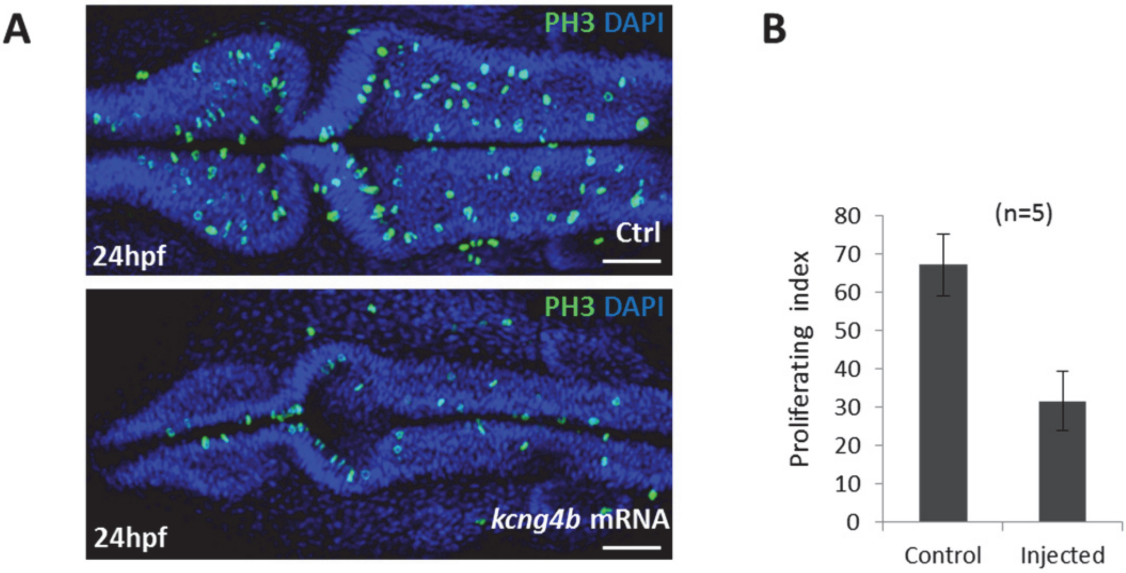

Figure 3.20. Overexpression of *kcng4b* inhibits neuroepithelial cell proliferation. A. Dorsal view of embryos midbrain and hindbrain ventricles stained with anti-phosphohistone H3 antibody (green) and DAPI (blue) to reveal cells in M-phase of cell cycle and cell nuclei. **B**. Comparative analysis of cell in M-phase in control vs. *kcng4*b mRNA injected embryos.

(Figure 3.21, E). As neurogenesis progressed, the number of neuroepithelial cells undergoing mitosis was reduced at 48 hpf in wild type embryos (Figure 3.21, A and C). However, the neuroepithelium of *kcng4b* mutant embryos still demonstrated a hyper-proliferative state at 48 hpf (Figure 3.21, G). Majority of the PH3-positive mitotic cells were still found to be located near the lumen in mutant embryos, indicating that the mechanism driving neural stem cells to migrate to the ventricular zone before cell division (including interkinetic nuclear migration) was probably not affected.

3.4.9 Apical cells in neural epithelia of *kcng4b* mutant embryos were lost

The main phenotype of *kcng4b* mutant was delamination of neuroepithelial cells into the brain ventricular lumen (Figure 3.10, A-D). Neuroepithelial cells facing the ventricle lumen are highly polarized cells with their apical end contacting the eCSF at the ventricular lumen and basal end contacting the basement membrane. To check whether apical/basal polarity was still maintained in the *kcng4b* mutant neuroepithelium, anti-αPKC immunostaining was performed on histology sections of mutant embryos at 24 hpf. Instead of a smooth apical lining αPKC observed in wild type embryo, mutant embryo displayed disrupted apical surface, especially in the forebrain region where in addition some delaminated ventricular cells were observed (Figure 3.22, A and B). At the midbrain and hindbrain region, apical staining of αPKC displayed a dispatched and distorted morphology of the ventricular lining unlike that in control embryos (Figure 22, C-F).

Phalloidin binds to F-actin, another cell surface localized apical marker of neuroepithelium. To further characterize the neuroepithelia at later stages,

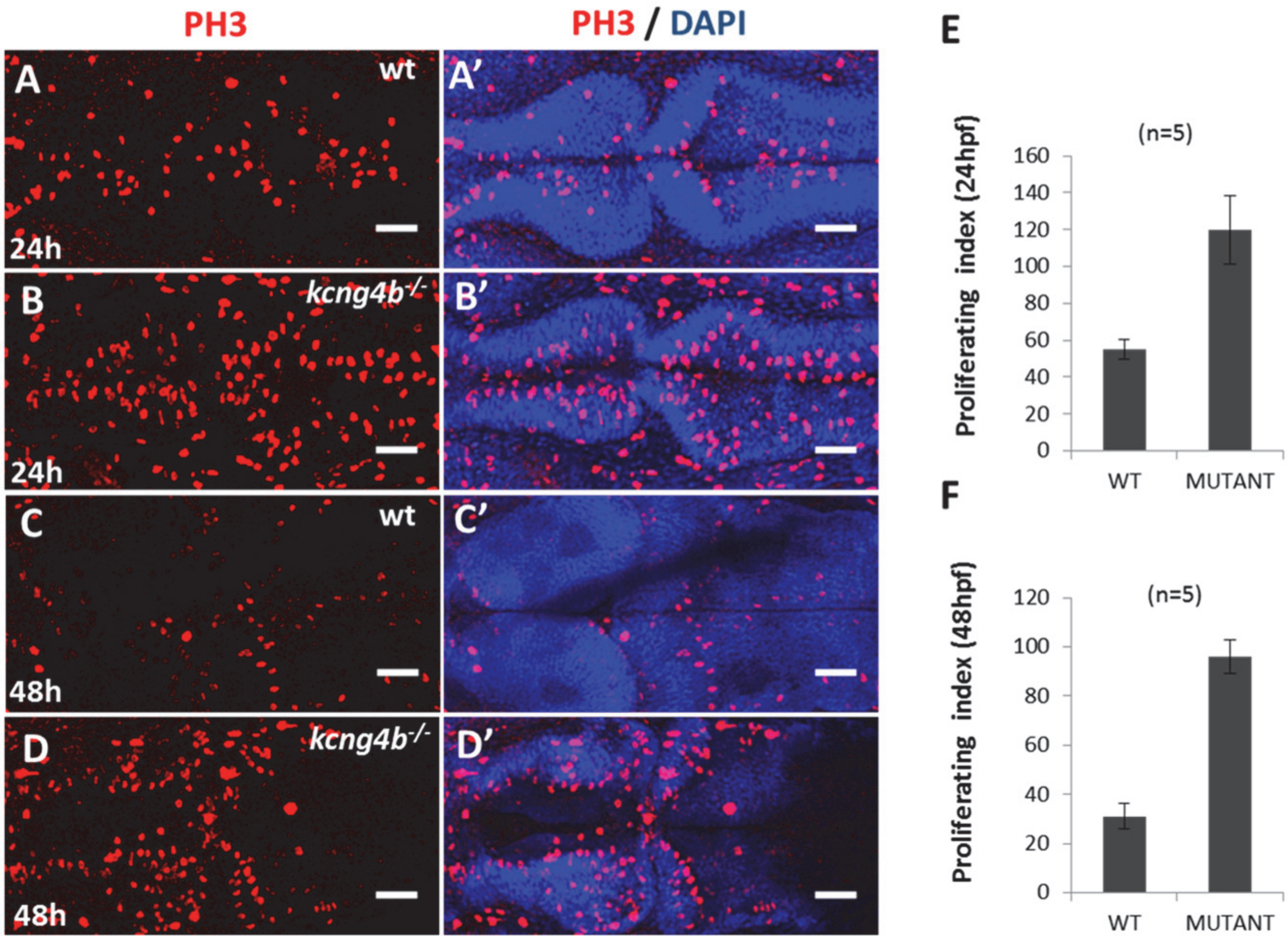

Figure 3.21. Neuroepithelium of *kcng4b* mutants displayed hyper-proliferation. **A-D**. Dorsal view of embryos stained by anti-phosphohistone H3 antibody (red) and DAPI (blue) to reveal cells in M-phase of cell cycle and cell nuclei. A,B. 24 hpf, C,D. 48 hpf; A,C. Controls, B,D. *kcng4b* mutant embryos. **E, F**. proliferative index.

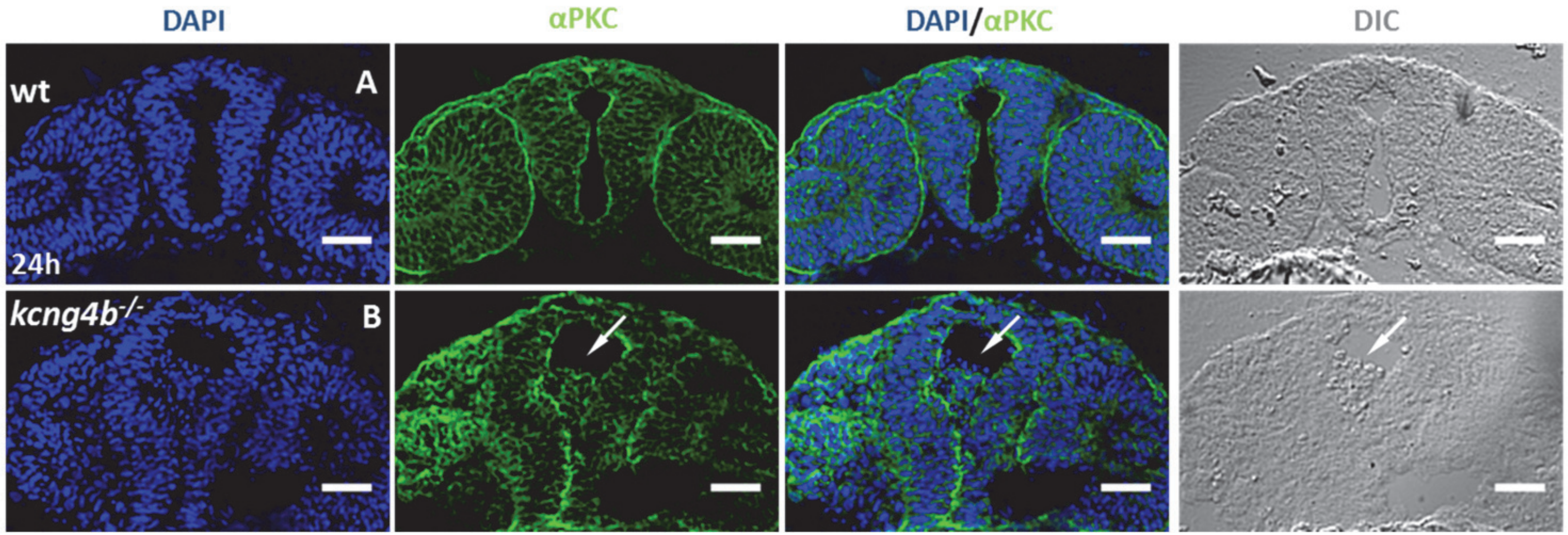

Figure 3.22. Apical/basal polarity is affected in neuroepithelial cells of *kcng4b* mutant embryos at 24 hpf. A, B. forebrain leve (cross section). **C, D.** midbrain (cross section near the eyes) **E, F.** hindbrain (tangential section) A, C, E. controls, B, D, F. *kcng4b* mutant embryos. Arrow: cells in the ventricle with absence of staining. Immunostaining by anti- αPKC, counterstained with DAPI.

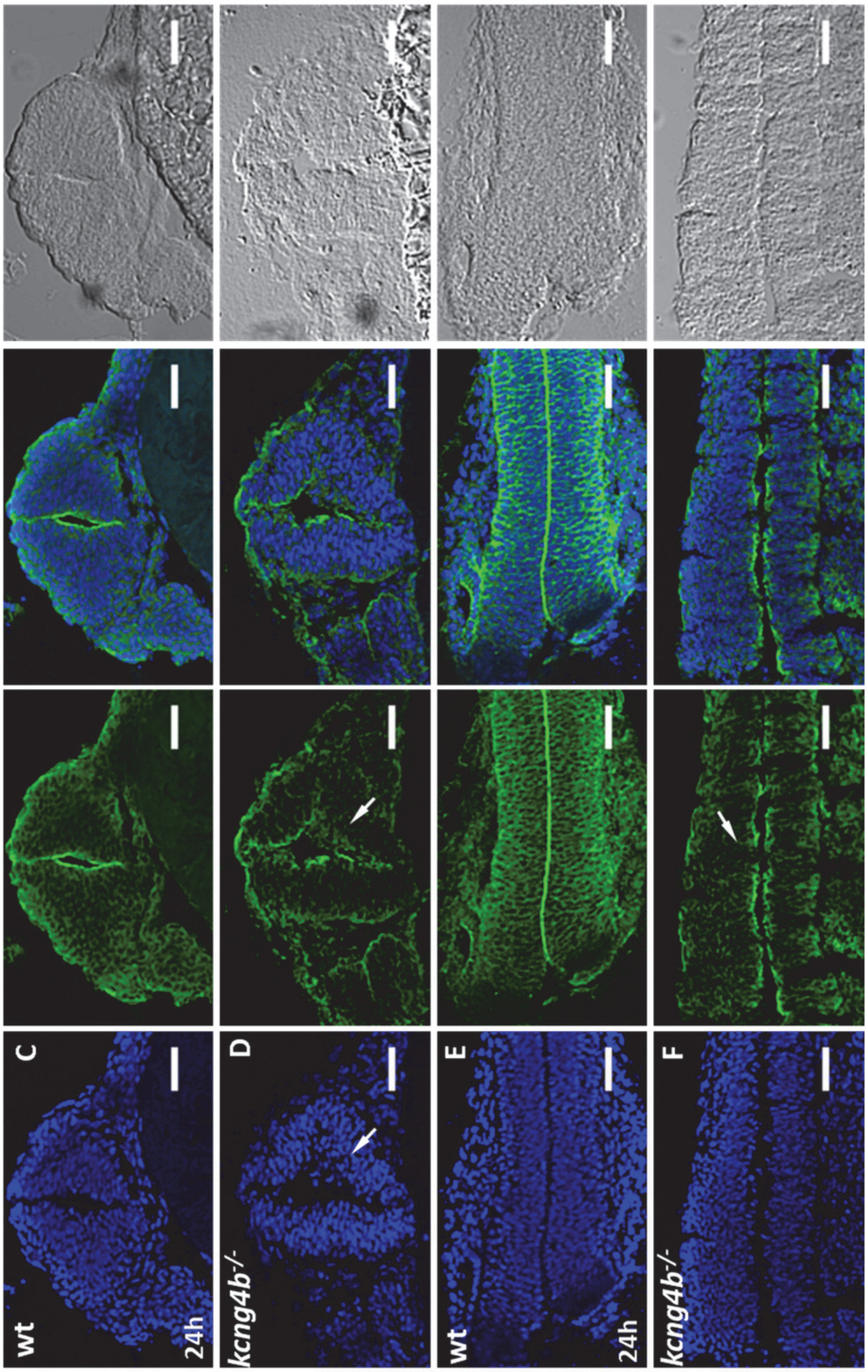
DAPI
αPKC
DAPI/αPKC
DIC
wt
24h
C
kcng4b-/-
D
wt
24h
E
kcng4b-/-
F

phalloidin staining was performed on histology sections of midbrain and hindbrain region at 48 hpf. As neurogenesis progresses further into day two, cell population of the embryonic brain increases dramatically. Ventricular lumen space is much narrowed at 48 hpf. However, in the hydrocephalic *kcng4b* mutant, lumen size was greatly increased. Similar to αPKC staining, phalloidin staining displayed a smooth apical surface lining the ventricular lumen surface of diencephalon, mesencephalon and hindbrain at 48 hpf in wild type control embryos (Figure 23, A and C). Phalloidin staining displayed a punctuate, distorted, discontinuous line in the neuroepithelia lining the ventricular surface of *kcng4b* mutant embryo. Albeit increases of mitosis, the amount of neuronal tissues was smaller than that in wild type controls (Figure 23, B and D). In addition, delaminated cells were observed in the ventricular lumen (Figure 23 B''). Thus, localization of apical proteins was distorted in the neuroepithelial cells facing the brain ventricles of *kcng4b* mutant in indication that cell polarity was affected. Previously, polarization of cell membrane was suggested to play a role in water transport thereby mediating the flow of water between glial cells and the cavities filled with CSF and the intravascular space and several proteins, including but not limited to N- and E-cadherins, Numb and Numb-like, p120-catenin, N-CAM and Stabilin2 are involved in regulation of cell adhesion and polarity in these processes (Nielsen et al., 1997; Vajda et al., 2004). In addition, the clearance of K+ from areas of high neuronal activity is associated with a concomitant water flux (Badaut et al., 2002). Thus, the modulation of Kv2.1 activity by Kv6.4 may play a role in regulation of cell polarity, which abnormality may affect ventricle inflation.

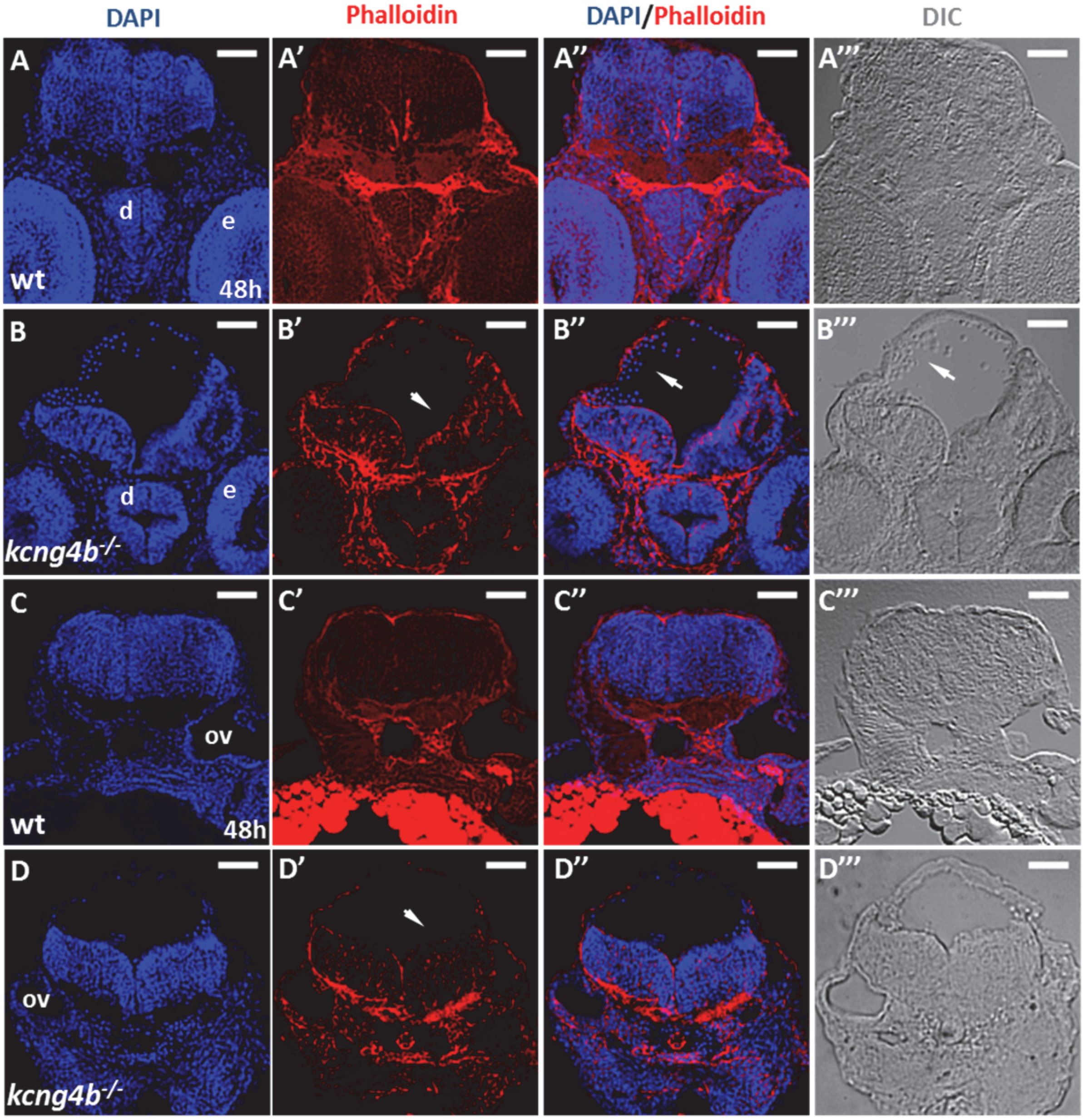

Figure 3.23. Apical/basal polarity is affected in neuroepithelial cells of *kcng4b* mutant embryos at 48 hpf. A, B. midbrain (cross section near the eyes). **C, D .** hindbrain (cross section around otic vesicles) A, C. controls, B, D. *kcng4b* mutant embryos. Immunostaining by phalloidin (Red), counterstained with DAPI.

3.4.10 Angiogenesis of ISV vessels displayed defects in *kcng4b* mutant embryos

Apart from its prominent expression in the ventricular zone of early embryonic brain, *kcng4b* was also expressed in the intersegmental vessels (ISV) of 48 hpf zebrafish embryos (Figure 3.14, G). However, no expression was detected in the major axial blood vessels, the dorsal aorta (DA) and peripheral cardinal vein (PCV). A similar expression pattern was observed for *kcnb1* at ISVs (Figure 3.17, F), but an expression domain of *kcnb1* was broader than that of *kcng4b*, including somites (Figure 3.17, E). Beginning at approximately 20 hpf, ISV sprout bilaterally from the DA. The sprout then migrates towards the dorsal-lateral aspect of the neural tube, where the leading cell branches anteriorly and posteriorly to form the dorsal longitudinal anastomotic vessels (DLAV) (Childs et al., 2002). The expression pattern in these tissues suggested a functional role of Kv6.4b during ISVs development.

To confirm this, an alkaline phosphatase (AP) staining of blood vessels was performed. In wild type control embryos, ISVs could be found along somite boundaries (Figure 3.24, A). In contrast, in mutant embryos a reduced number of primary ISVs was observed. Mutant embryos also displayed extremely thin ISVs probably due to lack of lumen space within the ISVs (Figure 24, B). Similar defects of the ISVs network was observed in *kcng4b* morphant embryos, where gaps or shorter ISVs were observed (Figure 24, C).

To look at the ISVs in more detail, *kcng4b* morphants were generated in a Tg (Fli: EGFP) and Tg (Gata1: DsRed) double transgenic background, so that both blood vessels and circulating red blood cells (RBCs) could be visualized.

Consistent with AP staining results, confocal imaging of the morphant embryos demonstrated shorter and disorganized ISV vessels (Figure 3.24, D and E). Morphant ISV sprouting was either incomplete, with only the dorsally located tip cell present, or the leading cell failed reaching the dorsal branching point, preventing the formation of DLAV. Importantly, unlike the healthy lumenized ISVs observed in control embryos, the majority of the ISVs in *kcng4b* morphants were thin and lacking blood flow, evidenced by the lack of circulating RBCs in these vessels (Figure 3.24, E). However, general morphology and blood flow of major axial blood vessels including DA and PCV were not affected in *kcng4b* depleted embryos, indicating an ISV specific role of *kcng4b* during embryonic vessel development.

Previous studies have demonstrated that K+ current was modulated by cellular redox potential in pulmonary and ear artery smooth muscle cells of the rabbit (Park et al., 1997). Moreno-Dominguez et al. (2009) have shown that the silent channel Kv6.3 regulates smooth muscle cell excitability by regulating Kv2 currents. Taking into account the similar expression patterns of *kcng4b* and *kcnb1* in the ISV, it could be hypothesized that Kv6.4b might have a function in regulating ISV sprouting and angiogenesis similar to that in brain ventricles, i.e. in formation of a lumen. Thus, an antagonism between Kv6.4 and Kv2.1 could be a common feature of lumen formation in development of brain ventricles and angiogenesis.

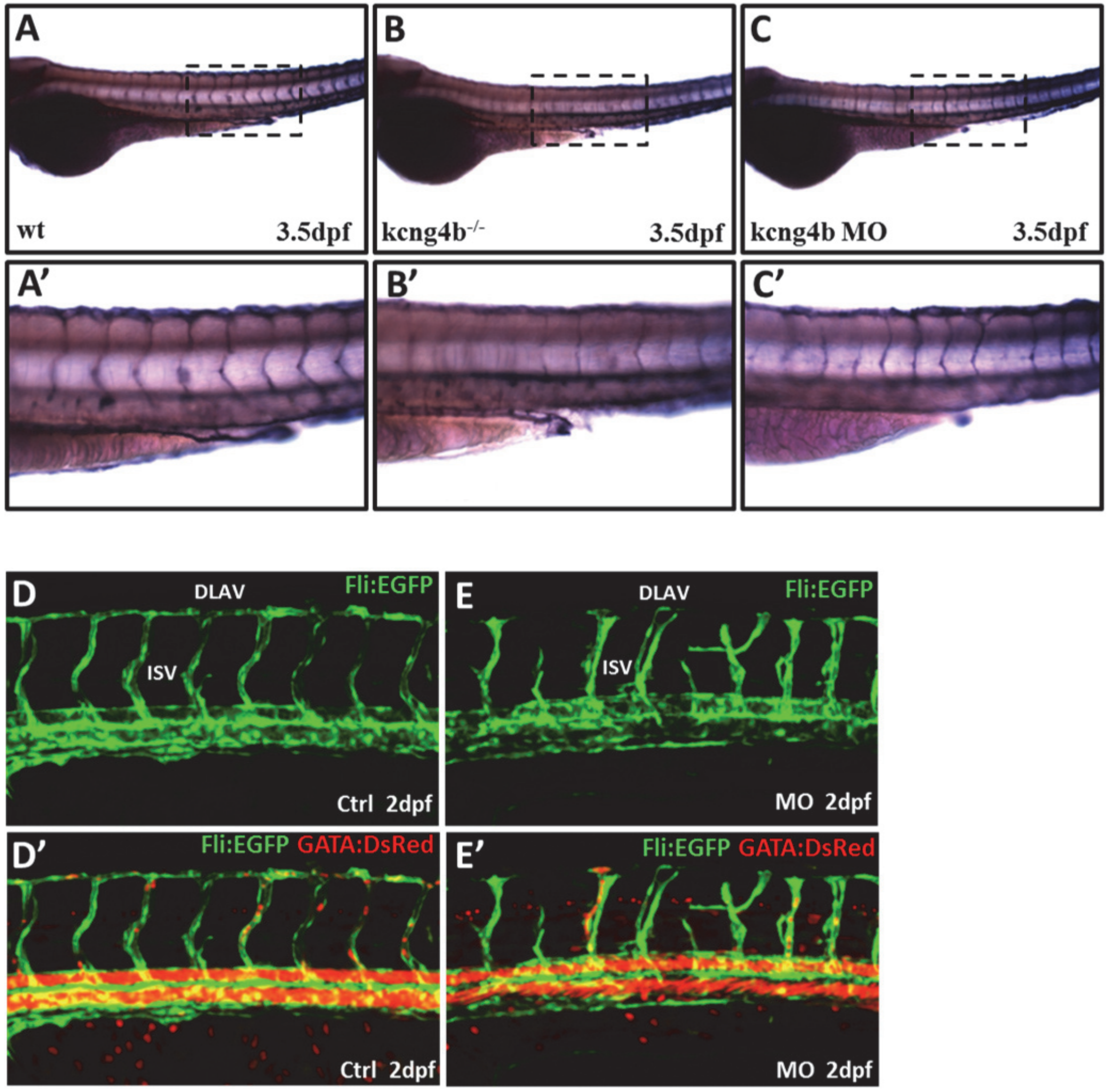

Figure 3.24. Angiogenesis defects in ISV of *kcng4b* mutant embryos. A-C. Alkaline phosphatase (AP) staining of blood vessels. A. Control. B. *kcng4b* mutant. C. *kcng4b* morphant embryo. A’-C’. blowups of box area. **D, E .** Confocal images of ISV vessels and red blood cell (RBC) at Tg (Fli: EGFP) and Tg (Gata1: DsRed) double transgenic background.

Chapter 4. Discussion

4.1 Efficiency of *Tol2*-mediated GBT insertional mutagenesis screen

In this study, a forward genetic screen using *Tol2* transposon-mediated insertional mutagenesis strategy, first described by Sivasubbu et al. (2006), was performed to search for novel genes that regulate embryonic brain circulation. We observed that 16% of embryos (n = 697/4347) display mosaic GFP expression suggesting successful integration of the GBT cassette into their genome. When these potential mosaic embryos grew into adults, 61 founder fish have been identified from screening of 350 adult fish (Table 1). This gives a transgenesis rate of 17% (n = 61/350), which is slightly higher than the 8% transgenesis rate (n = 15/171) previously reported (Sivasubbu et al., 2006). Due to the mosaic nature of the founder fish germline, we estimate the presence of 1.49 insertion sites per F_1 fish (n = 130/87). In individual founders the number of insertion sites varies from 1 to a maximum of 5. We find the efficiency of transposon integration falls into a similar range of Tol2-transposon-based screens reported previously (Nagayoshi et al., 2008; Parinov et al., 2004; Sivasubbu et al., 2006). Thus, we conclude that *Tol2*-mediated GBT integrates efficiently into zebrafish genome.

We find that 54% (n = 71/130) of insertion sites are located within transcribed regions, roughly in the same range (35% - 43%) of previous *Tol2*-based screens (Nagayoshi et al., 2008; Parinov et al., 2004). 32 insertions are located in introns with GBT cassette in the same orientation as the direction of the respective gene. Strictly speaking, only insertions with the correct *cis*-orientation cause effective disruption of the gene function according to the 'splice-in splice-out' working mechanism based on which the cassette was designed, although prior experience of the pseudoretroviral screen (the Hopkins insertional library) suggests that insertion of any foreign sequences into intron, especially the first intron, could greatly reduce the tagged gene expression (Sivasubbu et al., 2007). In addition, we also find insertions in exons of four genes, directly disrupting the coding sequences. Considering the screen was performed by only one person, the GBT insertional mutagenesis is rather efficient.

4.2 GBT cassette modifications for improved efficiency and functionality

The last few years have seen great improvement of *Tol2*-insertional cassette that increases both the efficiency and functionality. Efficiency of an insertional mutagenesis cassette not only relies on the efficient integration into the transcribed region but also an ability to disrupt the gene function. In the case of GBT, this solely depends on the poly (A) terminator sequences used. We observe, in the case of *kcng4b* mutant, great reduction of presence of full-length wild type sequences in homozygous mutants. However, traces of wild type transcripts are still detectable (Figure 3.9, C). This observation is in accordance with previous reports that GBT generally causes a 96%-98% knockdown effect (Sivasubbu et al., 2006). Although this is usually sufficient for analysing a loss of function phenotype, presence of traces of wild type transcripts might lead to a generally weak allele. To circumvent this, Clark et al. (2011) came up with a new GBT cassette, named RP2. They replaced the original poly (A) terminator with a strong poly (A) terminator signal together with border elements of the ocean pout antifreeze gene. This strong terminator increases the terminating efficiency to such extent that nearly all tested lines display a 99% knockdown of native transcripts.

In addition, loxP sites have been added to sequences flanking the GBT cassette, so that when Cre recombinase is introduced *in trans*, either by crossing with Cre recombinase-expressing transgenic lines or simply injection of Cre mRNA, mutant phenotype could be easily rescued (Petzold et al., 2009). This addition allows a quick confirmation on the specificity of mutant phenotype, without a need of mRNA injection rescue traditionally performed that can only rescue early developmental defects, not to mention the tedious titration and adverse effects.

The GBT cassette used in this study contains the β-actin promoter driving the ubiquitous expression of GFP that allows identification of GBT insertion regardless of the expression status of the tagged gene. However, no information on the expression pattern of the tagged gene could be obtained. The traditional protein trap cassette, harbouring a splice acceptor (SA) and an AUG-less fluorescent protein could efficiently mark the expression domain of tagged gene, if the AUG-less fluorescent protein is fused in-frame with gene (Asakawa et al., 2008; Sivasubbu et al., 2007). Therefore, the GBT-RP2 cassette has been designed by adding an AUG-less monomeric RFP after the SA sequences such that the expression domain of the tagged gene will be marked by RPF, if the fusion of RFP is in frame with upstream exon sequences (Clark et al., 2011). An advantage of this approach is obvious. An expression pattern could be easily monitored by RFP fluorescence at different developmental stages *in vivo*, a feature suitable for high-throughput screen.

Such additional feature diversifies the function of RP2 cassette into both expression and mutagenic studies. There are some drawbacks inevitably. For instance, theoretically only 1/3 of fish will have expression domain marked by RFP due to the requirement of an in-frame fusion. In addition, about a quarter of the 350 RP2 insertional lines have RFP expression in the kidney tubules, white blood cells or developing bone regardless of the native expression pattern of the tagged gene, possibly due to retention of RFP in these organs (Clark et al., 2011). Another disadvantage is that RFP expression, either specific or nonspecific, might interfere with fluorescence-based analysis when the mutant allele is transferred into other transgenic background (enhancer lines or reporter lines) for further analysis.

4.3 A few thoughts on improving the screen strategy

The *Tol2* transposon mediates efficient cargo integration. The by-product of this is multiple copies of insertion in a single fish genome. Usually, this could be easily segregated, for example, two insertions could be segregated into single insertions by crossing with wild type fish. However, this defers the analysis for additional three months (for zebrafish to grow from embryos to fertile adults), not to mention about additional effort required for genotyping fish in order to confirm identity of individual carriers. Those founders with three, four or even five insertions where multiple out-crosses are required and some insertions will be lost during this process due to a lack of manpower, fish mishandling, death or difficulties in genotyping. In fact, fish lines with three insertions or more were not analysed in this study solely for these reasons. Some of them were subsequently lost. As genetic screens are costly and labour-intensity, such loss results in tremendous waste of effort.

To prevent this, we support the idea that sperm cryoprotection, a protocol that has been established and improved recently (Carmichael et al., 2009), which should be performed for all male F_0 founder fish in order to preserve all possible insertion sites. By doing this, multiple insertions could be preserved ‘indefinitely’ and could be recovered whenever wanted. Desired insertion sites could be subsequently sorted out by out-crosses. Another advantage of this method is that all insertion sites could be mapped in one-go using the sperm DNA, instead of sampling of F_1 fish to determine the insertion sites. Due to the mosaic nature of F_0 germline, insertion sites mapped by sampling of F_1 fish could not represent all possible insertions in the founder germline. In fact, based on the mechanism of chromosome segregation, F_1 fish from the same founder usually share some of the same insertion sites (Appendix, Table 1). Mapping individual F_1 fish is not cost effective due to duplication efforts involved. Therefore, insertion site mapping based on founder sperm offers improved efficiency and allows sperm preservation at the same time as it prevents the loss of precious insertions.

Mapping of the insertion sites is a tedious and labour-intensive process. Most of the *Tol2*-mediated insertional screens use TAIL-PCR and/or inverse PCR (iPCR) to amplify flanking sequences of insertion sites, followed by BLAST alignment with zebrafish genome reference sequences to map individual insertion sites manually (Kondrychyn et al., 2009; Parinov et al., 2004; Sivasubbu et al., 2006). Here, TAIL-PCR was employed to map all the insertion sites in our screen. However, due to the limitation of using degenerate primers not all flanking sequences are amplified. Therefore, not all insertions are detected. The unmapped insertions are subsequently lost during outcrosses as only known insertions are pursued in the genotyping with specific primer pairs. Unfortunately, insertions mapped by TAIL-PCR only constitute a portion of all insertions that actually exist as demonstrated by whole genome sequencing using next generation sequencing (NGS) methods (Dr. Karuna Sampath, *Ac/Ds* transposon-mediated insertional screen, unpublished). As a cost of whole genome sequencing has become much more affordable recently and taking into account the cost of manpower and reagents used in manual mapping, whole genome sequences using NGS method is highly recommended for future screens, especially large scale insertional screens involving multiple insertion sites.

Ever since the first two reports (Doyon et al., 2008; Meng et al., 2008) demonstrating that zinc finger nuclease (ZFN) can cause heritable gene mutation in zebrafish through repair of double stranded DNA break (DSB) by non-homologous end joining (NHEJ) and homology directed repair (HDR), the last five years have seen tremendous breakthrough in zebrafish reverse genetics as targeted genome editing finally becomes achievable. Targeting nucleases, including ZFN and transcription activator-like effector nuclease (TALEN), provide high efficiency in inducing locus-specific DNA breaks in somatic and germline tissue (Bedell et al., 2012). Recently, the CRISPR-Cas system, using guide RNA to direct site-specific DNA cleavage by the Cas endonuclease, has been shown to work as efficiently as ZFN or TALEN (Hwang et al., 2013). The system is considerably simpler and easier to construct, and therefore should be amenable for automation and high-throughput use. Moreover, recent studies also demonstrate that a combination of two targeting nuclease further improves an efficiency of targeted deletions in zebrafish and allows deletion of large genomic fragments (Lim et al., 2013; Ma et al., 2013). Concurrently, annotation of the zebrafish genome has improved greatly (Zv9, Ensembl) with improved mapping of ESTs and difficult regions, which allows genome-wide precise design of targeted editing. When making a mutant in zebrafish becomes of such an ease, do we still need forward genetic screen? One undeniable advantage of forward genetic screen is that it allows isolation of mutants of novel genes that has not been characterized before. On the other hand, the simplicity of CRISPR-Cas system coupled with systematic *in silico* design of targeted sequences probably would bring zebrafish genetic screen into a new era.

4.4 Novel roles of Kv6.4/Kv2.1 in embryonic brain development

First cloned by Ottschytsch et al. (2002) from human cDNA library, Kv6.4 has been shown to have strong expression in the brain and low expression in liver, small intestine and colon in human when RT-PCR and cDNA libraries of different human tissues were used. However, the exact tissue localization was not demonstrated. The initial study suggested that Kv6.4 belongs to electrically 'silent' voltage-gated potassium (KvS) channel α subunits that do not form homotetramers but form heteroteramers with Kv2.1 subunits. This generates a functional Kv2.1/Kv6.4 channel complex in which the Kv6.4 subunit modulates the Kv2 current (Ottschytsch et al., 2002). Unlike the spatially restricted Kv6.4, Kv2.1 has ubiquitous expression that could be detected in almost all human tissues. Therefore, it seems that Kv2.1 subfamily uses interaction with the ‘silent’ subunit to diversify its function. Here, our results by *in situ* hybridization demonstrated a tissue-specific expression of this gene seem to support this diversification. The two zebrafish paralogues of *kcng4* (*kcng4a* and *kcng4b*) both have distinct tissue expression patterns. We find that transcripts of *kcng4a* localize to sensory cells (Figure 3.13) whereas *kcng4b* and *kcnb1* localize mainly to embryonic brain ventricular zone, and some other tissues later on (Figure 3.14 and Figure 3.17). As Kv6.4 forms obligatory heterotetramer in order to form functional Kv channels and to conduct current, *kcng4b* presumably regulates *kcnb1* whereas *kcng4a* may regulate some other Kv subunit from Kv1-Kv4 subfamilies that is expressed in sensory cells.

So far, little is known about the function of Kv6.4 *in vivo*. The only piece of evidence came from a biophysical characterization of whole cell voltage-gated K+ current ($I_{K(V)}$) in isolated urinary bladder smooth muscle (UBSM) cells. It demonstrated for the first time that in a native whole cell an efficient K+ efflux takes place due to formation of heterotetramer channels that consist of Kv2.1 and Kv5.1 and/or Kv6 (Kv6.1-Kv6.3) subunits (Thorneloe and Nelson, 2003). This stresses the importance of heterotetramer configuration in a native physiological context.

Our analyses of an insertional *kcng4b* mutant demonstrated for the first time the *in vivo* function of Kv6.4b in regulating embryonic brain ventricle inflation during zebrafish embryonic development. Loss of Kv6.4b results in neuroepithelial cell delamination, ventricle dilation and hydrocephalus in zebrafish embryos (Figure 3.10), indicating a regulatory role of Kv6.4b in modulation of Kv2.1 subunits. We also show that overexpression of Kv2.1 results in a similar phenotype as that caused by a loss of Kv6.4b function (Figure 3.15). This suggests an antagonizing function of Kv6.4b and Kv2.1 during regulation of brain ventricle formation. Based on their similar expression patterns in the brain ventricular zone, we propose that Kv6.4b regulates zebrafish embryonic brain ventricle formation by forming Kv2.1/K6.4b heterotetramer.

4.5 Mechanisms of regulation by Kv6.4/Kv2.1 heterotetramer

How does the 'silent' Kv6.4 subunit modulate Kv2.1 function? First, like most KvS subunits, Kv6 exerts a reduction of Kv2 current density when co-expressed in a heterologous system. For example, it has been demonstrated that the Kv6.1 subunit reduces Kv2 current density (Bocksteins et al., 2009a). This reduction is probably due to ER retention of the Kv2/Kv6 heterotetramer compared to Kv2 homotetramer (Ottschytsch et al., 2005). Second, Kv2.1/Kv6.4 heterotetramers have altered biophysical properties. In general, the co-expression with KvS subunits induces a shift in the voltage-dependency of activation that can be both in a hyperpolarized and depolarized direction (Bocksteins and Snyders, 2012). In contrast, the voltage dependence of inactivation is mostly shifted towards hyperpolarization. In addition, many KvS subunits slow the activation kinetics as well as the inactivation and deactivation kinetics. Therefore, the silent KvS subunits act as functional modifiers of the Kv2 channels. Specifically, the voltage-dependency of Kv6.4 appears to correspond to a strong (-40 mV) hyperpolarization shift in the voltage-dependence of steady state inactivation of Kv6.4/Kv2.1 heterotetrameric channels, as compared to Kv2.1 homotetramer channels. It has been suggested that if the 3:1 stoichiometry proposed for Kv2.1/Kv9.3 (Kerschensteiner et al., 2005) also applies to Kv2.1/Kv6.4 heterotetramer, a single Kv6.4 subunit is sufficient to initiate channel inactivation (Bocksteins et al., 2012). Therefore, we propose that Kv6.4b modulates Kv2.1 function in zebrafish embryonic brain neuroepithelium by forming Kv6.4b/Kv2.1 heterotetramers, which display decreased current density and hyperpolarization shift in the voltage-dependence that causes efficient inactivation of channel conductance.

Interestingly, our data demonstrate that transcripts of *kcng4a* are only detected in the sensory cells of cranial ganglia (Figure 3.13), but no *kcnb1* transcripts were detected in these regions at 30 hpf (Figure 3.17). As a specific and obligatory silent subunit, Kv6.4a must form heterotetramer with functional subunits from Kv1-Kv4 subfamily in order to exert its regulatory function. So far, only Kv6.4/Kv2.1 heterologous assembly has been reported by overexpression studies in cultured cells (Bocksteins and Snyders, 2012; Ottschytsch et al., 2002). As only one Kv2.1 has been annotated so far and its distinct tissue expression pattern already excludes the possibility of a Kv6.4a/Kv2.1 configuration, search for a functional subunit that can form heterotetramer with Kv6.4a in sensory cells will be of interest for future studies. This would definitely advance our understanding of the modulatory roles of Kv6.4 that diversify the function of Kv channels in different tissues.

4.6 Ion transport in brain ventricle inflation

A key process in brain ventricle formation is secretion of embryonic CSF (eCSF) into the ventricular lumen. Due to its inaccessible nature, eCSF production and embryonic ventricles formation are little studied in mammals. However, studies analysing ion transport in the neuroepithelial cells lining the adult choroid plexuses provide valuable insights. These cells secrete CSF by a process involving transport of ions including Na+, K+, Cl- and HCO_3- into the ventricles of the brain (Brown et al., 2004). The NaKATPase is a heterodimer normally consisting of two polypeptides, one α and one β subunit. The α subunit mediates the transport of three Na+ out of the cell and two K+ into the cell at the expense of a single molecule of ATP, and is thought to be the major pump for Na+ secretion into the CSF. Immunostaining studies demonstrated that the α subunit of NaKATPase was found to be localized exclusively at the apical brush border of rat and mouse choroid plexus (Ernst et al., 1986; Masuzawa et al., 1984). Inhibition of the pump by the inhibitor, ouabain, has been shown to reduce the CSF secretion and the movement of Na+ into the CSF. Similar function exists in zebrafish embryonic brain. The *snakehead* mutant, which lacks NaKATPase activity, fails to inflate the brain ventricles (Lowery and Sive, 2005). In addition, intracellular Na+ concentrations were increased in NaKATPase knockdown zebrafish embryos and embryos treated by the pump inhibitor, ouabain (Chang et al., 2012). Therefore, it is likely that embryonic brain ventricles inflate by an osmotic gradient formed as a result of membrane potential difference, under control of NaKATPase and other pumps and channels.

Among them, Kv channels are thought to provide a major route for K+ efflux into CSF of the ventricle lumen. In adult mammalian brain, studies by Zeuthen and Wright (1981) indicated that more than 90% of K+ leaves bullfrog epithelial cells via K+ channels in the apical membrane of choroid plexus. Speake et al. (2004) has also showed that Kv1.1 and Kv1.3 channel proteins are present in the rat choroid plexus and the two Kv channels contribute to the delayed-rectifying K+ conductance in choroid plexus epithelial cells. In postnatal mice, GFAP-expressing neural progenitor cells (NPC) in the subventricular zone (SVZ) display delayed-rectifying K+ currents, presumably generated by Kv3.1, which contribute to K+ transport, buffering, and maintain hyperpolarized resting potentials (Liu et al., 2006). Moreover, in cultured embryonic neural progenitor cells (eNPC) derived from the embryonic rat (E15) SVZ, Kv2.1 and Kv4.3 are shown to be expressed in these progenitor cells and associated with the delayed-rectifier and A-type currents, respectively, implying an early expression of Kv channel in eNPC (Smith et al., 2008).

Our results push the timeline one step earlier and demonstrate that Kv2.1 and Kv6.4b are expressed in pluripotent neural stem cells (NSC) of the ventricular zone lining the ventricles of embryonic brain (Figure 3.14, 3.17). By analysis of a hydrocephalus *kcng4b* mutant, we provide the first *in vivo* evidence that Kv6.4b function is required for regulating brain ventricle inflation (Figure 3.10). Through overexpression by mRNA injection, we also show that gain-of-function of Kv6.4b leads to an absence of ventricle inflation in embryonic brain (Figure 3.15, 3.16). Therefore, our data supports an essential role of Kv6.4b in modulating Kv2.1 function during brain ventricle inflation.

4.7 Ion channels and neuroepithelial cell proliferation and cell death

We observed decreased neuroepithelial cell proliferation in embryos with overexpression of *kcng4b* mRNA (Figure 3.15, H; 3.20). These embryos also displayed an absence of brain ventricle phenotype. Conversely, loss of *kcng4b* activity leads to hyper-proliferative neuroepithelium and mutant embryos developed hydrocephalus (over-inflated brain ventricle) (Figure 3.21). Such correlation between ventricle size and a rate of neural cell proliferation seems consistent with previous literature: the bigger the ventricle, the greater the amount of subsequent cell proliferation (Lowery and Sive, 2009). Desmond and Jacobson (1977) demonstrates that drainage of eCSF leads to reduced cell proliferation and increased apoptosis in the developing chick brain, suggesting eCSF is necessary for neuroepithelia proliferation. Indeed, a 50-fold increase in intraluminal pressure has been measured during chick brain ventricle expansion, and artificial increase of pressure by saline injection increases neuroepithelial mitoses (Desmond et al., 2005). This suggests that the intraluminal pressure exerted on the ventricular wall by eCSF fluid could drive the surrounding neuroepithelial to undergo proliferation, and this could possibly explain the increased mitotic cells observed in the hydrocephalic *kcng4b* mutant brain (Figure 3.21, D). Although the mechanism by which fluid pressure affects brain development is not fully understood, it has effects on other organs. For example, blood flow modifies the morphology of atrium and ventricular lumens in the zebrafish heart (Berdougo et al., 2003). In zebrafish intestine, electrochemical gradient generated by NaKATPase produces asymmetric ion distribution required for luminal fluid accumulation that eventually leads to an expansion of multiple small lumens and provide the force for their final coalescence into a single lumen (Bagnat et al., 2007).

However, we also observed an increase in a number of mitotic cells in the neuroepithelium of *kcng4b* mutant at 24 hpf (Figure 3.21, A and B). At this stage, the ventricle inflation phenotype is not fully manifested yet, hence ventricle size in *kcng4b* mutant and wild type embryos is approximately the same (Figure 3.10, C and D). This observation suggests that apart from the external fluid pressure an intrinsic mechanism probably exists, which is responsible for the over-proliferation observed in the neuroepithelium of *kcng4b* mutant.

Cell proliferation is a crucial function strictly controlled by a number of independent mechanisms. One of them is ion channel activity. It is generally believed that cells require K+ to proliferate (Wonderlin and Strobl, 1996). Kv channels have been reported to be involved in the proliferation of varieties of cell types, including tumour cells. Overexpression of the Kv channels and related channel activity could trigger neoplastic process. Lan et al. (2005) has demonstrated the existence of I_{DR} current (typically generated by Kv channels) in gastric cancer cells and downregulation of Kv1.5 by RNA interference (RNAi) or treatment of these cells with Kv inhibitors significantly reduced their proliferation and tumorigenicity. Studies by Suzuki and Takimoto (2004) demonstrate an existence of Kv2.1 and the silent regulator subunit Kv9.3 in cervical adenocarcinoma cell lines, and treatment with specific Kv2.1 blockers suppresses growth of these cells. Similarly, down regulation of Kv1.1 or Nav1.5 using the same approach suppresses gastric epithelial cell proliferation

(Wu et al., 2006). Furthermore, etraethylammonium (TEA) mediated blockage of Kv, presumably Kv3.1, inhibited proliferation of dissociated neurosphere-derived NPCs from the forebrain SVZ of adult mice (Yasuda et al., 2008). These findings indicate the existence of a diverse repertoire of Kv ion channels that modulate cell proliferation.

Although the mechanism by which ion channels control cell proliferation is not fully understood, there is some experimental evidence that allow formulation of some ideas. It is now believed that membrane hyperpolarization is required for cell cycle progression from G0/G1 to G1 and to S phases (Pardo, 2004; Wonderlin and Strobl, 1996). Cell cycle-dependent changes in I_{DR} have been observed with parallel alteration of mRNA levels of Kv1.2 and Kv2.1 (responsible for I_{DR}) in rat mesenchymal stem cells (MSC) (Deng et al., 2007). In addition, pharmacological blockage of or RNAi-mediated knockdown of Kv2.1 inhibits cell proliferation. As blockage of I_{DR} results in a depolarization of membrane potential in rat MSC, the inhibition of cell proliferation is likely caused by interference with cell cycle progression.

This possibly explains an increase in mitotic cells observed in the embryonic brain of *kcng4b* mutant zebrafish (Figure 3.21, B and D). Loss of *kcng4b* function removes the inhibitory function of Kv6.4b on Kv2.1 resulting in increase of Kv2.1 homotetramers in the progenitor cells of the ventricular zone. These homotetramers form functional Kv2.1 channels, which results in increased I_{DR} current density and hyperpolarization of the membrane potential hence increased cell proliferation. Moreover, the hyperpolarized membrane potential also causes opening of aquaporin water channels present on the apical membrane and formation of osmotic gradient, generating more fluid accumulation inside the brain ventricle. Acting in a way of positive feedback loop, the building-up of fluid pressure results in brain ventricle dilation, causing hydrocephalus. This increases further a mitogenic index in the neuroepithelia (Figure 3.21, D).

Conversely, an overexpression of Kv6.4b artificially increases Kv2.1/Kv6.4b heterotetramer formation in the neuroepithelia, thereby decreases the number of Kv2.1 homotetramers. This presumably blocks/inactivates the normal Kv2.1 channel clustering at the surface and alters the membrane potential of neuroepithelia cells towards depolarization. As hyperpolarized membrane potential is required for both cell cycle progression and aquaporin-mediated fluid flow, upon depolarization of the cell membrane embryos display decreased mitotic index (Figure 3.20, A) and underinflated brain ventricle (Figure 3.15, A-H). Therefore, our data supports a role of K+ in modulating cell proliferation, and provides the first *in vivo* evidence that modulation of K+ by a silent Kv6.4b subunit is essential for embryonic neuroepithelium proliferation and ventricle inflation in zebrafish.

Apart from cell proliferation, there is increasing evidence that K+ channels are involved in regulating cell apoptosis, as excessive K+ efflux has been shown to be a prerequisite for neurons to undergo apoptosis, and modification of Kv2.1 regulates neuronal survival/death dynamics. Ca+/calcineurin-dependent dephosphorylation of Kv2.1 results in lateral dispersion of Kv2.1 channel clusters and a ~20 mV hyperpolarization shift in the voltage dependence of channel activation (Misonou et al., 2004). This enhances channel opening with minimal depolarization, limiting firing frequency and increasing the refractory period duration, thereby providing neuroprotection during the early phase of hyperexcitable assaults (Mohapatra et al., 2009). In contrast, phosphorylation of Kv2.1 by p38 mitogen-activated protein kinase increases current density and K+ efflux, resulting in induction of neuronal apoptosis (Pal et al., 2003). Recent studies by Wu et al. (2013) also demonstrated that Kv2.1 oxidation-mediated apoptosis of mammalian cells is a result of defective endocytosis of Kv2.1 oligomers. Since our data support a regulatory role of Kv6.4b on Kv2.1 in embryonic brain ventricular zone, whether it will have a similar function in regulating early embryonic brain apoptosis could be of interest for further studies.

4.8 Ion channels and neuroepithelium integrity

Formation of brain ventricles requires both production of CSF and its retention in the ventricle. The latter is accomplished by a barrier function provided by the neuroepithelial cells lining the ventricles. As *kcng4b* transcripts have been detected mainly in these cells at the ‘window period’ when brain ventricles start to inflate (Figure 3.14, D and I), we checked apical polarity marked by αPKC at 24 hpf and the apical junction complex using phalloidin (F-actin) at 48 hpf.

In wild type embryos, apical membrane of neuroepithelial cells marked by αPKC at the ventricular zone forms a continuous and smooth apical band lining the ventricles of forebrain, midbrain and hindbrain, respectively (Figure 3.22, A, C and E). Loss of *kcng4b* led to discontinuous and scattered apical membrane, with non-polarized cells present throughout the ventricular zone of all three brain ventricles (Figure 3.22, B, D and F). Notably, in the forebrain ventricle of *kcng4b* mutant, where delaminated cells could be observed clearly, non-polarized cells (without αPKC staining) are observed, presumably due to over proliferation and loss of polarity. Similarly, apical junctions, marked by phalloidin, become discontinuous and scattered in *kcng4b* mutant at 48 hpf (Figure 3.23), suggesting that a loss of polarity in neuroepithelial cells of *kcng4b* mutant is irreversible and non-recoverable. These data suggest that *kcng4b* is required for the formation of a polarized and continuous neuroepithelium important for brain ventricle development, and loss of *kcng4b* leads to absence of a polarized and continuous neuroepithelium.

The loss of polarized and continuous neuroepithelium phenotype displayed by *kcng4b* mutant is reminiscent of that described in previous studies by Chang et al. (2012) where discontinuous and non-polarized cells were observed in zebrafish embryos deficient in NaKATPase (*atp1a1*) function. An apical membrane and apical junction complex are scattered and patchy in these embryos. This is possibly due to a lack of downstream activation of RhoA, a small GTPase, as injection of RhoA mRNA restores a continuous neuroepithelium in these embryos, although brain ventricle is still absent (Chang et al., 2012). This data also suggest that formation of cohesive neuroepithelium and brain ventricle inflation could be due to two discrete mechanisms although the same protein/protein complex might have roles in both events. It is possible that the novel *kcng4b* channel subunit might have a similar role in the formation of a cohesive neuroepithelium in zebrafish, apart from its regulatory role in embryonic brain ventricle inflation.

How does a Kv channel silent subunit Kv6.4b modulate neuroepithelium polarity? Is it a consequence of altered neuroepithelial cell proliferation or a discrete event? Although the mechanism is not fully understood, we could gain some insights from the analyses of NaKATPase-deficient embryos. NaKATPase is a well-known ion pump for modulating membrane potential in neurons and is essential for generating action potential. It has been proposed that depolarization of the cell leads to RhoA activation. In cultured cells, depolarization of epithelial cells has been shown to activate the Ras/MEK/ERK pathway (Waheed et al., 2010), by promoting GEF activity and increasing RhoA-GTP level. It has been proposed that NaKATPase is involved in the regulation of RhoA mediated actin polymerization. The active actin polymerization may then provide the necessary force to mobilize the tight junction strands at the apical-lateral region in order to establish functional tight junctions (Rajasekaran and Rajasekaran, 2003). It has also been proposed that RhoA regulates paracellular permeability in the zebrafish neuroepithelium (Chang et al., 2012). In addition, loss of Claudin5a, a barrier claudin and a component of a tight junction complex responsible for paracellular ion transport and selectivity also leads to brain ventricle inflation and neuroepithelial permeability defects in zebrafish (Zhang et al., 2010). Interestingly, a loss of Claudin5a does not affect cell polarity and tissue integrity of the neuroepithelium. Therefore, Claudin5a may act downstream of cell polarity regulation and provide a cerebral barrier function in sealing the neuroepithelial tight junction for the initial fluid accumulation and brain inflation.

Whether similar mechanism may underlie *kcng4b*-mediated control of neuroepithelium polarity remains to be elucidated. To check this, injection of RhoA mRNA to restore neuroepithelium apical/basal polarity could be a good approach to begin with. Also, a neuroepithelium permeability assay may be conducted on *kcng4b* mutant embryos to check the barrier function of the neuroepithelium is affected due to loss of polarity. These future studies would definitely help to shed light on a mechanism of interaction between ion channels, cell polarity and tight junction complex in the embryonic neuroepithelium.

4.9 Conclusion

In this study, a forward genetic screen using *Tol2* transposon mediated insertional mutagenesis strategy was carried out aiming to search for novel molecular regulators of brain circulation. Among 130 insertion sites that were successfully mapped, 32 insertions were found to be located in intronic sequences with correct *cis*-orientation with the tagged gene, thus being potentially mutagenic. In addition, four insertions were in exons of genes, causing direct disruption of coding sequences.

A *kcng4b* mutant, which lacks voltage-gated potassium channel Kv6.4b silent subunit function, displayed developmental defects in embryonic brain ventricles, including neuroepithelial cells delamination, ventricle dilation and thus hydrocephalus. Functional analyses of the *kcng4b* mutant demonstrated for the first time that the silent Kv6.4b subunits play an essential role in regulating embryonic brain lumen inflation by modulating neuroepithelial cell proliferation and maintaining neuroepithelium integrity, presumably through the formation of Kv2.1/Kv6.4b heterotetramers at the embryonic brain ventricular zone. Therefore, we propose that the silent Kv6.4b subunits function by modulating Kv2.1 function during vertebrate embryonic brain morphogenesis

Chapter 5. References

Alexandre, P., Reugels, A.M., Barker, D., Blanc, E., Clarke, J.D., 2010. Neurons derive from the more apical daughter in asymmetric divisions in the zebrafish neural tube. Nature neuroscience 13, 673-679.

Amsterdam, A., Varshney, G.K., Burgess, S.M., 2011. Retroviral-mediated Insertional Mutagenesis in Zebrafish. Methods in cell biology 104, 59-82.

Asakawa, K., Suster, M.L., Mizusawa, K., Nagayoshi, S., Kotani, T., Urasaki, A., Kishimoto, Y., Hibi, M., Kawakami, K., 2008. Genetic dissection of neural circuits by Tol2 transposon-mediated Gal4 gene and enhancer trapping in zebrafish. Proceedings of the National Academy of Sciences of the United States of America 105, 1255-1260.

Bachy, I., Kozyraki, R., Wassef, M., 2008. The particles of the embryonic cerebrospinal fluid: how could they influence brain development? Brain research bulletin 75, 289-294.

Badaut, J., Lasbennes, F., Magistretti, P.J., Regli, L., 2002. Aquaporins in brain: distribution, physiology, and pathophysiology. Journal of cerebral blood flow and metabolism : official journal of the International Society of Cerebral Blood Flow and Metabolism 22, 367-378.

Bagnat, M., Cheung, I.D., Mostov, K.E., Stainier, D.Y., 2007. Genetic control of single lumen formation in the zebrafish gut. Nature cell biology 9, 954-960.

Bedell, V.M., Wang, Y., Campbell, J.M., Poshusta, T.L., Starker, C.G., Krug, R.G., 2nd, Tan, W., Penheiter, S.G., Ma, A.C., Leung, A.Y., Fahrenkrug, S.C., Carlson, D.F., Voytas, D.F., Clark, K.J., Essner, J.J., Ekker, S.C., 2012. In vivo genome editing using a high-efficiency TALEN system. Nature 491, 114-118.

Berdougo, E., Coleman, H., Lee, D.H., Stainier, D.Y., Yelon, D., 2003. Mutation of weak atrium/atrial myosin heavy chain disrupts atrial function and influences ventricular morphogenesis in zebrafish. Development 130, 6121-6129.

Bernhardt, R.R., Chitnis, A.B., Lindamer, L., Kuwada, J.Y., 1990. Identification of spinal neurons in the embryonic and larval zebrafish. The Journal of comparative neurology 302, 603-616.

Bill, B.R., Balciunas, D., McCarra, J.A., Young, E.D., Xiong, T., Spahn, A.M., Garcia-Lecea, M., Korzh, V., Ekker, S.C., Schimmenti, L.A., 2008. Development and Notch signaling requirements of the zebrafish choroid plexus. PloS one 3, e3114.

Bocksteins, E., Snyders, D.J., 2012. Electrically silent Kv subunits: their molecular and functional characteristics. Physiology 27, 73-84.

Bocksteins, E., Labro, A.J., Snyders, D.J., Mohapatra, D.P., 2012. The electrically silent Kv6.4 subunit confers hyperpolarized gating charge movement in Kv2.1/Kv6.4 heterotetrameric channels. PloS one 7, e37143.

Bocksteins, E., Raes, A.L., Van de Vijver, G., Bruyns, T., Van Bogaert, P.P., Snyders, D.J., 2009a. Kv2.1 and silent Kv subunits underlie the delayed rectifier K+ current in cultured small mouse DRG neurons. American journal of physiology. Cell physiology 296, C1271-1278.

Bocksteins, E., Labro, A.J., Mayeur, E., Bruyns, T., Timmermans, J.P., Adriaensen, D., Snyders, D.J., 2009b. Conserved negative charges in the N-terminal tetramerization domain mediate efficient assembly of Kv2.1 and Kv2.1/Kv6.4 channels. The Journal of biological chemistry 284, 31625-31634.

Borck, G., Ur Rehman, A., Lee, K., Pogoda, H.M., Kakar, N., von Ameln, S., Grillet, N., Hildebrand, M.S., Ahmed, Z.M., Nurnberg, G., Ansar, M., Basit, S., Javed, Q., Morell, R.J., Nasreen, N., Shearer, A.E., Ahmad, A., Kahrizi, K., Shaikh, R.S., Ali, R.A., Khan, S.N., Goebel, I., Meyer, N.C., Kimberling, W.J., Webster, J.A., Stephan, D.A., Schiller, M.R., Bahlo, M., Najmabadi, H., Gillespie, P.G., Nurnberg, P., Wollnik, B., Riazuddin, S., Smith, R.J., Ahmad, W., Muller, U., Hammerschmidt, M., Friedman, T.B., Riazuddin, S., Leal, S.M., Ahmad, J., Kubisch, C., 2011. Loss-of-function mutations of ILDR1 cause autosomal-recessive hearing impairment DFNB42. American journal of human genetics 88, 127-137.

Brodbelt, A., Stoodley, M., 2007. CSF pathways: a review. British journal of neurosurgery 21, 510-520.

Brown, P.D., Davies, S.L., Speake, T., Millar, I.D., 2004. Molecular mechanisms of cerebrospinal fluid production. Neuroscience 129, 957-970.

Bulat, M., Lupret, V., Orehkovic, D., Klarica, M., 2008. Transventricular and transpial absorption of cerebrospinal fluid into cerebral microvessels. Collegium antropologicum 32 Suppl 1, 43-50.

Carmichael, C., Westerfield, M., Varga, Z.M., 2009. Cryopreservation and in vitro fertilization at the zebrafish international resource center. Methods in molecular biology 546, 45-65.

Chamberlain, C.E., Jeong, J., Guo, C., Allen, B.L., McMahon, A.P., 2008. Notochord-derived Shh concentrates in close association with the apically positioned basal body in neural target cells and forms a dynamic gradient during neural patterning. Development 135, 1097-1106.

Chang, J.T., Lowery, L.A., Sive, H., 2012. Multiple roles for the Na,K-ATPase subunits, Atp1a1 and Fxyd1, during brain ventricle development. Developmental biology 368, 312-322.

Chikly, B., Quaghebeur, J., 2013. Reassessing cerebrospinal fluid (CSF) hydrodynamics: a literature review presenting a novel hypothesis for CSF physiology. Journal of bodywork and movement therapies 17, 344-354.

Childs, S., Chen, J.N., Garrity, D.M., Fishman, M.C., 2002. Patterning of angiogenesis in the zebrafish embryo. Development 129, 973-982.

Clark, K.J., Balciunas, D., Pogoda, H.M., Ding, Y., Westcot, S.E., Bedell, V.M., Greenwood, T.M., Urban, M.D., Skuster, K.J., Petzold, A.M., Ni, J., Nielsen, A.L., Patowary, A., Scaria, V., Sivasubbu, S., Xu, X., Hammerschmidt, M., Ekker, S.C., 2011. In vivo protein trapping produces a functional expression codex of the vertebrate proteome. Nature methods 8, 506-515.

Deng, X.L., Lau, C.P., Lai, K., Cheung, K.F., Lau, G.K., Li, G.R., 2007. Cell cycle-dependent expression of potassium channels and cell proliferation in rat mesenchymal stem cells from bone marrow. Cell proliferation 40, 656-670.

Desmond, M.E., Jacobson, A.G., 1977. Embryonic brain enlargement requires cerebrospinal fluid pressure. Developmental biology 57, 188-198.

Desmond, M.E., Schoenwolf, G.C., 1985. Timing and positioning of occlusion of the spinal neurocele in the chick embryo. The Journal of comparative neurology 235, 479-487.

Desmond, M.E., Levitan, M.L., Haas, A.R., 2005. Internal luminal pressure during early chick embryonic brain growth: descriptive and empirical observations. The anatomical record. Part A, Discoveries in molecular, cellular, and evolutionary biology 285, 737-747.

Doganli, C., Beck, H.C., Ribera, A.B., Oxvig, C., Lykke-Hartmann, K., 2013. alpha3Na+/K+-ATPase deficiency causes brain ventricle dilation and abrupt embryonic motility in zebrafish. The Journal of biological chemistry 288, 8862-8874.

Dokmanovic-Chouinard, M., Chung, W.K., Chevre, J.C., Watson, E., Yonan, J., Wiegand, B., Bromberg, Y., Wakae, N., Wright, C.V., Overton, J., Ghosh, S., Sathe, G.M., Ammala, C.E., Brown, K.K., Ito, R., LeDuc, C., Solomon, K., Fischer, S.G., Leibel, R.L., 2008. Positional cloning of "Lisch-Like", a candidate modifier of susceptibility to type 2 diabetes in mice. PLoS genetics 4, e1000137.

Doyon, Y., McCammon, J.M., Miller, J.C., Faraji, F., Ngo, C., Katibah, G.E., Amora, R., Hocking, T.D., Zhang, L., Rebar, E.J., Gregory, P.D., Urnov, F.D., Amacher, S.L., 2008. Heritable targeted gene disruption in zebrafish using designed zinc-finger nucleases. Nature biotechnology 26, 702-708.

Dubreuil, V., Marzesco, A.M., Corbeil, D., Huttner, W.B., Wilsch-Brauninger, M., 2007. Midbody and primary cilium of neural progenitors release extracellular membrane particles enriched in the stem cell marker prominin-1. The Journal of cell biology 176, 483-495.

Ernst, S.A., Palacios, J.R., 2nd, Siegel, G.J., 1986. Immunocytochemical localization of Na+,K+-ATPase catalytic polypeptide in mouse choroid plexus. The journal of histochemistry and cytochemistry : official journal of the Histochemistry Society 34, 189-195.

Farkas, L.M., Huttner, W.B., 2008. The cell biology of neural stem and progenitor cells and its significance for their proliferation versus differentiation during mammalian brain development. Current opinion in cell biology 20, 707-715.

Garcia-Lecea, M., Kondrychyn, I., Fong, S.H., Ye, Z.R., Korzh, V., 2008. In vivo analysis of choroid plexus morphogenesis in zebrafish. PloS one 3, e3090.

Gato, A., Moro, J.A., Alonso, M.I., Pastor, J.F., Represa, J.J., Barbosa, E., 1993. Chondroitin sulphate proteoglycan and embryonic brain enlargement in the chick. Anatomy and embryology 188, 101-106.

Gato, A., Moro, J.A., Alonso, M.I., Bueno, D., De La Mano, A., Martin, C., 2005. Embryonic cerebrospinal fluid regulates neuroepithelial survival, proliferation, and neurogenesis in chick embryos. The anatomical record. Part A, Discoveries in molecular, cellular, and evolutionary biology 284, 475-484.

Gutzman, J.H., Sive, H., 2010. Epithelial relaxation mediated by the myosin phosphatase regulator Mypt1 is required for brain ventricle lumen expansion and hindbrain morphogenesis. Development 137, 795-804.

Higashi, T., Tokuda, S., Kitajiri, S., Masuda, S., Nakamura, H., Oda, Y., Furuse, M., 2013. Analysis of the 'angulin' proteins LSR, ILDR1 and ILDR2--tricellulin recruitment, epithelial barrier function and implication in deafness pathogenesis. Journal of cell science 126, 966-977.

Horne-Badovinac, S., Lin, D., Waldron, S., Schwarz, M., Mbamalu, G., Pawson, T., Jan, Y., Stainier, D.Y., Abdelilah-Seyfried, S., 2001. Positional cloning of heart and soul reveals multiple roles for PKC lambda in zebrafish organogenesis. Current biology : CB 11, 1492-1502.

Hwang, W.Y., Fu, Y., Reyon, D., Maeder, M.L., Tsai, S.Q., Sander, J.D., Peterson, R.T., Yeh, J.R., Joung, J.K., 2013. Efficient genome editing in zebrafish using a CRISPR-Cas system. Nature biotechnology 31, 227-229.

Kerschensteiner, D., Soto, F., Stocker, M., 2005. Fluorescence measurements reveal stoichiometry of K+ channels formed by modulatory and delayed rectifier alpha-subunits. Proceedings of the National Academy of Sciences of the United States of America 102, 6160-6165.

Kimmel, C.B., Ballard, W.W., Kimmel, S.R., Ullmann, B., Schilling, T.F., 1995. Stages of embryonic development of the zebrafish. Developmental dynamics : an official publication of the American Association of Anatomists 203, 253-310.

Klarica, M., Oreskovic, D., Bozic, B., Vukic, M., Butkovic, V., Bulat, M., 2009. New experimental model of acute aqueductal blockage in cats: effects on cerebrospinal fluid pressure and the size of brain ventricles. Neuroscience 158, 1397-1405.

Kleinjan, D.A., Bancewicz, R.M., Gautier, P., Dahm, R., Schonthaler, H.B., Damante, G., Seawright, A., Hever, A.M., Yeyati, P.L., van Heyningen, V., Coutinho, P., 2008. Subfunctionalization of duplicated zebrafish pax6 genes by cis-regulatory divergence. PLoS genetics 4, e29.

Kondrychyn, I., Garcia-Lecea, M., Emelyanov, A., Parinov, S., Korzh, V., 2009. Genome-wide analysis of Tol2 transposon reintegration in zebrafish. BMC genomics 10, 418.

Lan, M., Shi, Y., Han, Z., Hao, Z., Pan, Y., Liu, N., Guo, C., Hong, L., Wang, J., Qiao, T., Fan, D., 2005. Expression of delayed rectifier potassium channels and their possible roles in proliferation of human gastric cancer cells. Cancer biology & therapy 4, 1342-1347.

Leung, L., Klopper, A.V., Grill, S.W., Harris, W.A., Norden, C., 2011. Apical migration of nuclei during G2 is a prerequisite for all nuclear motion in zebrafish neuroepithelia. Development 138, 5003-5013.

Lim, S., Wang, Y., Yu, X., Huang, Y., Featherstone, M.S., Sampath, K., 2013. A simple strategy for heritable chromosomal deletions in zebrafish via the combinatorial action of targeting nucleases. Genome biology 14, R69.

Lister, J.A., Robertson, C.P., Lepage, T., Johnson, S.L., Raible, D.W., 1999. nacre encodes a zebrafish microphthalmia-related protein that regulates neural-crest-derived pigment cell fate. Development 126, 3757-3767.

Liu, X., Bolteus, A.J., Balkin, D.M., Henschel, O., Bordey, A., 2006. GFAP-expressing cells in the postnatal subventricular zone display a unique glial phenotype intermediate between radial glia and astrocytes. Glia 54, 394-410.

Liu, Y.G., Whittier, R.F., 1995. Thermal asymmetric interlaced PCR: automatable amplification and sequencing of insert end fragments from P1 and YAC clones for chromosome walking. Genomics 25, 674-681.

Lowery, L.A., Sive, H., 2005. Initial formation of zebrafish brain ventricles occurs independently of circulation and requires the nagie oko and snakehead/atp1a1a.1 gene products. Development 132, 2057-2067.

Lowery, L.A., Sive, H., 2009. Totally tubular: the mystery behind function and origin of the brain ventricular system. BioEssays : news and reviews in molecular, cellular and developmental biology 31, 446-458.

Lowery, L.A., De Rienzo, G., Gutzman, J.H., Sive, H., 2009. Characterization and classification of zebrafish brain morphology mutants. Anatomical record 292, 94-106.

Ma, A.C., Lee, H.B., Clark, K.J., Ekker, S.C., 2013. High efficiency In Vivo genome engineering with a simplified 15-RVD GoldyTALEN design. PloS one 8, e65259.

Martin, C., Bueno, D., Alonso, M.I., Moro, J.A., Callejo, S., Parada, C., Martin, P., Carnicero, E., Gato, A., 2006. FGF2 plays a key role in embryonic cerebrospinal fluid trophic properties over chick embryo neuroepithelial stem cells. Developmental biology 297, 402-416.

Masuzawa, T., Ohta, T., Kawamura, M., Nakahara, N., Sato, F., 1984. Immunohistochemical localization of Na+, K+-ATPase in the choroid plexus. Brain research 302, 357-362.

Meng, X., Noyes, M.B., Zhu, L.J., Lawson, N.D., Wolfe, S.A., 2008. Targeted gene inactivation in zebrafish using engineered zinc-finger nucleases. Nature biotechnology 26, 695-701.

Merkle, F.T., Alvarez-Buylla, A., 2006. Neural stem cells in mammalian development. Current opinion in cell biology 18, 704-709.

Misonou, H., Mohapatra, D.P., Trimmer, J.S., 2005. Kv2.1: a voltage-gated k+ channel critical to dynamic control of neuronal excitability. Neurotoxicology 26, 743-752.

Misonou, H., Mohapatra, D.P., Park, E.W., Leung, V., Zhen, D., Misonou, K., Anderson, A.E., Trimmer, J.S., 2004. Regulation of ion channel localization and phosphorylation by neuronal activity. Nature neuroscience 7, 711-718.

Mohapatra, D.P., Misonou, H., Pan, S.J., Held, J.E., Surmeier, D.J., Trimmer, J.S., 2009. Regulation of intrinsic excitability in hippocampal neurons by activity-dependent modulation of the KV2.1 potassium channel. Channels 3, 46-56.

Moreira, J., Deutsch, A., 2005. Pigment pattern formation in zebrafish during late larval stages: a model based on local interactions. Developmental dynamics : an official publication of the American Association of Anatomists 232, 33-42.

Moreno-Dominguez, A., Cidad, P., Miguel-Velado, E., Lopez-Lopez, J.R., Perez-Garcia, M.T., 2009. De novo expression of Kv6.3 contributes to changes in vascular smooth muscle cell excitability in a hypertensive mice strain. The Journal of physiology 587, 625-640.

Nagayoshi, S., Hayashi, E., Abe, G., Osato, N., Asakawa, K., Urasaki, A., Horikawa, K., Ikeo, K., Takeda, H., Kawakami, K., 2008. Insertional mutagenesis by the Tol2 transposon-mediated enhancer trap approach generated mutations in two developmental genes: tcf7 and synembryn-like. Development 135, 159-169.

Nielsen, S., Nagelhus, E.A., Amiry-Moghaddam, M., Bourque, C., Agre, P., Ottersen, O.P., 1997. Specialized membrane domains for water transport in glial cells: high-resolution immunogold cytochemistry of aquaporin-4 in rat brain. The Journal of neuroscience : the official journal of the Society for Neuroscience 17, 171-180.

Oreskovic, D., Klarica, M., 2010. The formation of cerebrospinal fluid: nearly a hundred years of interpretations and misinterpretations. Brain research reviews 64, 241-262.

Ottschytsch, N., Raes, A., Van Hoorick, D., Snyders, D.J., 2002. Obligatory heterotetramerization of three previously uncharacterized Kv channel alpha-subunits identified in the human genome. Proceedings of the National Academy of Sciences of the United States of America 99, 7986-7991.

Ottschytsch, N., Raes, A.L., Timmermans, J.P., Snyders, D.J., 2005. Domain analysis of Kv6.3, an electrically silent channel. The Journal of physiology 568, 737-747.

Pal, S., Hartnett, K.A., Nerbonne, J.M., Levitan, E.S., Aizenman, E., 2003. Mediation of neuronal apoptosis by Kv2.1-encoded potassium channels. The Journal of neuroscience : the official journal of the Society for Neuroscience 23, 4798-4802.

Parada, C., Gato, A., Bueno, D., 2005. Mammalian embryonic cerebrospinal fluid proteome has greater apolipoprotein and enzyme pattern complexity than the avian proteome. Journal of proteome research 4, 2420-2428.

Pardo, L.A., 2004. Voltage-gated potassium channels in cell proliferation. Physiology 19, 285-292.

Parinov, S., Kondrichin, I., Korzh, V., Emelyanov, A., 2004. Tol2 transposon-mediated enhancer trap to identify developmentally regulated zebrafish genes in vivo. Developmental dynamics : an official publication of the American Association of Anatomists 231, 449-459.

Park, M.K., Bae, Y.M., Lee, S.H., Ho, W.K., Earm, Y.E., 1997. Modulation of voltage-dependent K+ channel by redox potential in pulmonary and ear arterial smooth muscle cells of the rabbit. Pflugers Archiv : European journal of physiology 434, 764-771.

Petzold, A.M., Balciunas, D., Sivasubbu, S., Clark, K.J., Bedell, V.M., Westcot, S.E., Myers, S.R., Moulder, G.L., Thomas, M.J., Ekker, S.C., 2009. Nicotine response genetics in the zebrafish. Proceedings of the National Academy of Sciences of the United States of America 106, 18662-18667.

Pineda, R.H., Svoboda, K.R., Wright, M.A., Taylor, A.D., Novak, A.E., Gamse, J.T., Eisen, J.S., Ribera, A.B., 2006. Knockdown of Nav1.6a Na+ channels affects zebrafish motoneuron development. Development 133, 3827-3836.

Pongs, O., 1999. Voltage-gated potassium channels: from hyperexcitability to excitement. FEBS letters 452, 31-35.

Rajasekaran, A.K., Rajasekaran, S.A., 2003. Role of Na-K-ATPase in the assembly of tight junctions. American journal of physiology. Renal physiology 285, F388-396.

Redzic, Z.B., Preston, J.E., Duncan, J.A., Chodobski, A., Szmydynger-Chodobska, J., 2005. The Choroid Plexus-Cerebrospinal Fluid System: From Development to Aging. 71, 1-52.

Rohr, S., Bit-Avragim, N., Abdelilah-Seyfried, S., 2006. Heart and soul/PRKCi and nagie oko/Mpp5 regulate myocardial coherence and remodeling during cardiac morphogenesis. Development 133, 107-115.

Sakka, L., Coll, G., Chazal, J., 2011. Anatomy and physiology of cerebrospinal fluid. European annals of otorhinolaryngology, head and neck diseases 128, 309-316.

Sivasubbu, S., Balciunas, D., Amsterdam, A., Ekker, S.C., 2007. Insertional mutagenesis strategies in zebrafish. Genome biology 8 Suppl 1, S9.

Sivasubbu, S., Balciunas, D., Davidson, A.E., Pickart, M.A., Hermanson, S.B., Wangensteen, K.J., Wolbrink, D.C., Ekker, S.C., 2006. Gene-breaking transposon mutagenesis reveals an essential role for histone H2afza in zebrafish larval development. Mechanisms of development 123, 513-529.

Smith, D.O., Rosenheimer, J.L., Kalil, R.E., 2008. Delayed rectifier and A-type potassium channels associated with Kv 2.1 and Kv 4.3 expression in embryonic rat neural progenitor cells. PloS one 3, e1604.

Speake, T., Kibble, J.D., Brown, P.D., 2004. Kv1.1 and Kv1.3 channels contribute to the delayed-rectifying K+ conductance in rat choroid plexus epithelial cells. American journal of physiology. Cell physiology 286, C611-620.

Suzuki, T., Takimoto, K., 2004. Selective expression of HERG and Kv2 channels influences proliferation of uterine cancer cells. International journal of oncology 25, 153-159.

Svoboda, K.R., Linares, A.E., Ribera, A.B., 2001. Activity regulates programmed cell death of zebrafish Rohon-Beard neurons. Development 128, 3511-3520.

Thorneloe, K.S., Nelson, M.T., 2003. Properties and molecular basis of the mouse urinary bladder voltage-gated K+ current. The Journal of physiology 549, 65-74.

Urasaki, A., Morvan, G., Kawakami, K., 2006. Functional dissection of the Tol2 transposable element identified the minimal cis-sequence and a highly repetitive sequence in the subterminal region essential for transposition. Genetics 174, 639-649.

Vacher, H., Mohapatra, D.P., Trimmer, J.S., 2008. Localization and targeting of voltage-dependent ion channels in mammalian central neurons. Physiological reviews 88, 1407-1447.

Vajda, Z., Pedersen, M., Doczi, T., Sulyok, E., Nielsen, S., 2004. Studies of mdx mice. Neuroscience 129, 993-998.

Verbruggen, V., Ek, O., Georlette, D., Delporte, F., Von Berg, V., Detry, N., Biemar, F., Coutinho, P., Martial, J.A., Voz, M.L., Manfroid, I., Peers, B., 2010. The Pax6b homeodomain is dispensable for pancreatic endocrine cell differentiation in zebrafish. The Journal of biological chemistry 285, 13863-13873.

Waheed, F., Speight, P., Kawai, G., Dan, Q., Kapus, A., Szaszi, K., 2010. Extracellular signal-regulated kinase and GEF-H1 mediate depolarization-induced Rho activation and paracellular permeability increase. American journal of physiology. Cell physiology 298, C1376-1387.

Watanabe, K., Watson, E., Cremona, M.L., Millings, E.J., Lefkowitch, J.H., Fischer, S.G., LeDuc, C.A., Leibel, R.L., 2013. ILDR2: an endoplasmic reticulum resident molecule mediating hepatic lipid homeostasis. PloS one 8, e67234.

Wonderlin, W.F., Strobl, J.S., 1996. Potassium channels, proliferation and G1 progression. The Journal of membrane biology 154, 91-107.

Wu, W.K., Li, G.R., Wong, H.P., Hui, M.K., Tai, E.K., Lam, E.K., Shin, V.Y., Ye, Y.N., Li, P., Yang, Y.H., Luo, J.C., Cho, C.H., 2006. Involvement of Kv1.1 and Nav1.5 in proliferation of gastric epithelial cells. Journal of cellular physiology 207, 437-444.

Wu, X., Hernandez-Enriquez, B., Banas, M., Xu, R., Sesti, F., 2013. Molecular mechanisms underlying the apoptotic effect of KCNB1 K+ channel oxidation. The Journal of biological chemistry 288, 4128-4134.

Yasuda, T., Bartlett, P.F., Adams, D.J., 2008. K(ir) and K(v) channels regulate electrical properties and proliferation of adult neural precursor cells. Molecular and cellular neurosciences 37, 284-297.

Zappaterra, M.D., Lisgo, S.N., Lindsay, S., Gygi, S.P., Walsh, C.A., Ballif, B.A., 2007. A comparative proteomic analysis of human and rat embryonic cerebrospinal fluid. Journal of proteome research 6, 3537-3548.

Zappaterra, M.W., Lehtinen, M.K., 2012. The cerebrospinal fluid: regulator of neurogenesis, behavior, and beyond. Cellular and molecular life sciences : CMLS 69, 2863-2878.

Zeuthen, T., Wright, E.M., 1981. Epithelial potassium transport: tracer and electrophysiological studies in choroid plexus. The Journal of membrane biology 60, 105-128.

Zhang, J., Piontek, J., Wolburg, H., Piehl, C., Liss, M., Otten, C., Christ, A., Willnow, T.E., Blasig, I.E., Abdelilah-Seyfried, S., 2010. Establishment of a neuroepithelial barrier by Claudin5a is essential for zebrafish brain ventricular lumen expansion. Proceedings of the National Academy of Sciences of the United States of America 107, 1425-1430.

Appendix

Appendix Table 1. List of all insertion sites mapped by TAIL-PCR method

Family	Sex	No.	Chr.	Nucleotide	Ori	Region	Biotype	EntrezGene	Gene Name/Remarks
GB2	F	1	9	20507646	+	Intron	coding	hao2	Hydroxyacid oxidase 2 (long chain); zgc:63690
GB2	M	1	9	20507646	+	Intron	coding	hao2	Hydroxyacid oxidase 2 (long chain); zgc:63690
GB3	F	1	5	14351454	+	outside	NA	NA	NA
GB3	M	1	5	28196229	+	Intron	coding	bco2a	beta-carotene oxygenase 2a
GB4	F	1	7	59,166,786	+	Intron	coding	LOC566228	Potassium Voltage-gated channel, subfamily G, member 2- like
GB4	F	2	7	59,166,786	+	Intron	coding	LOC566228	Potassium Voltage-gated channel, subfamily G, member 2- like
GB4	F	3	7	59,166,786	+	Intron	coding	LOC566228	Potassium Voltage-gated channel, subfamily G, member 2- like
GB4	F	4	7	59,166,786	+	Intron	coding	LOC566228	Potassium Voltage-gated channel, subfamily G, member 2- like
GB6	F	1	12	16188779	-	Intron	coding	rnls	renalase, FAD-dependent amine oxidase; zgc:92286
GB7	F	1	15	18874197	-	outside	NA	NA	NA
GB8	F	1	4	69075368	-	outside	NA	NA	NA
			5	66192334	-	Intron	coding	anxalc	annexin A1c
GB8	M	1	9	14418062	-	Intron	coding	pard3b	human and mouse par-3 partitioning defective 3 homolog B
			3	30400051	-	Intron	coding	rarab	retinoic acid receptor alpha b
GB9	F	1	23	9041930	-	Intron	coding	eif4ba	NA
GB9	M	1	23	9041930	-	Intron	coding	eif4ba	NA
			9	19840205		outside	EST	NA	NA
GB10	F	1	9	13612198	+	Intron	coding	Fer1.6	NA
GB10	M	1	9	13612198	+	Intron	coding	Fer1.6	NA
			16	10313026	-	outside	NA	NA	NA
GB11	M	1	1	22217886	-	outside	NA	NA	Near some ESTs
GB12	F	1	-	-	+	NA	NA	NA	Zv8_scaffold2989
GB12	M	1	-	-	+	NA	NA	NA	Zv8_scaffold2989
			1	1021574	-	outside	NA	NA	Near some EST
GB13	F	1	-	-	NA	NA	NA	NA	Zv8_scaffoldNA2362
GB13	M	1	-	-	NA	NA	NA	NA	Zv8_scaffoldNA2362
GB14	F	1	12	25191547	-	outside	NA	NA	NA
	M	1	20	35239009	+	Outside	NA	NA	NA
			20	16926880	+	Outside	NA	NA	NA
GB15	M	1	-	-	+	-	NA	NA	Zv8_scaffoldNA10115, no gene in this region
GB17	F	1	9	5076130	+	Intron	coding	zgc:123286	Gene in reverse direction

			8	24547137	+	EST	NA	NA	Hits some EST
GB19	F	1	19	17038690	-	NA	NA	NA	NA
			19	32741456	+	NA	NA	NA	NA
			4	33423717	-	EST	NA	NA	Near some EST
GB19	M	1	17	6164025	-	Intron	coding	zgc:162968	taxilin beta b (txlnbb)
			9	46539915	+	Intron	coding	asb1	Gene in reverse strand
			1	14241359	+	Intron	coding	Novel	ENSDART000011475
			18	18440487	+	NA	NA	NA	NA
GB21	M	1	19	45,887,390	-	NA	NA	NA	Landed on the left side of zfpm2b
			1	51540469	-	Intron	coding	spast	Spastin (SPG4) (Intron 6-7)
GB23	F	1	23	18177925	+	NA	NA	NA	NA
GB23	M	1	23	8853854	+	NA	NA	NA	NA
			3	34743548	-	EST	EST	NA	NA
GB24	F	1	4	16262087	+	EST	NA	NA	Hit some ESTs of Extra matrix proteins
GB25	F	1	2	38,401,308	+	Intron	Predicted	si: ch211-119o8.5	Membrane, GTP binding, predicted
GB26	F	1	9	34609414	-	Intron	coding	ildr2	Immunoglobulin-like domain containing receptor 2
GB27	M	1	2	41105313	-	3'UTR	coding	BOV309_DANRE	BOV309_DANRE, gene in forwards direction
GB27	F	1	2	41105313	-	3'UTR	coding	BOV309_DANRE	BOV309_DANRE, gene in forwards direction
			15	3073904	-	Intron	coding	Zgc:85700	Zgc: 85700
GB29	F	1	5	63009435	+	Intron	coding	aspa	aspartoacylase
			12	10413689	+	Outside	NA	NA	NA
GB29	M	1	12	9769698	-	Intron	coding	erbb2	Affects Schwann cell development, DRG formation
			2	43295906	+	Intron	coding	atp1a2a	Gene in reverse direction
			3	58257509	+	Outside	NA	NA	NA
GB30	F	1	3	4541942	-	Intron	coding	Zgc:92241	Gene in forward direction
GB30	M	1	10	36592837	-	Outside	NA	NA	Nearby gene in reverse direction
			14	13841389	+	Outside	NA	NA	NA
GB31	M	1	1	29,199,477	+	Intron	coding	coro2a	Coronin, actin binding protein, 2A
GB31	F	1	9	17,190,689	-	Intron	coding	myo1bl2	Myosin 1b-like 2 (gene in reverse strand)
GB31	F	2	2	20651394	+	Intron	coding	aire	Insertion in 2nd transcripts in: B8A5S7_DANRE
			4	47955003	+	Outside	NA	NA	NA
GB32	F	1	10	14461014	+	Outside	NA	NA	NA
			16	24777878	-	Outside	NA	NA	NA
GB32	M	1	10	14461014	+	Outside	NA	NA	NA

			16	24777878	-	Outside	NA	NA	NA
GB33	F	1	20	18730983	+	Intron	coding	B8A4K9_DANRE	Gene in reverse direction
GB33	M	1	2	49036994	+	outside	NA	NA	NA
GB34	F	1	7	45762452	-	outside	NA	NA	Hit some EST
			2	30339114	+	Intron	NA	NA	Gene in reverse direction
GB34	M	1	8	42973471	-	outside	NA	NA	NA
GB35	F	1	16	35683246	+	EST	EST	EST	Some EST, outside any gene
			16	39689886	-	outside	NA	NA	NA
			16	35682792	+	outside	NA	NA	NA
			5	20216499	+	Intron	coding	novel	NP_001094419.1, ferredoxin
GB35	M	1	16	35683246	+	EST	EST	EST	Some EST, outside any gene
GB36	F	1	4	9704423	+	EST	EST	EST	Perhaps at promoter of flncb or EST intron
			2	20444596	+	Intron	coding	stk25	Gene in reverse direction
GB36	M	1	4	9704423	+	EST	EST	EST	Perhaps at promoter of flncb or EST intron
GB37	F	1	17	40754171	+	Intron	coding	LOC559917	MSH4
			6	1145961	+	outside	NA	NA	NA
GB37	M	1	17	40754171	+	Intron	coding	LOC559917	MSH4
GB38	F	1	22	17734730	-	Exon	coding	Polr2eb	Polymerase (RNA) II (DNA directed) polypeptide E,b
			21	32997806	+	Intron	coding	zgc: 175145	zgc:175145
GB38	M	1	22	17734730	-	Exon	coding	Polr2eb	Polymerase (RNA) II (DNA directed) polypeptide E,b
			15	38652808	-	Intron	coding	NA	Gene in reverse direction
			5	6379623	+	EST	EST	EST	Intron of some ESTs
GB39	F	1	6	9280536	-	Exon	coding	pglyrp2	Peptidoglycan recognition protein 2
			14	8599940	-	Intron	coding	NA	Gene in reverse direction
GB39	M	1	3	38802936	+	Intron	coding	gna12	Guanine nucleotide binding protein (G protein) alpha 12
GB40	F	1	22	20460723	-	Outside	NA	NA	NA
			24	36459061	-	Intron	coding	zgc:171660	zgc:171660
GB40	M	1	22	20460723	-	Outside	NA	NA	NA
			8	41605182	-	Outside	NA	NA	NA
			19	39448166	-	Intron	coding	asb4	Ankyrin repeat and SOCS box-containing 4
GB41	F	1	11	28030574	+	EST	EST	EST	Hit some ESTs
			8	35010930	+	Outside	NA	NA	NA
GB41	M	1	1	51055970	-	Outside	NA	NA	NA
			11	28030574	+	EST	EST	EST	Hit some ESTs

GB43	F	1	15	33210214	+	Exon	coding	lsrl	Lsr like
			10	43436181	-	Intron	coding	NA	Insertion in reverse direction of the gene
GB43	M	1	23	17836536	+	NA	NA	NA	NA
			4	16597455	-	NA	NA	NA	NA
			2	53671163	+	Intron	coding	zgc:153304	Zgc:153304
GB44	F	1	7	15154427	+	Intron	coding	Pax6b	Pax6b
GB44	M	1	6	3787921	+	Intron	coding	NA	Reverse direction of a LOC gene
GB44	M	1	13	24565240	-	NA	NA	NA	NA
GB46	F	1	21	16261744	+	NA	NA	NA	NA
GB46	M	1	21	17767753	+	Intron	coding	atp2a2b	ATPase, Ca++ transporting, cardiac muscle, slow twitch 2b
GB47	M	1	14	22272178	+	Intron	coding	zgc: 66433	zgc: 66433
			9	50892485	-	NA	NA	NA	NA
			14	22047954	-	NA	NA	NA	NA
GB47	F	1	9	50892485	-	NA	NA	NA	NA
			14	22047954	-	NA	NA	NA	NA
GB48	F	1	15	886441	+	Exon	coding	LOC555761	FAM115A/C
			1	47517724	-	NA	NA	NA	NA
			24	39737733	+	Intron	coding	Zgc:64119	Xylulokinase homolog
			X	NA	NA	NA	NA	NA	NA
	M	1	15	886441	+	Exon	coding	LOC555761	FAM115A/C
			13	18337395	+	Intron	coding	NP_001139072.1	KCNMA1, potassium large conductance calcium-activated channel, subfamily M, alpha member 1 fragment
			X	NA	NA	NA	NA	NA	NA
GB49	M	1	24	3020952	-	NA	NA	NA	Some nearby EST
			9	36390659	-	NA	NA	NA	In inter-gene space, nearby 2 genes
GB50	F	1	9	17642683	+	NA	NA	NA	NA
			X	NA	NA	NA	NA	NA	NA
		2	1	16200674	-	NA	NA	NA	NA
			6	40248994	+	Intron	coding	Slc9a7	Gene in reverse strand
GB51	F	1	1	1758953	+	NA	NA	NA	NA
		2	1	1758953	+	NA	NA	NA	NA
GB52	M	1	1	47517631	-	NA	NA	NA	NA
GB53	M	1	3	37268101	+	NA	NA	NA	NA
GB54	F	1	13	19683770	-	Intron	coding	B8A682_DANRE	ANUBL1, AN1, ubiquitin-like, homology

			X	NA	NA	NA	NA	NA	NA
GB56	F	1	3	850800	+	NA	NA	NA	NA
GB57	F	1	4	37063218	-	NA	NA	NA	NA
	M	1	3	14114092	+	Intron	coding	WNK1	WNK1(2 of 4) pseudohypoaldosteronism type II
GB58	F	1	12	20551910	+	NA	NA	NA	NA
			24	15238498	+	NA	NA	NA	NA
			23	11358497	-	NA	NA	NA	NA
GB59	F	1	14	9933075	+	Intron	coding	tmem129	transmembrane protein 129
			1	30194560	-	Intron	coding	si:dkey-7m11.2	KCNQ5
	M	1	X	NA	NA	NA	NA	NA	NA
GB60	F	1	1	507955	-	Intron	coding	Mrpl39	Gene in the other direction
	M	1	4	NA	NA	NA	NA	NA	Not able to map to specific site
			18	44330864	+	NA	NA	NA	NA
			8	18329755	+	Intron	coding	st6galnac5	Gene in the other direction
			23	41919480	+	NA	NA	NA	NA
GB61	F	1	14	36780466	-	NA	NA	NA	Next to the start of clint1, epidermal gene
			24	1250017	-	Intron	coding	Nrp1a	Gene in the other direction
			1	1010110	+	Intron	coding	zgc:92834	N-6-adenine-specific DNA methyltransferase 1, N6AMT1
			8	10229695	-	NA	coding	zgc:113105	Protein tyrosine phosphatase, non-receptor type 18
			10	628124	+	Intron	coding	rfx3	Gene in the other direction